THE DEFORMATION RESPONSE OF POLYCRYSTALLINE MAX PHASES UNDER HIGH STRAIN-RATE LOADING

by

Riddhiman Bhattacharya

A dissertation submitted in partial fulfillment
of the requirements for the degree of
Doctor of Philosophy
(Materials Science and Engineering)
in The University of Michigan
2016

Doctoral Committee:

Associate Professor Nakhiah C. Goulbourne, Co-chair
Professor John W. Halloran, Co-chair
Professor John E. Allison
Associate Professor Miladin Radovic, Texas A & M University
Associate Professor Veera Sundararaghavan
Professor Anthony M. Waas , University of Washington, Seattle

To my parents

Acknowledgements

First and foremost, I would like to thank my adviser, Prof. Nakhiah Goulbourne for mentoring and advising me during my graduate studies. I am grateful for the amount of time she has invested in carefully analyzing my work and iterating several times until it meets her expectations, and the bar has always been set very high. Therefore, it has been challenging journey but I feel enriched to have gone through the rigor. Second, I would like to thank Prof. John Halloran for graciously agreeing to serve as a co-chair on my committee and my other committee members, Prof. John Allison, Prof. Anthony Waas, Prof. Veera Sundararaghavan, and Prof. Miladin Radovic for agreeing to serve on my committee. In this regard, I am extremely grateful to Prof. Waas (and members of his research group with whom I have worked) for allowing me to use the Hopkinson bar set-up, and MTS machine in his lab. A major portion of this dissertation constitutes of experiments conducted using his equipment and therefore I am thankful for his support. I would like to thank Prof. Miladin Radovic and his research group for providing the Ti_2AlC and Ti_3SiC_2 samples. Furthermore, his long association and high level expertise with MAX phases have stimulated several interesting discussions during our collaboration that has improved the quality of this dissertation. I am thankful for the interactions I had with Prof. Amit Misra about my career plans and his mentorship in this regard has been inspirational.

I would also like to thank the staff members and technicians in MSE and AE, specifically, Renee Hilgendorf, Denise Phelps, Thomas Griffin, Aaron Borgman, Chris, Terry Larow, and Keith McIntyre for their assistance regarding administrative or technical aspects.

I am equally grateful to people outside work and university, who have helped me maintain my calmness while working through the hardships of graduate school. In this regard, I would like to thank all my friends in Ann Arbor, most of who happen to be the Aerospace Engineering department. There are too many people to name individually. I would like to thank members of the softball intramural team (Aeros in the outfield) that I was part of and members of Prof.Goulbourne's research group, especially, Yali Li and Dr. Jacob Davidson who have been more than just colleagues. I would also like to thank Arunabha Mohan Roy and Rahul Datta – who is also my cohort and therefore we go back a long way. I am grateful to have them around whenever I needed them the most during the hard times as well as during fun times.

Finally, I would like to thank to my parents, Prof. Sriman K Bhattacharyya, and Mrs. Kajal Bhattacharya for all the love, affection, and support that they have provided – not only in the past few years as a graduate student but also for bringing me up to be the person I am today. Words cannot describe my gratitude for you and therefore I aspire to live up to your expectations through my accomplishments in life.

Table of Contents

CHAPTERS

List of Tables

List of Figures

List of Appendices

List of Acronyms

ASTM	American Society for Testing of Materials
BC	Boundary Condition
BPTT	Brittle Plastic Transition Temperature
DIC	Digital Image Correlation
EBSD	Electron Back Scattered Diffraction Pattern
EDM	Electrical Discharge Machining
EDS	Energy Dispersive Spectroscopy
FE	Finite Element
FGHC	Functionally Graded Hybrid Composite
GCMeC	Graded Ceramic Metal Composite
HCP	Hexagonal Close Packed
HP	Hot Pressing
HIP	Hot Isostatic Pressing
IKB	Incipient Kink Band
KB	Kink Band
KNE	Kinking Non-linear Elastic
LAGB	Low Angle Grain Boundary
MAX	Generic term for $M_{n+1}AX_n$ Phases
SEM	Scanning Electron Microscope / Microscopy

SHPB	Split Hopkinson Pressure Bar
SPS	Spark Plasma Sintering / Sintered
TEM	Transmission Electron Microscope/Microscopy

List of Symbols

$c{:}a$	Aspect ratio of hexagonal crystals
Ti_2AlC	Titanium Aluminium Carbide
Ti_3SiC_2	Titanium Silicon Carbide
$\dot{\varepsilon}$	Strain rate
ε_i	Incident strain pulse
ε_r	Reflected strain pulse
ε_T	Transmitted strain pulse
σ	Stress
σ_y	Yield Stress
C_o	Longitudinal wave speed in bar material
E_b	Elastic modulus of bar material
A_b	Cross sectional area of bars
A_S	Cross sectional area of specimen
L or L_s	Length of specimen
C	Longitudinal wave speed in material
D_s	Diameter of specimen
D_b	Diameter of bars
R	Stress Ratio
σ_f	Front end stress (specimen-incident bar interface)

$\boldsymbol{\sigma_b}$	Back end stress (specimen-transmission bar interface)
$\boldsymbol{u}$	Displacement in x direction
$\boldsymbol{v}$	Displacement in y direction
$\boldsymbol{D_i}$	Inhomogeneity parameter

Abstract

THE DEFORMATION RESPONSE OF POLYCRYSTALLINE MAX PHASES UNDER HIGH STRAIN-RATE LOADING

By

Riddhiman Bhattacharya

$M_{n+1}AX_n$ phase ternary compounds (or MAX phases) are a relatively newer class of nano-layered, ternary compounds (carbides or nitrides) which exhibit unique combination of properties typical of ceramics and metals. Hence, they are attractive candidates for use in structural applications. However, the responses of MAX phases under dynamic loading conditions have not been characterized extensively. In this dissertation, experimental protocols to characterize representative MAX phases (Ti_2AlC and Ti_3SiC_2) under high strain-rates are developed using a Split Hopkinson Pressure Bar (SHPB) set-up. It is observed that Ti_2AlC shows significant inelastic deformation and relatively higher strains before fracture, even at very high strain-rates (~up to 4700 s^{-1}), underlying cause of which is attributed to kink banding of the nano-layered structure at sub-grain length scale. On the other hand, Ti_3SiC_2 exhibits a response more typical of ceramics and therefore additional modification to the experimental set-up and protocols are necessary. Local strain field analysis using Digital Image Correlation (DIC) shows that strain evolution is heterogeneous, underlying origins of which can be related to existence of grain clusters. The clusters span several grains that are identified as discrete homogeneous patterns on the strain distribution maps. The geometric properties of a grain and neighboring grain effects by virtue of its position in polycrystalline MAX phase are of relevance in dictating the deformation modes. A computational model is developed to capture the effect of grain geometry and multi-axial stress state experienced by a grain in a polycrystalline material due to its neighbors and applied external loading.

Chapter 1: Introduction and Motivation

1.1 MAX phase fundamentals and applications

MAX phase materials or MAX phases are a class of ternary solids, known for exhibiting a unique combination of properties of both ceramics and metals. More generally, these materials have a formula of $M_{n+1}AX_n$ where M is an early transition metal (Ti, V, Cr, Zr, Nb, Mo, Hf , and Ta), A is a group 13 or 14 element (Al, Si, P, As, Ga, Ge, As, Cd, In, Tl, and Pb), and X is Carbon (C) or Nitrogen (N)[1-4] . Currently there are more than 60 known MAX phases, which were first discovered in the 1960s by Nowotny and co-workers [5, 6]. Bulk processing and characterization of MAX phases were first reported by Barsoum et al.[4, 7] in the late 1990s, which led to a renewed interest in these materials. MAX phases are elastically stiff, thermally and electrically conductive similar to conventional ceramics (or their binary counterparts), while exhibiting high machinability, thermal shock resistance, damping capabilities, and unusual damage tolerance. The combination of properties makes them highly suitable as high temperature structural materials. In this dissertation two representative MAX phases are characterized under dynamic loading, often encountered in aerospace and defense related applications.

These materials crystallize in a Hexagonal Close Packed (HCP) crystal structure, because of which polycrystalline MAX phases lack the five independent slip systems, necessary for maintaining integrity during deformation. That is to say, conventional slip is limited to basal planes. In typical HCP metals such as Magnesium (Mg), Titanium (Ti), deformation progresses via twin formations[8, 9]. However, given the high c/a ratio of MAX phase unit cells, twinning is not favored. The value of n in the general $M_{n+1}AX_n$ varies from 1-3, which results in three different classes of MAX phases viz. 211, 312, and 413 type. Figures 1.1(a)-(c) show the three different classes of MAX phases and their respective crystallographic structures. For each of the material classes, near close packed M layers are interleaved with A layers. The X atoms occupy the octahedral void sites between the M layers. The M_6X octahedral sites are in an “edge-sharing” configuration, reminiscent of the classic rock salt structure. The key difference between the different classes is in the number of M layers which separate the A layers. That is to say, in 211 MAX phases there are two; three for 312 type; four in the case of 413. Bonding in MAX phases is dominantly metallic (M-M), with covalent and ionic contributions arising from the M-A and M-X bonds respectively. The MX ionic bonds are exceptionally strong with M-A covalent bonds being relatively weak, especially in shear [10].

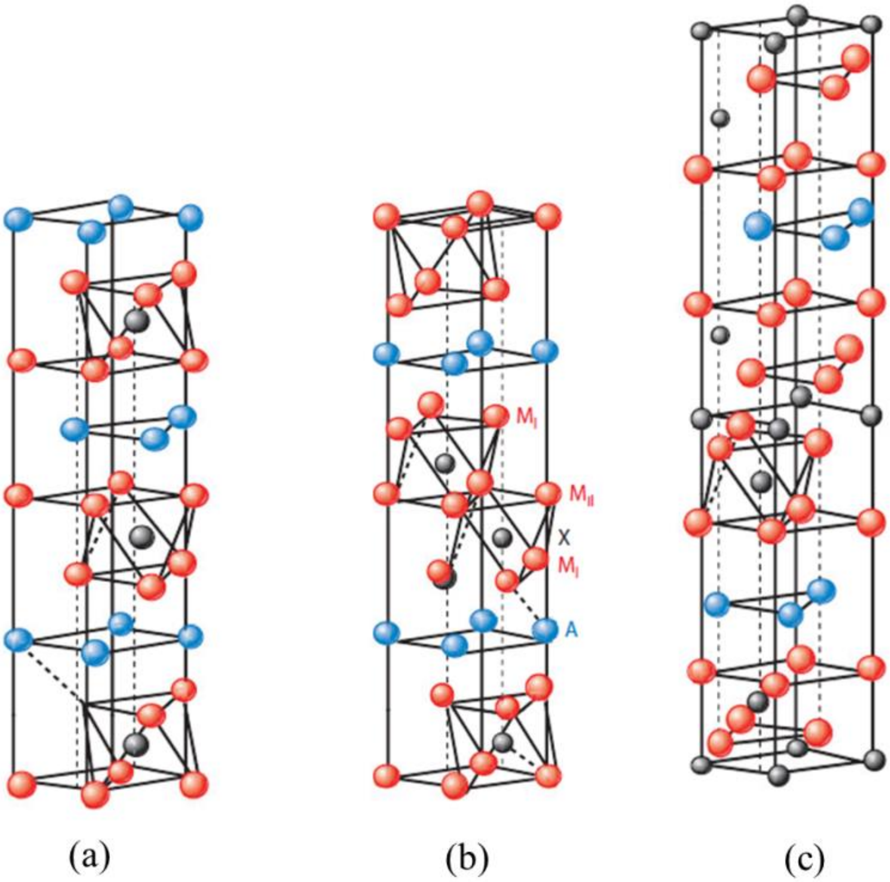

(a) (b) (c)

Figure 1.1 Representative crystal structures of MAX phases showing the a) 211, b) 312, and c) 413 types (taken from Ref [2] in compliance with "fair use" policies)

Theoretically, the lack of non-basal slip and twinning should lead to a brittle linear-elastic response in a polycrystalline MAX phase, often encountered in conventional ceramics such as SiC[11]. However, the unique combination of bonding leads to interesting mechanical properties at the macroscale, as introduced earlier. At the nanoscopic scale, a layered structure is observed, which deforms via a combination of kink and shear band formations, along with delaminations[10, 12]. Kink bands and delaminations are ubiquitous in fiber composites, where they are classified as failure modes[13, 14]. However, these features are energy absorbing mechanisms, which are more favorable over conventionally brittle modes of deformation such as microcracking, cleavage type fracture, and therefore are believed to contribute towards the damage tolerant behavior. Furthermore, these features are formed in MAX phases due to highly mobile dislocations over a range of temperatures (up to 1200^{o}C), which multiply and arrange into arrays or walls[2, 3]. These arrangements lead to kink boundaries, which are discussed in a greater detail in the following sub-section. The mechanisms are often classified as pseudo-ductile to distinguish them from conventional ductility caused by slip. The most common and well characterized MAX phases include Ti_2AlC[15, 16], Ti_3SiC_2[4, 7, 17, 18], and Ti_3AlC_2[19-21]. These materials have been characterized extensively under compressive[15-18], tensile[22], flexural[17] loading conditions along with their temperature dependencies[17-22], and crack healing characteristics[23]. Representative MAX phases, Ti_2AlC and Ti_3SiC_2, possess exceptional oxidation resistance up to temperatures of ~1400^{o}C[24, 25]. Ti_2AlC forms a protective layer of Al_2O_3, which remains stable and don't spall after 10,000 thermal cycles at 1400^{o}C[26]. These characteristics, along with the other favorable attributes mentioned earlier (such as high damage tolerance due to kink band formation), justify their inclusion in a Functionally Graded Hybrid Composite (FGHC), designed for extreme thermo-mechanical environments such as a hypersonic jet. A conceptualized version of a FGHC is shown in Figure 1.2. The different layers in the hybrid composite offer different functionalities such as thermal barrier to high temperatures (top oxide layer), and load bearing capabilities that facilitate in situ sensor integration (bottom PMC layer). MAX phases belong to the central Graded Ceramic/Metal Composite (GCMec) layer, which provides damping and damage tolerance to the structural component. Although MAX phases have been extensively characterized under quasi-static loading conditions (10^{-6}-10^{-3} s^{-1}) in the last two decades, there remains a gap in understanding of their dynamic response i.e. response under extreme loading conditions, often encountered in structural components such as hypersonic jet skins[27].

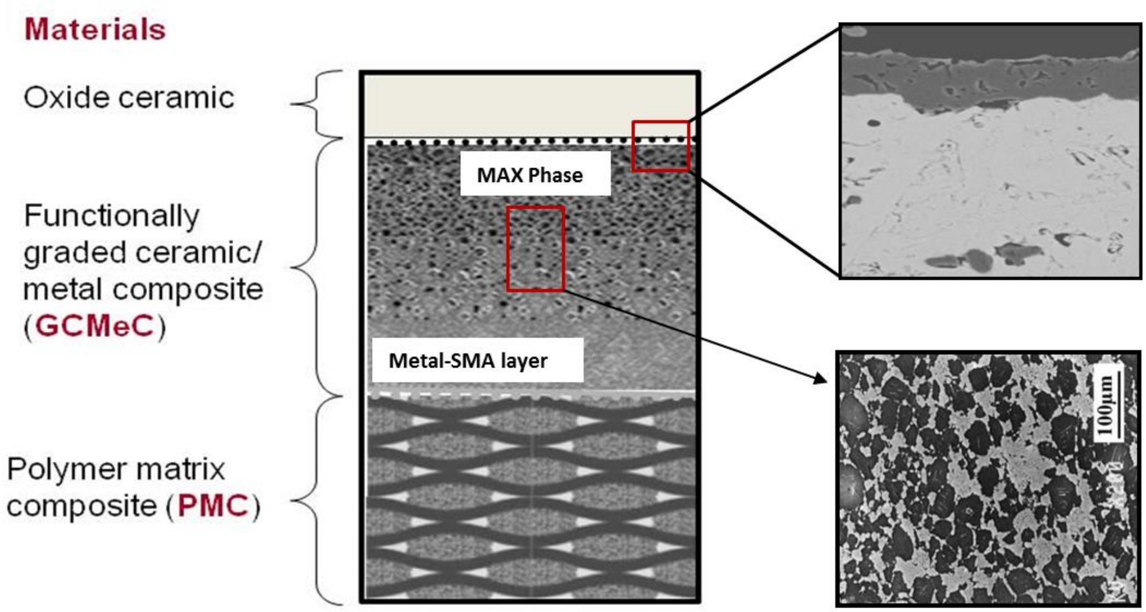

Figure 1.2 A conceptualized schematic of the Functionally Graded Hybrid Composite (FGHC) suited to withstand high thermomechanical loading conditions.

This dissertation focuses on characterizing these representative polycrystalline MAX phases under high strain-rates (10^2-10^4 s^{-1}). The experimental protocols and necessary modifications for testing the representative MAX phases are presented, along with their macroscale response and microscopic origins. Furthermore, in situ experimental methods and analyses suggest the presence of grain clusters forming a meso-structure, which is purported to play an important role in the deformation response of MAX phase polycrystals. Finally, a computational approach is presented, which captures the pseudo-ductile modes of deformation in an inherently multi-layered grain in a polycrystalline neighborhood.

1.2 Processing methods and microstructure

The 211 and 312 type MAX phases were first to be discovered with several researchers attempting to process bulk materials until mid-1990s[10]. The first successful attempt at fabricating fully dense Ti_3SiC_2 samples in one single step using reactive Hot Pressing (HP), was reported by Barsoum et al. in 1996[4]. It was observed that the bulk compound was better electrical and thermal conductor than Ti or TiC, had a modulus of 320 GPa, yet relatively soft and machinable. Following this initial discovery, other MAX phases – Ti_2AlC, Ti_2AlN, Ti_2GeC and Ti_3GeC_2 – were also shown to possess properties similar to Ti_3SiC_2 and thus several members of the MAX phase family were obtained.

El Raghy and Barsoum[7] observed that pure Ti_3SiC_2 is stable up to 1700^oC and thermal decomposition of powders at lower temperatures is a signature of impurities existing in the commercial powders, used as initial starting materials for bulk processing. TiC is the most common impurity, followed by TiSi and $TiSi_2$. Similarly, Ti_2AlC in its purest state is stable up to 1600^oC but pre-existing impurities can lead to the following reaction occurring at temperatures of ~1500^oC[10]:

$$2Ti_2AlC = Ti_3AlC_2 + TiAl_x + (1-x)\ Al, \text{ where } x < 1 \ldots\ldots\ldots(1.1)$$

Therefore, $TiAl_x$ is a common impurity observed in Ti_2AlC resulting from contaminations in starting materials. In an open system, the Al formed in reaction 1 segregate at the grain boundaries. In a closed system, a situation commonly encountered during processing of MAX phases, the Ti powder reacts with the graphite dies to form TiC, thereby preventing formation of Al (and their segregation at the grain boundaries). As a result, $TiAl_x$ and TiC are the most commonly found impurities in MAX phases.

The microstructures resulting from these processing techniques result in elongated plate-like grains[28] with random orientations (i.e. no texture) and grain size distributions (see section 2.1 for details). In the last two decades, researchers in the community have shown development of several different methods to process bulk MAX phases, with the objectives of i) obtaining an equiaxed overall microstructure, with narrower grain size distributions, ii) achieving near perfect densification, iii) reducing the impurity content in the material, and iv) fabricating textured samples [10]. Following the initial processing using HP [4], Barsoum et al. reported on using Hot Isostatic Pressing (HIP) [7,12,17,24]. Murugaiah et al. [28] reported on using tape casting followed by cold pressing and pressureless sintering, and studied the effects of sintering in the presence of C and Si, which inhibit grain growth. Li et al.[29] showed evidence of obtaining high density (>98 %) and 80% pure Ti_3SiC_2 using pressureless sintering, starting with mechanical alloying of elemental Ti, Si, and graphite (C) powders. The processing of bulk Ti_3SiC_2 using Spark Plasma Sintering (SPS) was also first reported by Gao et al.[30] around the same time, in which the desired heating could be obtained in a few minutes, thereby making the process extremely efficient. A common characteristic of the microstructure resulting from the different processing routes is the plate-like elongated grains, which occurs due to different growth rates along *c* and *a* directions (see Fig.1.1) although the grain size distributions vary based on the processing conditions. It must also be noted that Barsoum and El-Raghy[12] had also obtained oriented macrograined Ti_3SiC_2 using a sinter forging technique, which involved hot pressing of pre-reacted MAX phase powders. Recent approaches in the literature have used techniques like magnetic fields[31], subsequent SPS of finely powdered MAX phases[32], and spark plasma deformation[33] to form textured compounds. Based on post processing characterizations presented in some of these reports, it is anticipated that textured MAX phases would show superior mechanical properties if ductile and pseudo-ductile mechanisms of deformation (see section 1.3) are dominant. Therefore, current research efforts in the MAX phase processing community are focused at fabricating textured samples. In this dissertation, however, properties of polycrystalline MAX phases are demonstrated.

Figures 1.3(a) and (b) show a microstructure from a sample used in this work, processed using pressureless sintering of commercial powders at 1500°C in inert atmosphere. The low magnification image (Fig. 1.3(a)) shows existence of larger grains (~100 μm) in a matrix of smaller equiaxed grains (10-20 μm). The higher magnification image (Fig. 1.3 (b)) highlights the inherent nano-layered structure of the grain. Furthermore, the elongated plate-like nature of the grains is also evident. The average grain lengths and widths were 16 μm of 4 μm respectively, based on measurements performed at Texas A&M University [27].

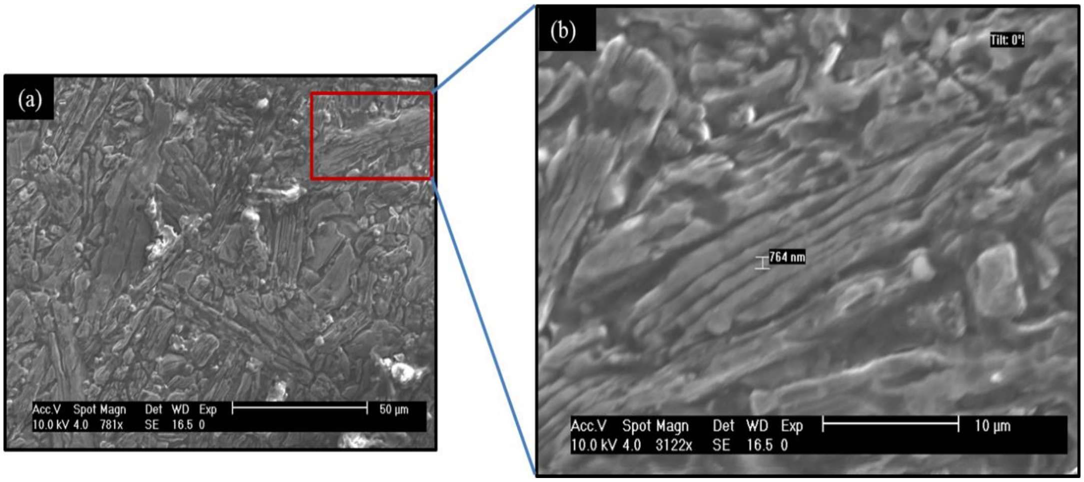

Figure 1.3 Etched microstructures of polycrystalline Ti_2AlC processed using pressureless sintering[1], showing a) the random grain structure, and b) a magnified grain showing the nano-layers of ~700 nm in thickness.

1.3 Mechanical Properties of Ti_2AlC and Ti_3SiC_2

1.3.1 Quasi-static response

MAX phases, although similar to their MX counterparts in some aspects (high modulus and hardness), respond very differently when subjected to different kinds of loading such as compression, tension, flexure, and shear[10]. Furthermore, these materials demonstrate excellent machinability. The difference is attributable to the unique layered microstructure and presence of mobile dislocations, briefly introduced in previous sub-sections. Although the response of different MAX phases (Cr_2AlC, V_2AlC, Ti_3GeC_2, Nb_4AlC_3, Ta_4AlC_3) have been reported in the literature, we restrict our discussion to Ti_2AlC and Ti_3SiC_2 in this dissertation.

---

[1] Processed at Texas A&M University (Prof. Miladin Radovic's research group)

It has been reported that Ti_3SiC_2 shows catastrophic failure[34] while the other 211 (such as Ti_2AlC, Ti_2AlN) type show a “graceful” failure [10], with a sharp drop after attainment of peak stress.

Table 1.1 summarizes the peak stress values as a function of grain sizes for Ti_2AlC under compressive loading at room temperatures, which show that peak stress values increase with decreasing grain sizes[34-36]. The dependence of peak stress on strain-rates does not show a trend under quasi-static loading conditions. A similar behavior is observed under higher strain-rates, as discussed in detail later in this dissertation (see Chapter 3). The maximum engineering strains have been reported to be ~4 % at peak stress values under quasi-static loading reported in the literature. Figure 1.4 shows the inverted “V” type stress-strain response commonly observed in Ti_2AlC. It is understood from our in situ imaging analysis that the strain softening behavior is due to crack formations, as pointed out later in this dissertation. Therefore, the strains at the point corresponding to peak stress are treated as the maximum compressive strain.

Table 1.1: Mechanical properties of Ti_2AlC under quasi-static compressive loading at room temperature

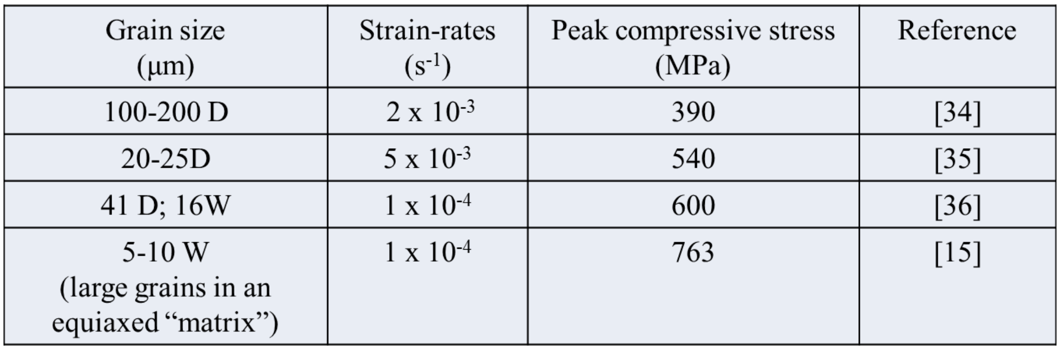

Grain size (μm)	Strain-rates (s^{-1})	Peak compressive stress (MPa)	Reference
100-200 D	2×10^{-3}	390	[34]
20-25D	5×10^{-3}	540	[35]
41 D; 16W	1×10^{-4}	600	[36]
5-10 W (large grains in an equiaxed “matrix”)	1×10^{-4}	763	[15]

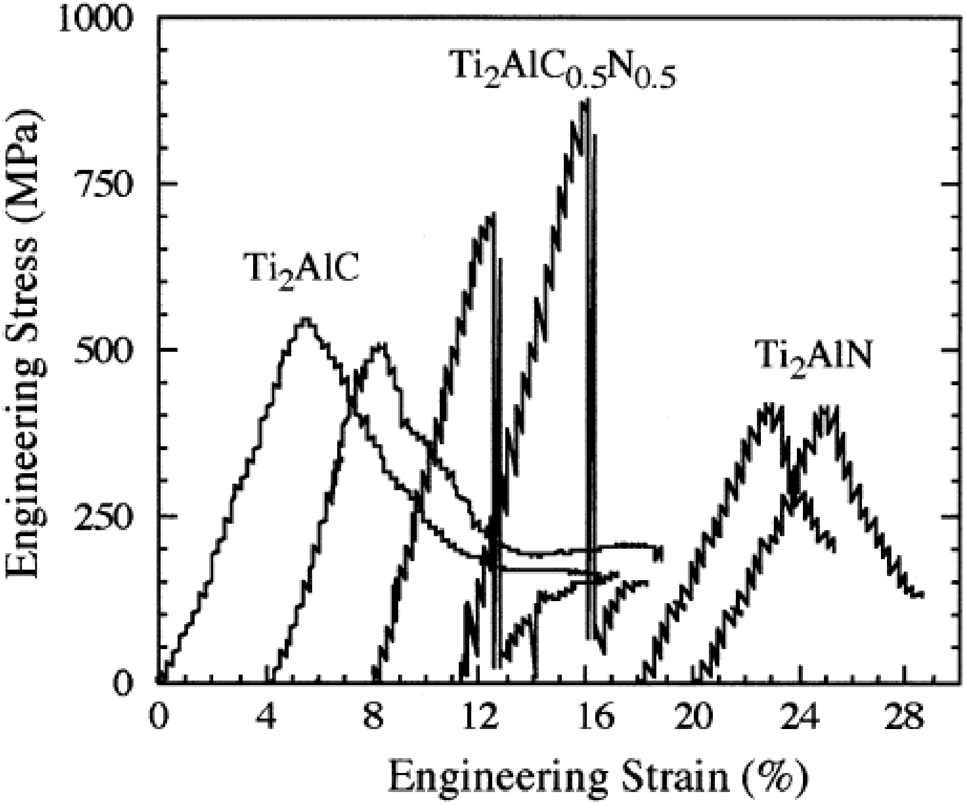

Figure 1.4 Stress-strain curves for different MAX phases for compression under room temperatures (taken from [34] in compliance with "fair use" policies).

Table 1.2 shows the relevant mechanical properties as a function of grain sizes for Ti_3SiC_2 under both compressive and tensile loading conditions[37]. A trend similar to Ti_2AlC is observed with respect to grain size, where the peak compressive stress increases with grain refinement. Whether these materials obey Hall-Petch relationship (Eqn. 1.2) or not has not been extensively reported. One report by Hu et al.[38] on V_2AlC has shown that the peak compressive stress varies linearly with $d^{-1/2}$, thereby showing a near Hall-Petch type variation with yield stress, $\sigma_y = 0$. This can be a plausible assumption for MAX phases since they don't yield in the classical sense.

$$\sigma = \sigma_y + k\, d^{-1/2} \ldots\ldots\ldots\ldots\ldots\ldots\ldots..(1.2)$$

In the context of this dissertation, response under flexural and shear loading is not relevant.

Table 1.2: Mechanical properties of Ti_3SiC_2 under quasi-static loading at room temperature

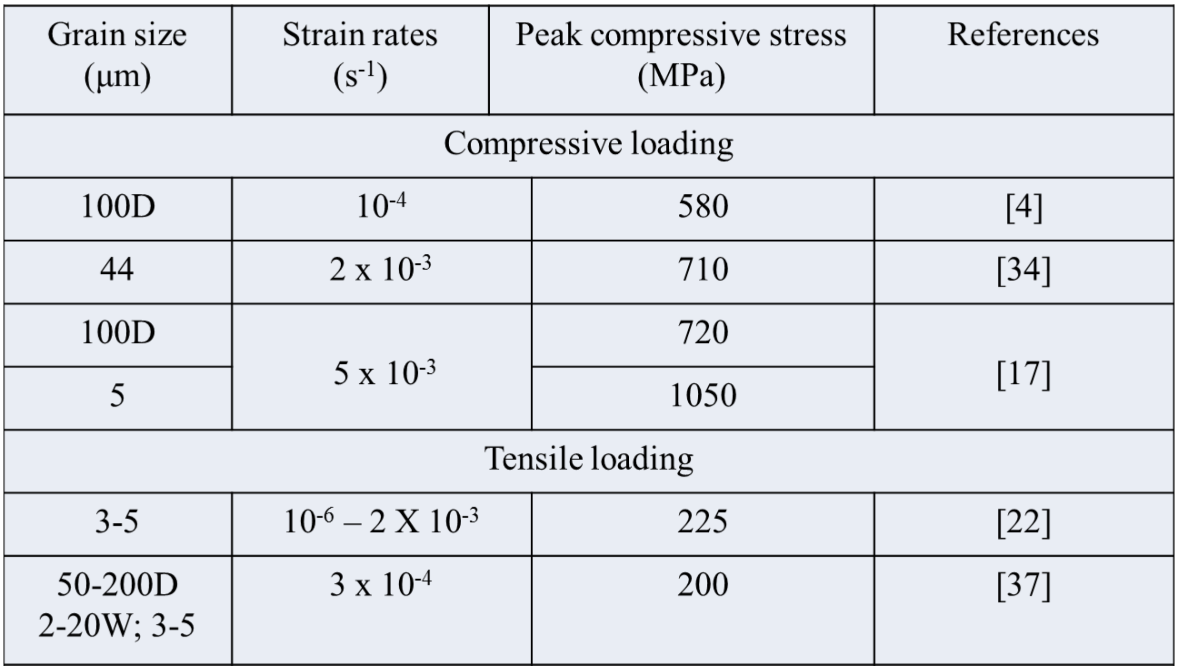

Grain size (µm)	Strain rates (s^{-1})	Peak compressive stress (MPa)	References
Compressive loading			
100D	10^{-4}	580	[4]
44	2×10^{-3}	710	[34]
100D	5×10^{-3}	720	[17]
5		1050	
Tensile loading			
3-5	$10^{-6} – 2 \times 10^{-3}$	225	[22]
50-200D 2-20W; 3-5	3×10^{-4}	200	[37]

The most intriguing aspect of the mechanical response of both Ti_2AlC and Ti_3SiC_2 is the stress-strain hysteresis under cyclic loading, dissipating upto 25% of mechanical energy, thereby making them highly suitable for damping and vibration mitigation applications [2]. The hysteresis loops are fully reversible under room temperatures which show some rate-dependence and inelastic effects under higher temperatures [2,15,18]. The microstructural origin of reversible cyclic behavior had initially been attributed to a reversible feature called Incipient Kink Bands (IKBs), which can be realized as a pre-cursor to fully formed Kink Bands (KBs). However, it must be noted that there are no direct experimental evidence supporting the IKB theory. Recently, cyclic loading experiments performed using in situ diffraction methods[39] pointed towards mesostructructal interactions in polycrystalline Ti_3SiC_2 as a cause for hysteresis. In other words, grains which are favorable for slip interact with the grains which are not favorable for slip (soft grains) and lead to build up of elastic strains in hard grains, which are reversible. A more recent report by Benitez et al. [40] has shown formation of Low Angle Grain Boundaries (LAGBs) in polycrystalline Ti_2AlC irrespective of orientations, thereby pointing towards neighboring grain effects in the kinking and deformation process.

The high temperature mechanical properties of MAX phases make them highly attractive for applications involving thermo-mechanical loading conditions. A brittle-to-plastic transition temperature (BPTT) has been observed to lie in the range 1000-1100^oC in Ti_3SiC_2 and some Al-containing MAX phases[41-43]. BPTT is defined as a particular temperature range beyond which ductile or plastic behavior is observed in an otherwise brittle material. In typical metals (and solids) in general, the fracture toughness increases above a certain transition temperature, commonly labeled as ductile-to-brittle transition (DBT) temperature[44]. This phenomenon is related to activation of additional slip systems, which are inactive below the transition temperature. However, for MAX phases, the fracture toughness drops thereby indicating mechanisms different from slip system activation [10] i.e. pseudo-ductile mechanisms, which are discussed in much greater detail in the next sub-section. It must be noted that the pseudo-ductile mechanisms lead to generation of high internal stresses [2,10]. It has been reported that high temperature compressive loading leads to strains on the order of 15% [41] and a *yield* point is observed followed by a work hardening regime. The grain size dependency of the peak compressive stress is still observable beyond the BPTT. Similar results have also been reported for Ti_2AlC[34], and other MAX phases[18,41]. On the other hand, response of Ti_3SiC_2 under tensile loading condition[22,37] have been reported to show higher strains to failure and peak compressive stresses in the fine grained microstructure. This is contrary to the Hall-Petch behavior enumerated earlier. Higher internal stresses in the coarse grained microstructure and greater dissipation capabilities of internal stresses in the fine grained microstructure have been theorized to be possible causes for this difference. Furthermore, evidence for cyclic hardening has been observed at temperatures of ~1200^{o}C in coarse and fine grained microstructures. This feature is more dominant in coarse grained Ti_3SiC_2 and is manifested in the form of smaller areas enclosed by the hysteresis loops[45]. It has also been reported that the elastic limit is reached with increased cycling, implying that increased cycling leads to micro-domain formations which are difficult to kink than initial grains. It has also been proposed that the observed hardening is a macroscale manifestation of crack healing characteristics at lower length scales [10].

A rather interesting and beneficial characteristic of MAX phase deformation under high temperatures deformation is their resistance to thermal shocks. It had been reported that some representative MAX phases retain their flexural strengths post-quench[46, 47]. A secondary contribution resulting from the work presented in this dissertation has shown that dynamic compressive strengths of Ti_2AlC are retained post-quench, and the pseudo-ductile mechanisms of kink banding are ubiquitous on post fracture micrographs. The mechanisms underlying the unique thermal shock response of MAX phases is still an open question in the community.

1.3.2 Dynamic response

The reports summarized in the previous sub-section provide an account of experimental analyses conducted under quasi-static ($10^{-6} – 10^{-3}$ s^{-1}) loading conditions. The dynamic or high strain-rate response of MAX phases have not been studied or reported extensively, which motivates this dissertation. To date, there are only two reports on impact response of MAX phases. Lo et al[48] investigated the ballistic impact response (at a velocity of 380 m/s) of hot pressed Ti_3SiC_2 and analyzed the multiscale mechanisms associated with the deformation. The microscale analyses presented in this work showed evidence of intergranular, transgranular fracture, delamination, and grain pull-outs. TEM analysis showed evidence of stacking faults that extended from grain boundaries. A recent report on high strain-rate response of fine grained Ti_2AlC investigated the combined role of high temperatures using a SHPB technique[49]. The material used in this work had a finer grain size that resulted in room temperature peak stress values of up to 1800 MPa at a strain-rate of 500 s^{-1}.

In this dissertation, the technique of SHPB is used to characterize Ti_2AlC and Ti_3SiC_2 over a range of strain-rates in the regime 10^2-10^3 s^{-1}. The technique consists of applying a stress-wave to a specimen, as elucidated later in the dissertation (Chapter 2). There are no standardized protocols for experimentally analyzing different classes of materials using a SHPB technique. Therefore, material specific design protocols are necessary. The lack of experimental studies on high strain-rate response necessitates development of specific protocols for Ti_2AlC and Ti_3SiC_2 that are presented in chapters 3 and 4.

1.3.3 Microstructural features of deformation

The unique combination of mechanical properties over a range of temperatures led researchers in the area to probe further into the deformation mechanisms operative in MAX phases. During the last two decades, several theories have emerged at multiple length scales. Generally speaking, a polycrystalline bulk MAX phase is not expected to deform via extensive slip due to the lack of five independent slip systems, as mentioned earlier. There is little or no evidence of twin formations either [10]. However, it was observed that under the application of load, the layered microstructure gives rise to Kink Bands (KBs), reminiscent of folded structures often encountered in geological structures[50, 51].

However, the origins of KBs can be traced back to highly mobile dislocations that arrange themselves in certain arrangements (pile-ups and walls), thereby forming the boundaries of KBs. Several TEM studies have confirmed that these dislocations are mostly basal in nature with a mixed nature i.e. it has both edge and screw components. Dislocation based KBs had been observed earlier in 1950s in Cd[52] and Zn[53] crystals, wherein several qualitative theories were proposed. Around the same time, Frank and Stroh[54] used a Griffith like approach to model growth of sub-critical KBs using the concept of remote shear stress. This approach was extended to model the growth of IKBs (which are pre-cursors to KBs) in MAX phases and other KNE solids by Barsoum et al.[55, 56]. Reports by Guitton et al.[57] and Lane et al. [58] have shown evidence of dislocation-dislocation interactions, which are also believed to contribute significantly towards the KB formation mechanism. However, a more recent report by Guitton et al. [59] have pointed towards multi-axial state of stress and grain bending mechanisms in a polycrystalline grain as a cause for hysteresis and elastoplastic heterogeneous strains.

Post-fracture micrographs reported in the literature[60] have shown crack bridging properties, which led to the inference that KB formations lead to higher damage tolerance in MAX phases. It must be noted that KBs in MAX phases are often, if not always, accompanied by delaminations, where a stack of nano-laminates or individual layers delaminate with respect to adjoining layers. Figure 1.5(a) shows a typical buckled grain (circled region) surrounded by regions of extensive damage. In Price and Cosgrove[51], folds are classified as: i) chevron folds, ii) kink folds or kink bands, iii) box folds, iv) similar or concentric folds, and v) parallel folds. Conditions where the limbs are connected by rounded hinges are known as concentric folds, as shown in Fig. 1.5(b). Figure 1.5(c) shows sharp and pointed hinges that are signatures of kink bands and chevron folds, which are the most widespread in MAX phases. A third type of folding called box folding is also observed wherein the hinge regions are plateau like or near-parallel to the initial pristine flat state, as shown in Fig. 1.5(d). The arrows in each figure point towards the hinge regions, thereby highlighting the type of folding. In fiber composites, two types of kinking have been reported i.e. in plane kinking and out of plane kinking[14]. Figures 1.6(a) and (b) show a schematic of the two types of kink bands. Majority of the post-fracture SEM images of MAX phases show evidence of in plane kinking (that are similar to chevron type folding) and delaminations. Out of plane type kink bands have been observed and reported for other crystallographic structures, such as Zn[61] and are also known as “stove pipe kinks”[62].

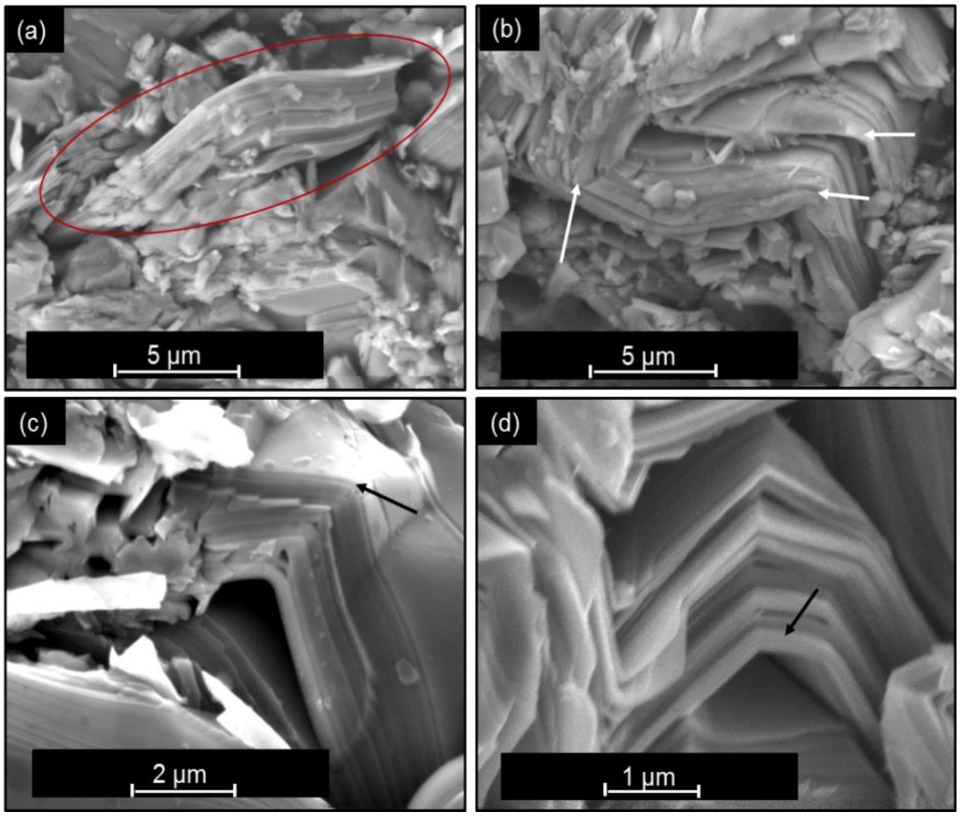

Figure 1.5 Post-fracture SEM micrographs of Ti_2AlC showing a) grain buckling, b) concentric folding, c) chevron folding, and d) parallel folding.

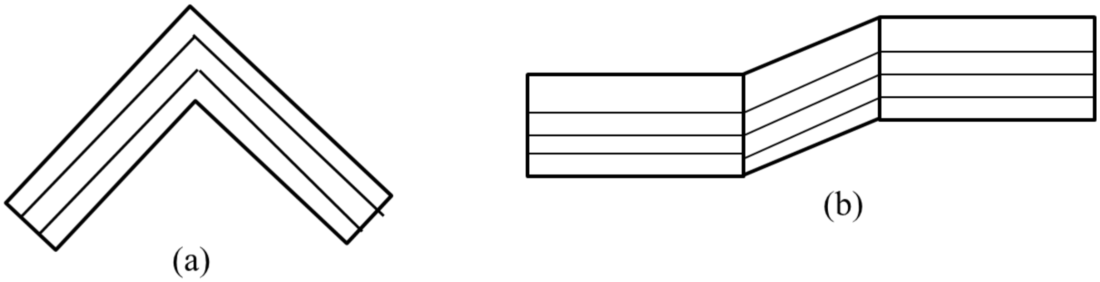

Figure 1.6 Schematics of a) in plane (or chevron type), and b) out of plane kink bands

Formation of shear bands in macrograined oriented Ti_3SiC_2 has also been reported by Barsoum and El-Raghy [4]. Following this, Zhang and Sun[63] used a Mohr-Coulomb criterion to analyze the shear band formations in MAX phases based on the angles observed experimentally. It was observed that larger grain sizes lead to lower values of shear fracture stress and therefore it can be concluded that shear bands are expected to be a mode of deformation in macrograined MAX polycrystals. In the vicinity of the shear bands, damage mechanisms such as grain bending, decohesion, pull-out, push in and crack deflections were also observed[10]. More recent studies and the work presented in this dissertation have shown evidence of brittle modes like transgranular / intergranular cracking, and cleavage fracture. Furthermore, the work presented herein along with concurrent work by other researchers in the area has shown evidence of grain-grain interactions and importance of mesoscale in the deformation response of polycrystalline MAX phases. At high temperatures, similar microstructural features of deformation are observed. However, the formation of open irrecoverable stress-strain loops under cyclic loading implies that IKBs are not operative – that is to say, the IKBs are converted to fully formed KBs based on the theory proposed by Barsoum et al. [18]. EBSD studies by Barcelo et al. [64] showed evidence of uneven deformation at the grain scale in post-creep tested coarse grained Ti_3SiC. Misorientation maps obtained from EBSD analysis showed co-existence of heavily deformed grains in a neighborhood of undeformed or intact grains.

The results presented herein and most recent reports in the literature [40, 65, 66] point towards three broad categories of deformation modes at the meso-scale operative over a range of strain-rates (10^{-4} – 10^{3} s^{-1}). To briefly summarize, these are as follows: i) elastic modes followed by brittle modes such as transgranular, intergranular cracking, and cleavage, ii) conventional basal slip or ductile modes, and iii) pseudo-ductile modes of kinking, delamination, and grain decohesion, . It must be noted that mechanisms like KB formation and delaminations are classified as damage mechanisms in fiber composites [13,14] but since these mechanisms allow for more deformation compared to conventionally brittle modes, they are categorized as pseudo-ductile modes in context of MAX phases. Therefore, they are believed to contribute towards the damage tolerant behavior in an otherwise brittle material at room temperature [10].

1.4 Outline of the thesis

This chapter presents an introduction to the material class being characterized in this dissertation i.e. the MAX phases. Two representative MAX phases which show desirable properties in the context of withstanding extreme loading conditions are characterized using experimental methods coupled with state of the art in situ imaging techniques. In this dissertation, the experimental protocols and necessary modifications required for testing polycrystalline Ti_2AlC and Ti_3SiC_2 under high strain-rates is established. Furthermore, the microstructural features are analyzed before and after deformation to establish microstructure-property relationships. In light of the most recent results (presented here and in the literature), it is observed that mechanisms at the length scale of grains as well as grain clusters are of relevance in a polycrystalline MAX phase. The microstructural landscape consists of several factors that need to be considered to provide a complete understanding of the deformation mechanisms in MAX phases. In this dissertation, a 3D numerical model is presented that takes into account some of the factors that have been commonly observed in a MAX phase microstructure, such as geometry, material anisotropy, multi-axial loading and nature of constraints due to neighboring grains.

The following is a brief summary of the content of each chapter in this dissertation:

2. Experimental methods and materials. This chapter describes the processing methods (performed at Texas A&M University), material compositions thus obtained and the fundamentals of experimental techniques used for characterization i.e. Split Hopkinson Pressure Bar (SHPB) and Digital Image Correlation (DIC) techniques.

3. High strain-rate response of Ti_2AlC. Material-specific experimental protocols and geometry optimization for high strain-rate testing is outlined following which the macroscale response of Ti_2AlC under high strain-rates is enumerated, along with description of microstructural origins of deformation. The results show a retention of pseudo-ductile properties under high strain-rates.

4. High strain-rate response of Ti_3SiC_2. Fundamental material differences between Ti_2AlC and Ti_3SiC_2 necessitates certain experimental modifications to the classic SHPB technique, which are outlined in this chapter. This is followed by the response of Ti_3SiC_2

under different strain-rates or test velocities. Extensive kinking, similar to Ti_2AlC wasn't observed post dynamic testing. However, there was evidence of grain refinements that pointed towards underlying delaminations.

5. Heterogeneous strain evolution in Ti_2AlC and Ti_3SiC_2. The full field technique of DIC used in the experimental analysis showed heterogeneous strain fields, as mentioned earlier in this chapter. A quantification of the spatial distribution of strains along with microscopic origins is provided herein that reveals the role of grain clusters in polycrystalline Ti_2AlC and Ti_3SiC_2.

6. Deformation modes in idealized multi-layered grains. A 3D numerical formulation capturing the compressive/bending/buckling deformation modes in MAX phases (and any multi-layered grain by extension) is proposed here, which captures the grain scale response and takes into account the several distinct cases for a grain in a polycrystalline MAX phase. The results conform in part to some of the recent theories on the continuum representation of MAX phase grains.

Chapter 2: Experimental methods and materials

2.1 Introduction

In this chapter, we present the details regarding the processing methods, sample preparation techniques and experimental set-ups used for characterizing the two representative MAX phases, Ti_2AlC and Ti_3SiC_2. The processing technique[2] and information regarding material compositions are briefly outlined in section 2.2. The fundamental principles underlying the Split Hopkinson Pressure Bar (SHPB) technique and Digital Image Correlation (DIC) are enumerated in sections 2.3 and 2.4 respectively, along with specific details of equipment used to generate the results presented in this dissertation. The specific details pertaining to development of testing protocol for the two different MAX phases are presented in subsequent chapters.

2.2 Materials and processing methods

Commercial MAXthal powders (Sandvik Technologies, Sweden) were processed into cylindrical discs using Spark Plasma Sintering (SPS) and pressureless sintering methods at

---

[2] Bulk MAX phases were processed by Dr. Miladin Radovic's research group at Texas A& M University. Impurities present in the sample can be linked to commercial powders used and/or decomposition occurring during processing.

temperatures of 1300°C (for Ti_2AlC) and 1325°C (for Ti_3SiC_2) at a heating rate of 50°C / min and load of 100 MPa. The grains had a rectangular plate like shape for both materials, with an average length in the range of 15-18 μm for Ti_2AlC, and 20-32 μm for Ti_3SiC_2. For both materials, widths of the plate like grains were 3-5 μm. However, there was a distribution of grain sizes in the microstructure with lengths ranging from 10-100 μm [3]. Secondary and intermetallic phases are often formed during processing due to impurities present in the commercial powders[67], used as starting materials. Table 2.1 provides an estimate of the amount and type of secondary phases present in the samples presented here. It must be noted that the current processing capabilities and in house powder processing methods have led to a drastic reduction in impurity content to less than 1% (for details, see [40]).

As-processed cylindrical discs were machined into smaller discs using Electrical Discharge Machining (EDM) for mechanical testing. ASTM C773-88 (for ceramics) and ASTM E-9 (for metals) standards were used as preliminary guidelines. The quasi-static tests were performed using a MTS® servo-hydraulic testing machine at strain rates of 10^{-3} -10^{-4} s^{-1}, and the high strain-rate experiments were performed in the range 3-5 x 10^3 s^{-1} for Ti_2AlC, and 5 x 10^2 - 1.5 x 10^3 s^{-1} for Ti_3SiC_2, using a Split Hopkinson Pressure Bar (SHPB) set-up.

---

[3] Standardized grain size range determinations were performed at Texas A &M University.

Table 2.1: Processing routes, secondary phases and content in the samples tested (data courtesy of Rogelio Benitez and Dr. Miladin Radovic, TAMU)

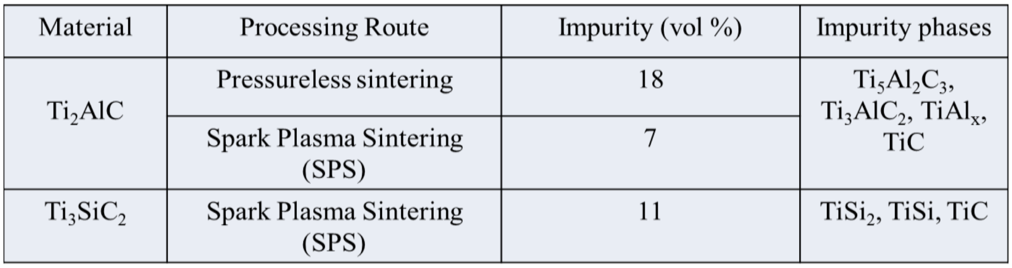

Material	Processing Route	Impurity (vol %)	Impurity phases
Ti_2AlC	Pressureless sintering	18	$Ti_5Al_2C_3$, Ti_3AlC_2, $TiAl_x$, TiC
	Spark Plasma Sintering (SPS)	7	
Ti_3SiC_2	Spark Plasma Sintering (SPS)	11	$TiSi_2$, TiSi, TiC

2.3 Split Hopkinson Pressure Bar (SHPB) fundamentals and set-up

The Split Hopkinson Pressure Bar (SHPB) or Kolsky Bar technique is a wave propagation technique first developed by Kolsky in 1949 to study high strain-rate mechanical behavior of isotropic materials such as polyethylene, synthetic rubber, and copper[68]. A large number of metals, ceramics, polymers, and composites have been widely studied using this technique since its development. The technique consists of applying a stress-wave to a specimen, sandwiched between two long bars. The dimensions and properties of the bars are designed based on the material being tested and therefore determination of material class specific protocols is crucial [69-77]. In the classical SHPB test setup, data acquisition relies on two strain gages on each of the bars. Therefore, some limitations in general could arise because measurements are not made directly on the specimen – i.e. the method relies on an inference technique[69]. The experimental data analysis assumes specific specimen-bar interface conditions (similar mechanical impedances, etc.) and linear elastic response of the bars to obtain material response data using conventional wave analysis techniques (see Section 2). Uncertainties in the strain-rate and strain calculations can therefore be induced by improper bar-specimen interface effects. To minimize this and ensure dynamic equilibrium, proper specimen design and fabrication is a crucial part of establishing the experimental protocols. There are no global rules for specimen design, that is to say, influence factors are material specific. Since MAX phase materials are known to exhibit some plastic deformations combined with high strength and stiffness, specimen design protocols for both conventional ceramics and metals are used to provide initial guidelines [68, 70-74, 76-78].

A schematic of the SHPB experimental set-up for testing Ti_2AlC is shown in Figure 2.1(a). In the experimental set-up, a short cylindrical specimen is placed between two case hardened stainless steel bars, the incident bar and the transmission bar. A third bar, much shorter in length, is used to strike the incident bar at a known velocity, using a pneumatic pressure system which leads to generation and propagation of a compressive stress wave pulse. The incident bar has a length of 1.83 m and the transmission bar has a length of 1.22 m. The length of the striker bar is 305 mm. The diameters of all the bars are 12.7 mm, with an elastic modulus of 220 GPa and an ultimate tensile strength of about 2 GPa.

As the traveling stress wave pulse reaches the specimen-bar interface, a portion gets reflected back and the remaining portion gets transmitted through the specimen into the output (transmission) bar. The bars are instrumented with strain gages to measure the wave pulses, which are analyzed to obtain stress and strain in the specimen. If there is no dispersion, one dimensional wave theory can be used to deduce the material response from the signals thus obtained. The strain gage on the incident bar records the incident and reflected strain pulses (ε_i and ε_r); the gage on the transmission bar records the transmitted strain pulse (ε_T). This theory relates the particle velocity at the two specimen-bar interfaces to the measured pulses. It is inherently assumed that the stress is equilibrated at the interfaces and often referred to as dynamic equilibrium. The stresses at the two interfaces are given by:

$$\sigma_1 = \frac{A_b}{A_s} E_b(\varepsilon_i + \varepsilon_r), \tag{2.1}$$

$$\sigma_2 = \frac{A_b}{A_s} E_b \varepsilon_T \tag{2.2}$$

The condition of dynamic equilibrium requires that $\sigma_1 = \sigma_2$ and is crucial for a valid SHPB test.

It has been shown that the amplitudes of reflected and transmitted pulses are proportional to the axial strain-rate and axial stress in the specimen (Eqns. 2.3 & 2.4) respectively; integrating the strain-rate with respect to time gives the axial strain in the specimen (Eqn. 2.5). The equations for strain-rate, strain and stress in the specimen are given by:

$$\dot{\varepsilon}(t) = 2\frac{C_0}{L}\,\varepsilon_r(t) \quad , \tag{2.3}$$

$$\varepsilon(t) = \int_0^t \dot{\varepsilon}\,(\tau)\mathrm{d}\tau \,, \tag{2.4}$$

$$\sigma(t) = \frac{A_b\,E_b}{A_s}\;\varepsilon_T(t)\,, \tag{2.5}$$

where $\dot{\varepsilon}(t)$ is the strain-rate in the specimen, c_0 is the longitudinal wave speed through the bar material, L is the length of the specimen, $\varepsilon_r(t)$ is the reflected wave-pulse obtained from strain gage 1 (see Fig 2.1(a)). The time-variable is represented by t and τ is a dummy variable for integration. The elastic modulus of the bar material is E_b, cross-sectional areas of the bars and the specimen are given by A_b and A_s respectively. In deriving Eqn.2.3, there are five major assumptions: i) the specimen deforms homogeneously during the experiment, ii) the stress pulses (reflected, transmitted) undergo minimal dispersion, and iii) the bars remain elastic at all times, with the ends of bars in contact with the specimen remaining flat and parallel, iv) a constant strain-rate is attained, and v) a dynamic stress equilibrium condition is achieved. A detailed derivation of the equations can be found elsewhere [12].

The conventional SHPB set-up is coupled with a high speed camera (Photron® SA5) to capture the deformation events during loading. Figure 2.1(b) shows an image of a Ti_2AlC specimen before loading. The camera is operated at a frame rate of 124,000-150,000 frames per second (fps) for the high strain-rate experiments reported herein. The images captured in-situ during the high strain-rate experiments are fed into commercial software ARAMIS® for Digital Image Correlation (DIC) analysis to measure strains, further details regarding which are mentioned later in this chapter.

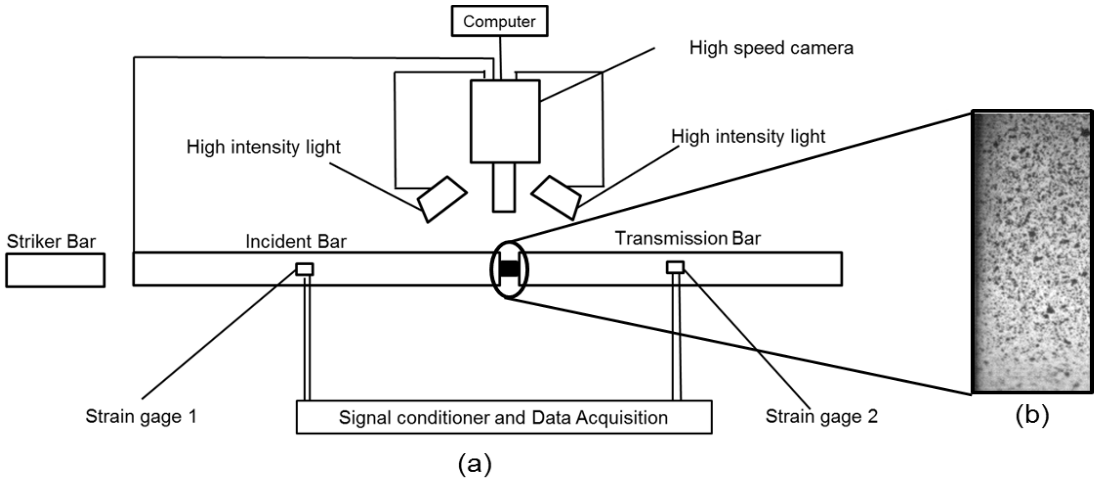

Figure 2.1 Split Hopkinson Pressure Bar (SHPB) experimental set-up showing (a) the high speed camera (Photron®SA5), instrumented bars, Ti_2AlC specimen, data acquisition system, and (b) speckled image captured at 131,250 frames per second (fps) prior to loading.

Broadly speaking, both Ti_2AlC and Ti_3SiC_2 belong to the class of MAX phases (or KNE solids based on their quasi-static response) but preliminary testing of Ti_3SiC_2 using a SHPB set-up showed appearance of indents at the bar-specimen interface, which were not observed in the case of Ti_2AlC [1]. Therefore, a modification was introduced to the set-up by using impedance matched alumina disks between the Ti_3SiC_2 samples and the bars, as shown in Figure 2.2.

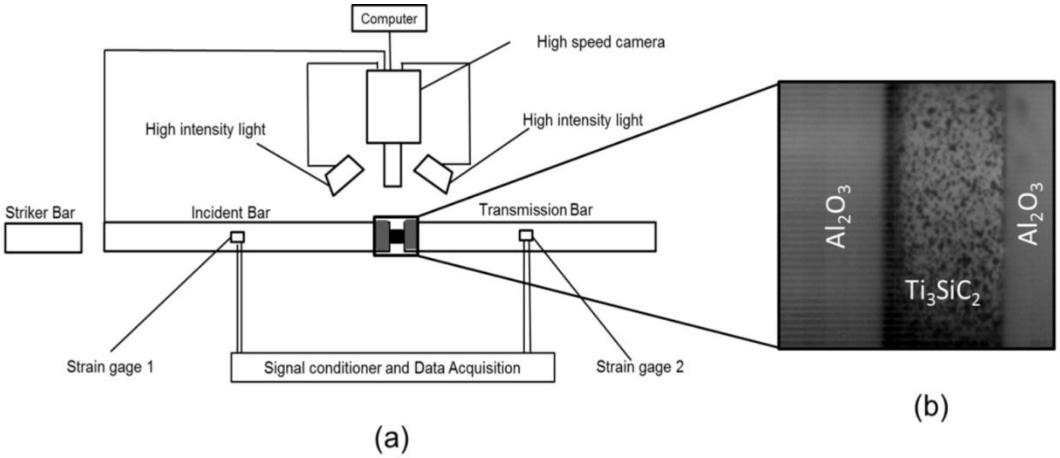

Figure 2.2 Split Hopkinson Pressure Bar (SHPB) experimental set-up for testing Ti_3SiC_2 showing (a) schematic of the high speed camera (Photron®SA5), instrumented bars, specimen, alumina anvils, and data acquisition system, and (b) speckled sample and alumina anvils captured at 150,000 frames per second (fps) prior to loading.

2.4 Digital Image Correlation (DIC): Principles and set-up

DIC is an image based, full-field, non-contact technique used to measure displacements and strains. In this method, a series of images captured in-situ are processed using an algorithm which measures displacements and performs strain calculations by tracking a random and high contrast pattern (known as a speckle pattern) on the specimen surface[79, 80]. This method enables visualization and thereby quantification of localized strain fields, which provides a means of determining spatial heterogeneity[81]. A key advantage of this method is that it relies solely on the contrast pattern and there is no inherent length scale i.e. strain measurement resolution can be refined by applying speckle patterns of different sizes at multiple length scales[82]. For example, specialized techniques such as UV photo-lithography have been developed to achieve suitable contrast at very small length scales[83]. Depending on the scale probed, insight into the nature of macroscopically observed phenomena can be gained[84-86]. Because of this, DIC has emerged as a powerful tool in understanding fundamental mechanisms of deformation in the last few decades.

The DIC method can be broadly categorized into two types: two-dimensional (2D) and three-dimensional (3D) DIC. 2D DIC has a relatively simple set-up (consisting of a single camera), reduced post-processing time, and does not induce triangulation or calibration errors as may be the case with 3D DIC. In 2D DIC it is assumed that: i) the specimen surface is planar before and during the deformation, and ii) out-of-plane motions are minimal or negligible[87]. 3D DIC is commonly used at the macroscale and is based on using stereovision to perform correlation on a pair of images[79, 87]. This method involves calibration of the camera sensor using an optimization process in which a calibration target is imaged in various orientations. 3D DIC involves a relatively cumbersome setup with either 2 synchronized cameras or a single camera with suitably positioned mirrors[88]. The key advantage of this method over 2D DIC is that it can be used to make measurements on curved surfaces for large[89] or small objects[90]. However, it is important to ensure that the cameras are synchronized spatially and temporally i.e. at a given time, both cameras should be imaging the same region on the sample surface[87].

The experimental results for quasi-static tests presented in this dissertation were analyzed using both 2D and 3D DIC. In situ images captured the progression of deformation events using i) a Nikon® D2X (with a 105 mm lens), and ii) two Grasshopper (GRAS-505SM-C) cameras (with 75 mm lenses) for 2D and 3D DIC analysis, respectively and operated at frame rates of 1-5 frames per second. Figure 2.3 (a) shows a representative Ti_3SiC_2 specimen used for testing under quasi-static loading conditions. Speckle patterns are applied on polished samples using paint, which are tracked in the DIC analysis to measure the strains. It is ensured that the contrast is resolvable by optimizing the speckle sizes. This is experimentally determined by trial and error, until a reasonable contrast is obtained. Figure 2.3 (b) shows the corresponding histogram for the sample shown in Fig. 2.3 (a). It is observed that the distribution of pixel intensities (or gray-levels) is uniform and unimodal (containing one peak). A bimodal gray-value distribution is indicative of more energy in the high wave number range, which leads to higher interpolation errors [30]. Therefore, a smooth transition between black and white ensures minimal errors [16,17,24]. The images obtained in situ are fed into the commercial software, ARAMIS® to obtain strain fields.

The resolution of strain calculations is dependent on a) the resolution of the lens-camera system, and b) software parameters such as facet, subset, and step sizes. While the camera-lens system determines the spatial resolution i.e. length-pixel relationship, the software parameters determine the grid size and the distance between the grid centers (step size), on which the correlation is performed at various stages of deformation. Table 2.2 summarizes the camera parameters – Field of View (FOV) and optical resolution for Ti_2AlC and Ti_3SiC_2, tested under quasi-static loading conditions. Smaller FOVs ensure a higher optical resolution, based on which the sizes of strain heterogeneities can be correlated to the underlying microstructure. These specifications are important in assessing the strain fields and correlating them to physical deformation mechanisms. For example, taking Ti_2AlC tested under quasi-static conditions, the field of view is 13.6 x 6 mm and the optical resolution per pixel is 13.2 microns per pixel. These values are later used to calculate the average number of grains in a pixel and hence in a subset. A subset is a 3 by 3 pixel array used to sample the speckles. A certain number of subsets combined together gives the facet size, which is the resolved region for calculating strain and gives an indication of strain smearing using this method. That is to say, one can identify the physical length-scale (number of grains or sub-grain) associated with the calculated strain at a point. For the results presented in this dissertation, the facet sizes are 13-16 pixels, which comprises of an area of ~200-300 μm. This is the region over which strain is smeared and corresponds to fewer than 10 grains. Further details regarding the analysis method and results are presented in Chapter 5.

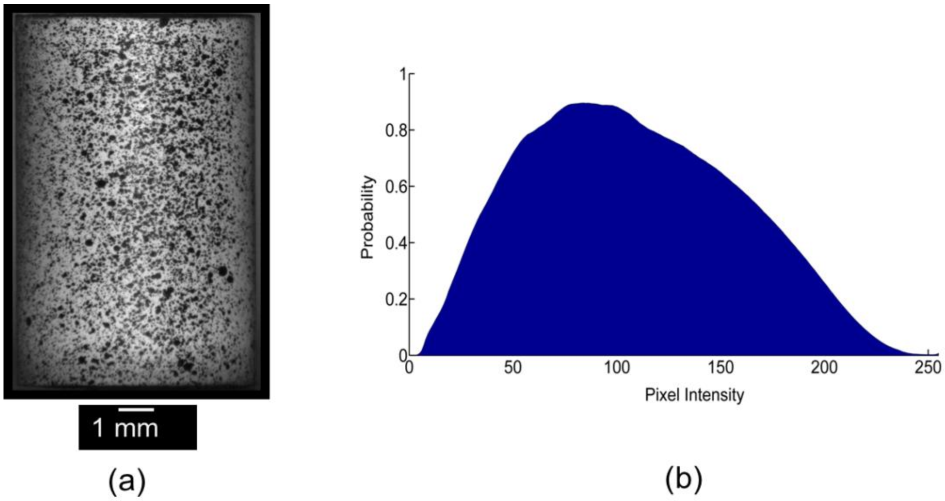

Figure 2.3 a) Typical speckled Ti_3SiC_2 specimen and, b) the corresponding histogram, which indicates unimodal distribution of pixel intensities on the sample surface.

Table 2.2: Field of view and optical resolutions for different sample sizes / camera magnifications.

Material	**Strain-rate (s^{-1})**	**Field of View - Sample (mm x mm)**	**Optical Resolution (µm / pixel)**
Ti_2AlC	$10^{-3} – 10^{-4}$	13.6 x 6	13.2
Ti_3SiC_2	$10^{-3} – 10^{-4}$	13.3 x 7	19.1

Chapter 3: High strain-rate response and mechanisms in Ti_2AlC

3.1 Introduction

The unique combination of properties in MAX phases makes them potentially suitable for applications involving impact and high temperature loading conditions because of their exceptional damage tolerance as compared to conventional ceramics. Ti_2AlC is one of the most promising representative members of the MAX phase family due to its low density and relatively lower cost of raw materials required for processing [3]. These properties coupled with excellent oxidation resistance and high temperature stability makes it particularly suitable for applications in aerospace structures, such as hypersonic jets. Characterization of Ti_2AlC under quasi-static loading conditions (10^{-6}-10^{-3} s^{-1}) over a range of temperatures has been widely reported, as mentioned earlier (see Chapter 1). In this chapter, the high strain-rate response of fully dense, pressureless sintered Ti_2AlC is presented. Herein, specific testing protocols for deducing constitutive response of Ti_2AlC under high strain-rates is elucidated (section 3.2) followed by a detailed analysis of the stress-strain response over a range of strain-rates (section 3.3). The chapter is concluded by correlating the macroscale stress-strain response to microstructural features observed before and after deformation (section 3.4).

3.2 SHPB Test Protocol

A critical aspect of high strain-rate testing using SHPB is developing the experimental protocols, in which proper specimen design plays a crucial role. Typically, cylindrical specimens are used for SHPB tests in which the length to diameter aspect ratio ($L_s : D_s$) is a design parameter. Different design requirements for softer materials[73], ductile metals [74, 75, 78] and ceramics[76-78] have been reported in the literature. For example, an aspect ratio between 1.0 and 2.0 [70, 71, 76-78] is recommended for ceramics whereas annular specimens have been used for softer materials [1]. These modifications are primarily introduced to eliminate frictional and inertial effects, the two major sources which lead to improper pulses. A robust specimen design essentially relies on minimizing these effects (to satisfy the homogeneous deformation assumption) while ensuring stress equilibrium condition in the specimen. According to Davies and Hunter, the interfacial and frictional effect corrected stress in the specimen is given by [7]:

$$\sigma^C(t) = \sigma^M(t) + \rho_s \left[\left(\frac{L_s^2}{6} \right) - \left(\nu_s \frac{D_s^2}{8} \right) \right] . \frac{\partial^2}{\partial t^2} \epsilon(t), \tag{3.1}$$

Where superscripts C and M indicate corrected and measured respectively. The subscript S indicates the parameters associated with the specimen, i.e. length (L_s), diameter (D_s), density (ρ_s) and Poisson's ratio (ν_s). Equation 3.1 is derived by balancing the specimen kinetic energy with work done by external forces, during the deformation. For a specimen design to account for this effect the corrected stress should be equal to the measured stress and the second term in Eqn. 3.1 would vanish. Incorporating this condition ($\sigma^C = \sigma^M$) in Eqn. 4, the optimal condition for specimen aspect ratio reduces to:

$$\frac{L_S}{D_S} = \sqrt{\frac{3\,\nu}{4}}\,. \tag{3.2}$$

Using a value of ν=0.2[91] for Ti_2AlC, the optimal aspect ratio based on this relationship is 0.38. Testing Ti_2AlC specimens using this aspect ratio resulted in very small deformations leading to a very small reflected pulse and hence the material response could not be deduced (see Fig 2(b)). This is a common problem often encountered in ceramics. It must be noted that the specimen diameters were the same as the bar diameter for these initial experiments. This condition is conventionally used to ensure uniaxial one-dimensional stress wave propagation through the bars and specimen. Gray et al. [8] however suggested that by slightly reducing the diameter and tailoring specimen aspect ratios, the frictional and inertial conditions can be minimized without violating the one-dimensional stress state. Furthermore, relatively thinner specimens can be used to minimize stress non-equilibrium in the specimen. Nemat-Nasser showed that introducing pulse-shapers to prolong the loading pulse can generate an appreciable strain signal in ceramics[72]. Following these suggestions and guidelines, iterative experiments conducted on different aspect ratios[92] led to an optimal range for appreciable deformations in Ti_2AlC without any premature pulverization. This condition is particularly important for brittle materials such as ceramics since they show little strain prior to fracture, usually on the order of 1%[76]. The results from iterative experiments to determine experimental protocols for testing Ti_2AlC in the strain-rate regime ~3-5 x 10^3 s^{-1} are summarized in Table 3.1. For each testing condition, two samples were tested.

Table 3.1: Specimen dimensions and strain rates reported in this dissertation (Diameter of bars=0.5 inches)

Specimen Diameter (D_s, mm)	Specimen aspect ratio (L_s : D_s)	Strain Rate (s^{-1})
9.52	0.52	3310
9.52	0.25	2895
6.35	0.35	2715, 2980
6.35	0.25	2620, 4670

The typical pulse shapes for a Ti_2AlC specimen with optimized geometry tested at ~3500 s^{-1} is shown in Fig. 3.1(a). The strain wave pulses obtained are smooth without much observable noise, which qualitatively suggests that dispersion is minimal. The reflected pulse shows a characteristic trapezoidal shape, which indicates attainment of a constant strain-rate plateau (see Eqn. 2.2) as observed typically in ductile metals[2,3]. From this observation, it is inferred that Ti_2AlC exhibits pseudo-ductile behavior at high strain-rates (contrary to typical ceramics) and the stress-equilibrium condition can be ensured by tailoring specimen sizes appropriately (Table 3.1). Figure 3.1(b) shows a typical pulse shape for a specimen that showed a sharp, small triangular shaped reflected pulse. These were determined to be unsuitable for deducing accurate constitutive responses (since they do not deform under a *constant* strain-rate) and hence discarded. The stress equilibration time can be estimated using the following relationship[93]:

$$t = \frac{nL}{c}, \tag{3.3}$$

where t is the time for equilibrium, n is the number of wave reflections before equilibrium is achieved, L is the length of the specimen and c is the calculated wave speed in the specimen. The value of n is typically 4 based on experimental and theoretical considerations. This value is indicative of the number of reflections that a wave pulse is subjected to at the bar-specimen interfaces, before equilibrating. Using this value in Eqn. 3.1, the approximate theoretical estimate is calculated as 2.62 μs. The small equilibration time is facilitated by using thinner specimens, which also allows testing at higher strain-rates (see Eqn.2.2). In conventional ceramics, it has however been observed that dimension reductions often result in frictional and inertial effects, thereby violating the one-dimensional stress state[76]. To minimize this and ensure dynamic equilibrium, modifications in specimen geometries and experimental set-up have been proposed. Yet it has been observed that some ceramics such as SiC, TiB_2, AlN cannot be tested beyond critical strain-rates in the range 2500-3000 s^{-1}. Figure 3.1 (c) shows a typical stress and strain-rate versus time response for a Ti_2AlC specimen at a strain rate of ~3.5×10^3 s^{-1}. It is observed that a Ti_2AlC specimen with optimized geometry stays in stress-equilibrium for a comparably large amount of time (~100μs) as compared to conventional ceramics. The stress-strain response of Ti_2AlC is deduced from the equilibrated regime and presented in the subsequent section.

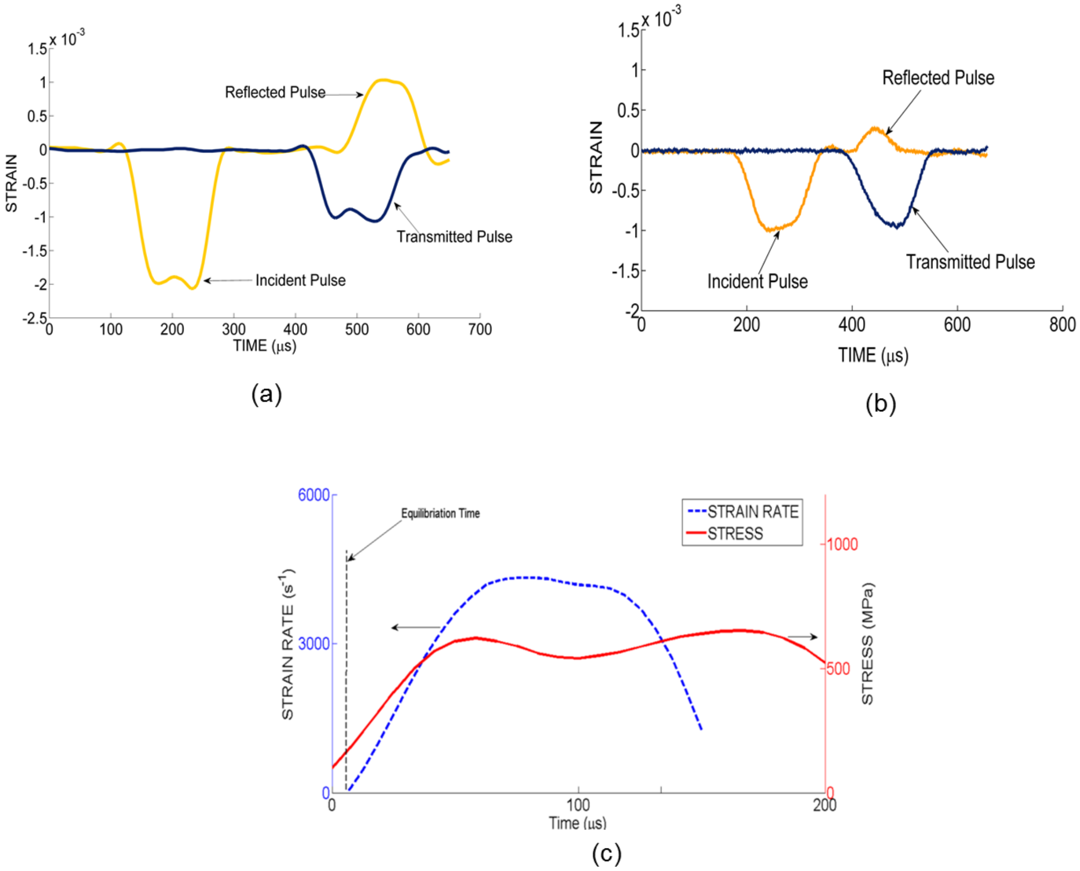

Figure 3.1 Typical strain wave pulses for incident and transmitted bars, showing reflected pulses with (a) trapezoidal shape and, (b) sharp triangular shape. (c) Strain-rate and stress versus time for a Ti_2AlC specimen loaded at strain-rate of 3500 s^{-1}.

3.3 High Strain Rate Behavior of Ti_2AlC

The response of Ti_2AlC under compressive loading at strain rates in the range 3-5 x 10^3 s^{-1} is outlined in this section. Figure 3.2(a) shows a typical average axial strain versus time response obtained by comparing the strain gage wave analysis and DIC calculations. The average strain from DIC calculations are in good agreement with the conventional wave analysis technique (average error of ~ 2% and variance of 1.4% for two samples per test condition) up until the macroscale cracks form. Figure 3.2(b) shows the corresponding stress-strain response for Ti_2AlC at ~3000 s^{-1} which reveals a large strain regime with maximum compressive strains of ~25%. Whilst, strains of the order of ~ 5% or higher have been observed under quasi-static loading of the MAX phases under high temperatures[15] , strains on the order of 25% at high strain rates are certainly unexpected[15, 22, 94]. The question arises if such large strains at high strain-rates are *real* strains. In this case, the use of *in-situ* imaging becomes highly critical. Our DIC results show that the excessive strains are an artifact induced by the formation of micro-cracks and delaminations.

The strain measurement in the DIC technique relies on contrast differences in the speckled specimen surface (see Fig. 2.1(b)). The crack formation process is accompanied by a loss of contrast around the cracked region, which leads to erroneous calculation of strains. Due to this, the average strains calculated from DIC show an abrupt jump at the point of cracking (confirmed from in-situ high speed images) whereas the wave analysis technique shows a monotonic increase up to 25% strain. Based on this analysis, the constitutive stress-strain response is truncated to delineate real strains as shown in Fig. 3.2(b) (5% in this case). For all specimens tested, the maximum average strains before *macroscopic* fracture are in the 4.5-7.5 %. However, it is likely that microscopic cracks form much earlier, propagation or growth of which are retarded by the pseudo-ductile modes, observed on the fractured surface.

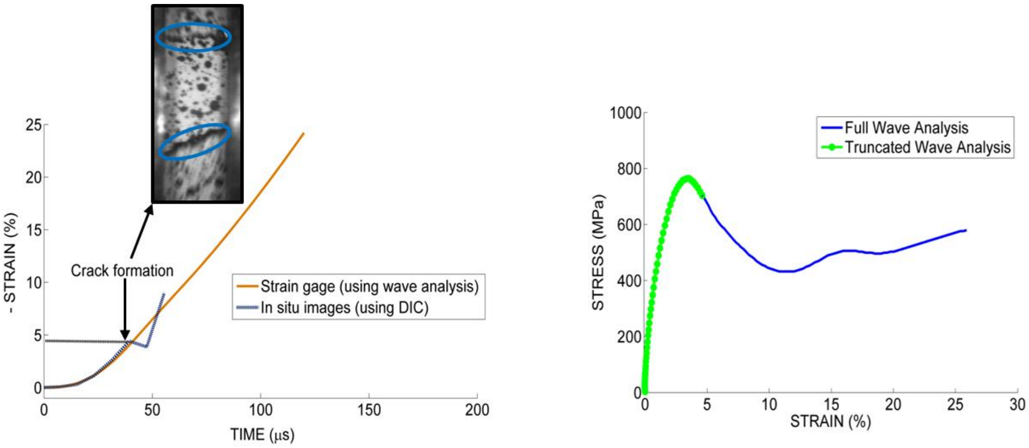

(a) (b)

Figure 3.2 a) Axial strain versus time signals measured from strain gage sensors (orange) and averaged from DIC analysis (blue) at 3 x10^3 s^{-1}. The strain at which cracking occurs is indicated in the plot. b) Full and truncated wave analysis for the same sample.

The strain-rate versus strain and the average stress-strain response for 12 samples of Ti_2AlC tested in the range 3-5 x 10^3 s^{-1} are shown in Figs. 3.3(a) and (b), respectively. In Fig. 3.3(a), the strain rate versus strain shows an initial linear regime followed by attainment of a plateau region, which indicates that the material deformed at a constant rate and the constitutive response corresponding to the rate can be obtained. For some strain-rates, a sudden drop and subsequent increase of the rate after the plateau region is observed. This is a qualitative indication of damage propagation in the specimen. A quantification of the exact strain values is achieved with the imaging technique, as discussed earlier.

Figure 3.3(b) shows the constitutive stress-strain response of Ti_2AlC. There is an initial linear regime at very low strains followed by a large non-linear regime leading to attainment of peak stresses and softening followed by macroscopic crack initiation (>=0.1

mm). The peak stress-values obtained at different rates are in the range 520-900 MPa. The transition of the non-linear regime to the peak stress is similar to plastic behavior, often observed in ductile metals. The *pseudo-yield* in MAX phases is caused by a combination of deformation mechanisms, primarily kink banding of the nano-layered structure - typically observed on the specimen fracture surface at higher magnifications (see Fig 3.7). Figure 3.4 illustrates the variation of peak stress in different samples at a given strain-rate. It is observed that the minimum variation between two samples is 16 MPa and the maximum variation is 118 MPa. It is observed that there is a variation in the peak stress values at similar strain rates. These differences in the type of responses and peak stress values can likely be attributed to a) different microflaw distribution, b) variations in the impurity phase concentration, c) grain size distributions, and d) machining induced defects (if any). The first three are microstructural variabilities whereas the last point is an experimental variability. To minimize the latter, flat surfaces of samples are fine ground and polished using 9 μm diamond paste. The former can be controlled and reduced by improving the processing technique, which has been reported in the most recent literature. The powders from which these compounds are fabricated and the processing route may induce these variations, as explained in the subsequent section (3.4). For comparison, the peak stress values under quasi-static loading are indicated from reports in the literature and summarized in Table 3.2. It is observed that the peak stress values do not increase significantly from quasi-static (10^{-4} s^{-1}) to dynamic strain-rate regimes (10^{3} s^{-1} or higher). Therefore, it is inferred that the response is not strain-rate dependent but variations in the peak stress values (and overall stress-strain response in general) are caused by microstructural features, induced during the processing of these compounds. A most recent report by Parrikar et al.[49] shows peak compressive strengths in the range 1427-1870 MPa , for spark plasma sintered Ti_2AlC tested at 500 s^{-1}. It must be noted that the samples used in their work had $TiAl_x$ on the order of 7 %, which is lower than the amount of secondary phase content in samples used in this dissertation. Furthermore, the grain diameters are on the order of 4.2 µm, which is finer than the grain sizes for the samples presented herein (see Section 3.4 for further details). Therefore, the higher peak compressive strength could be attributed to a Hall-Petch type behavior.

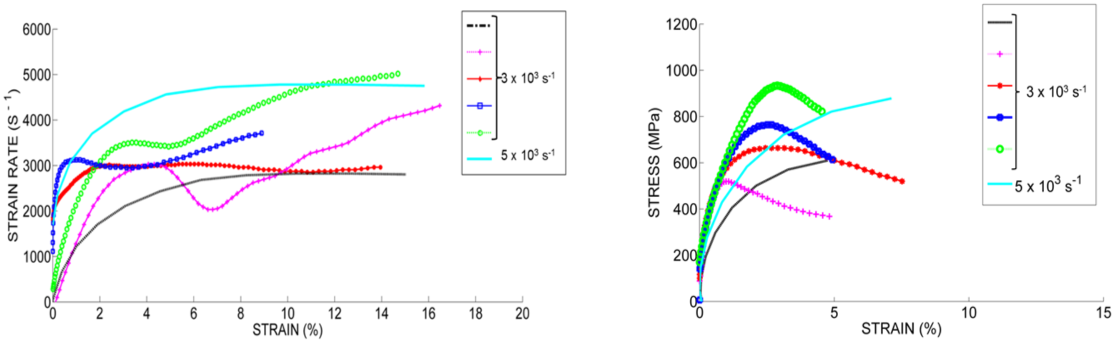

(a)

(b)

Figure 3.3 (a) Strain-rate versus strain behavior, and (b) average stress-strain response of Ti_2AlC in the regime 3-5 x 10^3 s^{-1}.

Table 3.2: Summary of properties of Ti_2AlC under dynamic and quasi-static compressive loading

Strain Rate (s^{-1})	Peak Stress (MPa)	Max. Compressive strain (%)	Reference
3×10^3	608 ± 59	4.7	This work
	517 ± 12.5	4.8	
	691 ± 28.3	7.5	
	755 ± 8	4.9	
	907 ± 27.5	4.5	
5×10^3	849 ± 29	7.1	
10^{-4}	763	4.8	[13]
10^{-4}	600	-	[95]

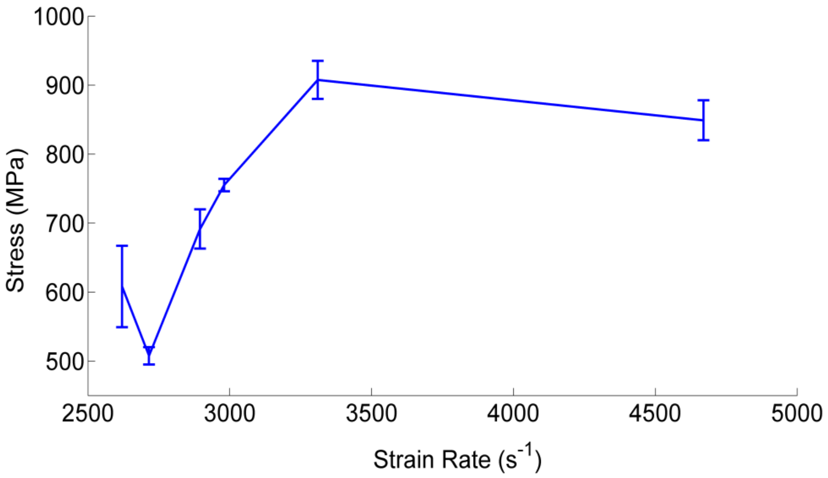

Figure 3.4 Peak stress versus strain-rate variation of Ti_2AlC under dynamic loading conditions. The error bars indicate variation in peak stresses from two samples at a given rate.

3.4 Microstructure and post-deformation failure analysis

Analysis of the phase composition on the as-processed specimens (not shown here) using X-ray diffraction (XRD) and SEM with Energy-Dispersive Spectroscopy (EDS) of polished but un-etched surfaces, showed that the majority phase in pressureless sintered samples was Ti_2AlC. However, the sample also contained up to 18 vol% $TiAl_x$ intermetallic and smaller amount of TiC, Ti_3AlC_2 and $Ti_5Al_2C_3$. Some amount of TiC, $TiAl_x$ and Ti_3AlC_2 impurities might originate from commercially available MAXtal 211 powders[95]. However, $Ti_5Al_2C_3$ and some amount of TiC, $TiAl_x$ and Ti_3AlC_2 phases are most likely formed as a result of decomposition of Ti_2AlC during pressureless sintering[95, 96]. SEM analysis of the etched surfaces revealed that the microstructure consists of plate-like grains with average grain lengths and widths of 16 μm and 4 μm, respectively. Second-phase particles (light gray) marked by arrows in Fig 3.5(a) can be seen on polished and etched surfaces were confirmed to be TiC using EDS analysis. The elemental composition of the rest of the phases (dark gray) in Figs. 3.5(a) and (b) corresponds to the MAX phases, i.e. Ti_2AlC, Ti_3AlC_2 or $Ti_5Al_2C_3$. It is worth noting here that the TiAl impurity phase cannot be observed in Figs. 3.5(a) and (b) as it was completely dissolved during etching. A magnified view of the equiaxed portion of the microstructure in Fig 3.5(b) also highlights the random orientations and polycyrstallinity of the specimens.

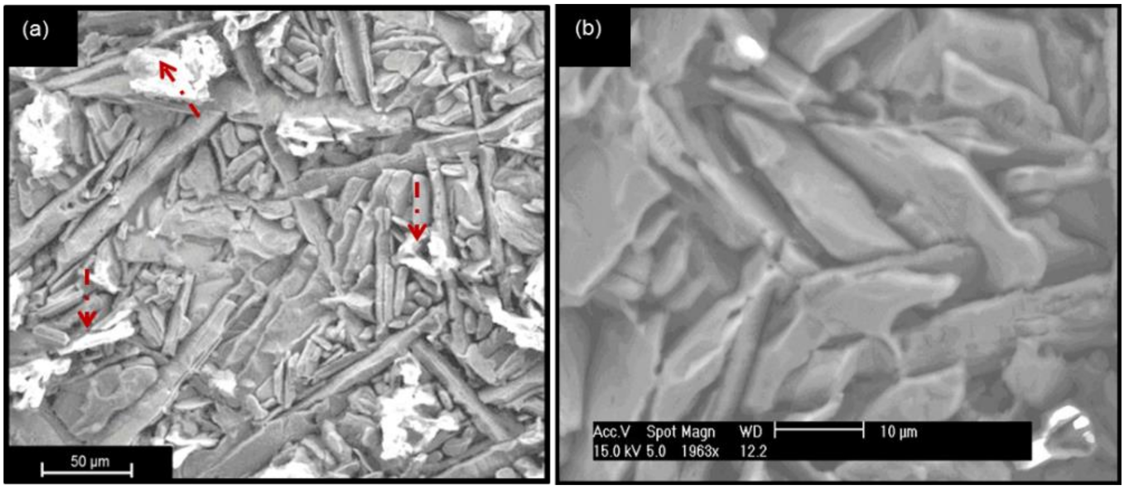

Figure 3.5 SEM micrographs of the polished and etched surfaces showing a) plate-like grains and second phase TiC particles, b) random orientation of equiaxed grains.

Images of deformed and fractured specimens obtained after high strain-rate loading are shown in Fig.3.6 and are representative of behavior observed in all specimens. Two types of fracture surfaces tested at approximately identical strain-rates were observed. Figure 3.6(a) shows a fracture surface with a large central flattened disc and primarily radial cracks of ~2 mm visible on the outer circumference (small particles released from the outer circumferential region). Secondary cracks with little dominant orientation were also present on the central flattened disc. In Fig.3.6(b), the circumferential regions were fragmented into sizes ranging from 0.5 mm - 2mm from the central flattened disc. As a comparison, under monotonic quasi-static loading at room temperature the specimens fracture by propagation of a single crack growing at a 45^o angle to the axis of loading [15, 97]. Since the material did not completely separate upon failure, it was inferred that Ti_2AlC is quasi-brittle at room temperature. At higher temperatures (for a strain rate of 10^{-4} s^{-1} at ~1100^{o}C), specimens compressed into flat pancake shapes[12] beyond the Brittle-Plastic

Transition (BPT) temperature. The fact that Ti_2AlC retains some structural integrity at high strain-rates (up to ~ 3000 s^{-1}) at ambient temperatures indicates that microscale damage mitigation mechanisms are operative. The diameters of the central flattened portions obtained post-deformation are observed to be in the range 10-13 mm, which indicates an increase of up to 70% with respect to the initial size (see Table 3.1)

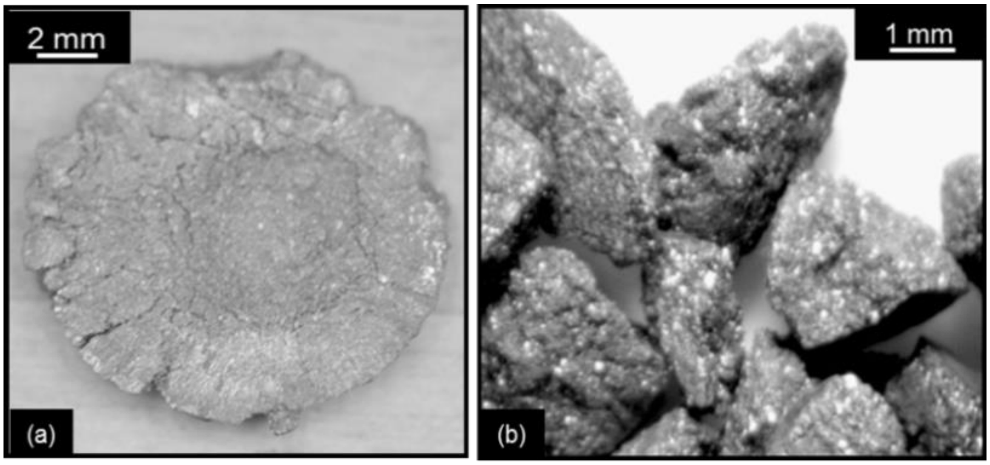

Figure 3.6 Fractured specimens after high strain-rate loading showing a) *pseudoductile* type deformation where crack formations are observed with flattening out of the cylindrical disc, b) pulverized particles from circumferential region indicating a brittle type fracture, tested at 3 x 10^3 s^{-1}.

Herein, specific microstructural mechanisms are proposed which govern the macroscale stress-strain response (Figure 3.3(b)) observed under high strain-rates. Figure 3.7 shows fractured surfaces observed under higher magnification using SEM. At relatively low magnification levels, a lamellar structure with void formations (see Fig 3.7(a), marked by white circles) are observed. Due to extensive formation of kink bands accompanied by inter-layer delaminations (see Figs. 3.7(b) and (c)), the fracture surface microstructure seems to have a refined appearance (Fig. 3.7(a)) in comparison to the initial microstructure (Fig. 3.5(a)). A kink banded region is typically 1-2 μm thick with each nano-layer having thicknesses in the range 150-250 nm. The angle at which a kinked region is oriented with respect to its boundaries is in the range of 40^o-80^o, as shown in Figs. 3.7(b) and (c)).

Figures 3.7(d)-(f) show the co-existence of lamellar and cleavage regions, intergranular delaminations, translayer and transgranular cracking, and grain pullouts. Among these, kink bands, and interlayer delamination, are the most extensive and unique features believed to be responsible for the observed pseudo-ductility and damage mitigation in MAX phase materials.

Since MAX phases in general have a hexagonal crystal structure, polycrystalline Ti_2AlC does not possess the five independent slip systems[2, 3], required to maintain microscale integrity during deformation. In other words, it does not undergo classic yielding due to plastic slip and dislocation glide is limited only to the basal planes. However, these dislocations can easily multiply in these materials to arrange themselves in arrays and walls leading to the formation of Kink Bands (KBs), as reported by Barsoum et al.[2, 3, 12]. Hess and Barrett[61] first reported dislocation based kink band formations in hcp Zinc (Zn) and proposed that the collapse of several dislocation walls into a small region leads to kink boundary formations. The type of kink band that was observed is known as the stove-pipe kink, which is similar in structure to the kink band shown in Fig 3.7(c). Barsoum et al.[98] building on the kinking model developed by Frank and Stroh[62] proposed that kink bands evolve from a precursor, usually referred to as an incipient kink band (IKB) - a recoverable kinking phenomenon that can be thought of as buckling of the nanolayers within a grain.

As deformation progresses, the walls bounding the IKBs detach and form Mobile Dislocation Walls (MDWs) eventually leading to the formation of fully formed KBs.

In relatively unfavorable orientations (hard grains), the deformation is believed to proceed by more brittle modes such as pull-out of nano-laminated grains and transgranular cracking. The observations are similar to features observed under quasi-static loading where delaminations, kink band formations, transgranular cracking and grain pullouts have been reported[4]. But it is the simultaneous occurrence and retention of the ductile modes, which are believed to be key mechanisms governing the *pseudo-ductile* response in these high strength ternary ceramics at high strain-rates.

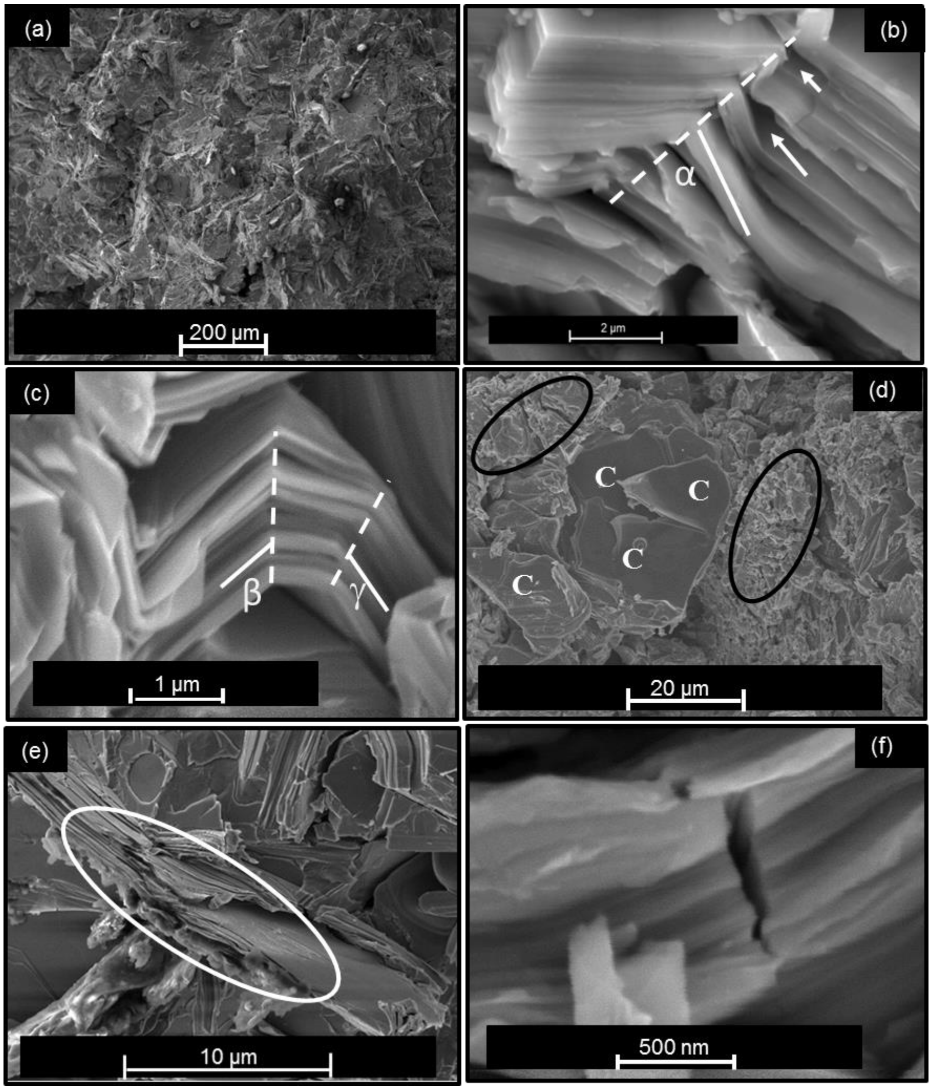

Figure 3.7 Morphological characteristics of dynamically loaded fractured surface of Ti_2AlC showing a) overall refined appearance of the microstructure, and void formations, b) and c) kink band formations at slightly higher magnifications with $\alpha=75^o$, $\beta= 50^o$ and $\gamma=60^o$ (arrows indicating delaminations), d) Co-existence of smooth cleavage and lamellar regions, e) pulled-out nanolayer grain structure, and f) transgranular cracking.

3.5 Conclusions

Ti_2AlC is a 211 type MAX phase known to exhibit a unique combination of properties of conventional metals and ceramics. In this chapter, the high strain-rate response of Ti_2AlC was evaluated experimentally using the well-known SHPB technique. From a systematic experimental analysis it was determined that cylindrical samples with aspect ratios (L_s : D_s) in the range 0.25-0.5 and diameter ratios in the regime 0.5-0.75 (diameter of specimen : diameter of bar) should be used to accurately test Ti_2AlC (and similar materials) in the range 3-5 x 10^3 s^{-1}. Peak stresses are in the range of 520-900 MPa, without any particular trend with respect to strain-rate variations. It is believed that the variations in micro-flaw and impurity phase concentrations are responsible for the scatter in the values. Recent work on fine grained Ti_2AlC (processed using spark plasma sintering method) has shown peak compressive stresses of up to 1870 MPa is achievable at strain-rates on the order of ~500 s^{-1}.

Microscopic analysis of the fractured specimens reveals a combination of brittle and ductile fracture modes. The ductile modes are likely mechanisms for damage mitigation and the exceptional *pseudo-ductility* of Ti_2AlC at high strain-rates.

Chapter 4: High strain-rate response and mechanisms in Ti_3SiC_2

4.1 Introduction

Bulk Ti_3SiC_2 is the most well characterized MAX phase that are known to be elastically stiff (elastic modulus of 322 GPa), a good thermal and electrical conductor, and resistant to chemical attack while being machinable, thermal shock resistant, and softer than their binary counterpart (SiC)[2]. A brittle-to-ductile transition type behavior at high temperatures (1000-1100^{o}C) while withstanding stresses of up to 1GPa has also been reported[18]. Most recent reports on Ti_3SiC_2 are aimed at optimizing and improving the mechanical properties by fabricating composites with other metals and Shape Memory Alloys (SMAs) due to their suitability for high temperature structural applications. Similar to Ti_2AlC, reports to date concerning the deformation response of Ti_3SiC_2 have been mostly performed under quasi-static conditions. To date, only one study on the ballistic impact response (at a velocity of 380 m/s) of hot pressed Ti_3SiC_2 have been reported in the literature[48]. However, the response of Ti_3SiC_2 under dynamic loading conditions (10^2-10^4 s^{-1}), often encountered in aerospace and defense related application has not been extensively reported in the literature. In this chapter, the SHPB technique is suitably modified (section 4.2) to experimentally characterize Ti_3SiC_2 under dynamic loading conditions. A description of the set-up is followed by analysis of the macroscale response (section 4.3) and microstructural characteristics (section 4.4).

4.2 Specimen geometry optimization

The development of experimental protocols for testing materials under high strain-rates involves optimizing specimen geometry to ensure the attainment of stress equilibrium in the sample [69, 72, 76-78, 99, 100]. That is to say, aspect ratio and diameter of the cylindrical sample are varied systematically using an iterative testing procedure. Based on the discussion in the previous chapter, experimental protocols for testing Ti_2AlC, in concert with reports on conventional ceramics such as SiC [11, 72], Al_2O3[77], AlN [101] are used as an initial guideline for systematically tailoring the geometry.

Since brittle materials like ceramics don’t yield, they are relatively more susceptible to stress concentrations, which arise from: i) insufficient smoothness of loading surfaces, ii) misalignment of bars, and iii) indentations of the hard specimen material into the compliant bar at the interfacial regions. Stress concentrations combined with the inability to yield lead to premature failure and one of the objectives of optimizing the specimen geometry is to remove factors leading to it. The advanced machining technique and fine grinding procedure (see chapter 2) ensured flatness of the loading surfaces, and the introduced alumina (Al_2O_3) platens (see Fig. 4.1) accounted for minimizing any stress concentration effects due to indentations. An alternate way to tackle the problem of indentations is to use dumbbell shaped specimens, which have been studied by Chen et al.[100], and have shown promising results. However, achieving high quality machined surfaces of dumbbell specimens in a hard material like Ti_3SiC_2 is not a feasible cost-effective option. The selection of platen material is based on two criteria [78] – first, the platen should be structurally stiff to withstand impact, and secondly, the mechanical impedance should be nearly identical to that of the bars. Therefore, the geometries of the platens also need to be optimized accordingly once a platen material is selected. The platen sizes used for the experiments reported herein had a diameter of 12.7 mm (equal to that of the bars) and a nominal length of 4.8 mm. Figure 3 shows the strain signals obtained from calibration (bar on bar) tests after introducing the Al_2O_3 platens to the conventional test set-up. It is observed that the incident and the transmission pulses align closely with negligible amplitude of the reflected pulse. This implies that the platen does not affect wave propagation through the bars; therefore no additional corrections to the conventional 2-wave analysis are necessary.

A pulse shaping technique [72, 78] was also applied by placing copper discs at the impact end of the incident bar i.e. the surface closer to the striker bar. This ensures a ramping up of the load, attainment of dynamic equilibrium in the samples and circumventing the issue of premature failure, a common issue when testing ceramics due to the lower strain levels, as mentioned earlier. Dynamic equilibrium conditions for the different geometries are checked by comparing front end and back end stresses. Figures 4.2(a) and (b) show representative stress histories in two samples, tested at similar velocities but using different specimen geometries (aspect ratio and diameter ratios). Therefore, the strain-rates are expected to be different. The condition of equilibrium is checked by comparing stress ratio, R defined as follows [76]:

$$R = \left|\frac{\sigma_f - \sigma_b}{\sigma_m}\right| \ldots\ldots\ldots\ldots\ldots\ldots\ldots\ldots\ldots\ldots\ldots\ldots\ldots\ldots\ldots..(4.1)$$

The results indicate a large R value for a sample tested with protocols similar to Ti_2AlC (Fig. 4.2(a)), whereas further optimization of the geometry leads to a reduction of R values in the range 0.01-0.02, as shown in Fig. 4.2(b). Here, the response (section 4.3) for $R < 0.05$ is reported, although some reports in the literature report up to R values 0f 0.1[78].

Theoretically speaking, at a nominal specimen length of 6.35 mm, the longitudinal wave takes 0.75 μs and therefore the theoretically predicted stress equilibration time is 3 μs, based on a procedure given in [76]. Therefore, the R values are calculated for times greater than 3 μs. Furthermore, it was also checked that the samples are in equilibrium when peak stresses are attained (50-100 μs). A summary of the aspect ratios, diameter ratios and R values (expressed in percentage) are presented in Table 4.1. The geometries shown in bold font are the optimal ones which resulted in lower R, thereby indicating dynamic equilibrium for a significant time. Diameter ratios, defined as the ratio of specimen diameter to bar diameter (D_s:D_b), lying in the range 0.5-0.7 and aspect ratio in the range 0.5-1 are found to be suitable for achieving longer equilibrium times.

The amplitude of signal from the transmission bar is typically used to measure stress in the specimen. A propagating stress pulse changes in amplitude with propagating distance leading to a phenomenon called geometric dispersion. Dispersion in propagating stress waves can lead to a violation of the stress equilibrium condition that is highly critical for testing brittle materials using the SHPB technique. The likelihood of dispersion effects increase with higher strain-rates and lower times to failure (as typically encountered in a ceramic), thereby leading to discrepancies in the true material response. Ravichandran and Subhash[76] proposed a law to determine critical strain-rates beyond which such inconsistencies in data are likely to occur. For the range of optimal specimen sizes presented here and failure strains observed, the critical strain-rate for Ti_3SiC_2 is found to be 2784 s^{-1}. The nominal strain-rate values obtained for the tests presented here are much lower than this value and hence it is concluded that the results do not contain any wave dispersion effects. Furthermore, the validity of the assumptions is checked by comparing the front and back end stresses (Fig. 4.2) and comparing strain measurements using two different methods, as outlined in the subsequent section.

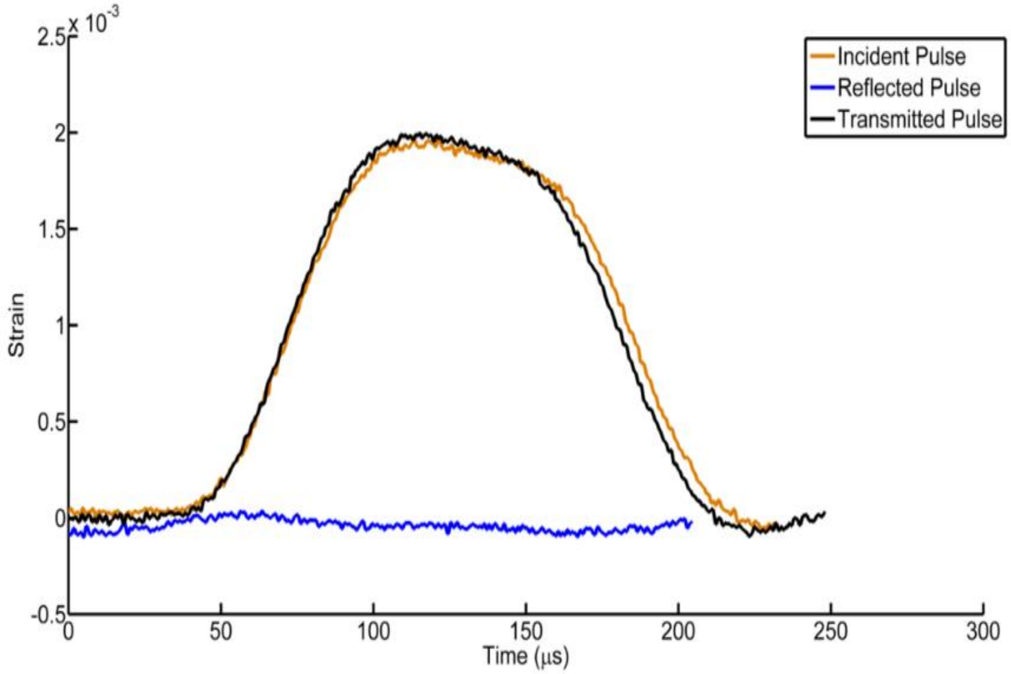

Figure 4.1 Typical strain wave pulses obtained by introducing alumina discs of suitable size between the incident and transmission bars.

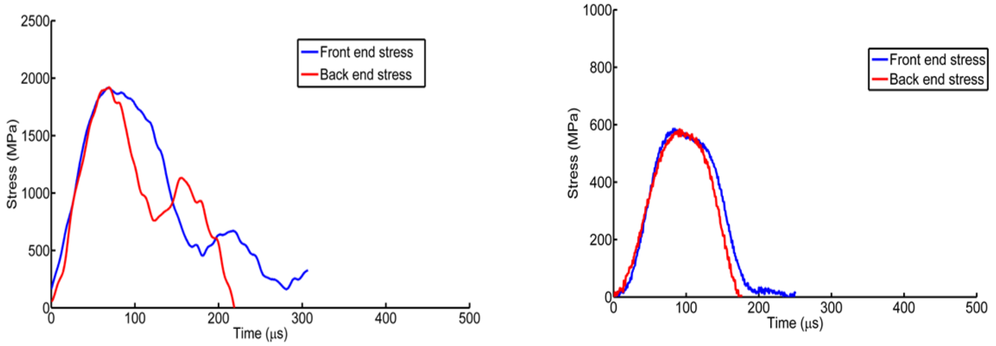

(a) (b)

Figure 4.2 Representative stress-time responses for Ti_3SiC_2 tested at 40 m/s showing results from (a) initial experiments, and (b) optimized geometries.

Table 4.1: Specimen geometries of Ti_3SiC_2 used for testing under high strain-rates. The geometries in bold font indicate the optimal range. Diameter of bar (D_b) =12. 7 mm

Aspect Ratio (L:D)	Diameter Ratio (D_s:D_b)	Mean error (%)
0.3	0.5	20.8
0.4	0.7	11.3
0.5	0.8	9.2
0.5	**0.7**	**1.7**
0.5	**0.5**	**2.4**
1	**0.5**	**3.2**
1	0.4	13.2

4.3 Dynamic Response of Ti_3SiC_2

The strain-rate, stress, and strain histories of Ti_3SiC_2, tested at different striker velocities in the range 30-45 m/s is presented in this section. It must be noted that in contrast to Ti_2AlC, Ti_3SiC_2 had a smaller range over which strain-rate was constant, even with optimized geometries. The reason for this is attributed to the inherent brittle nature of Ti_3SiC_2 which promotes microscopic crack formations. A linear strain versus time is ideal and indicative of constant strain-rate (given by slope). However, reports in the literature on classical ceramics such as SiC [11, 72], Al_2O_3 [99] have shown an overall parabolic type response, from which a near-linear portion is selected to calculate the strain-rate (see [72]). The strain versus time response for Ti_3SiC_2 shows a similar behavior and therefore the velocity of striker bar is used as a metric. Stress or loading rate has been also used as a metric for several conventional ceramics reported in the literature ([69, 72, 77, 78, 99]) where strains are on the order of 1% or smaller. However, since the strains observed here are slightly higher, nominal strain-rates based on a regression analysis performed on strain histories (see Fig. 4.3)is reported.

The traditional inferred wave analysis technique, typically used to measure strains in a SHPB test, can cause some inaccuracies when applied to classical ceramics due to the lower strains and their inability to yield in general [72, 78].To circumvent this issue, use of sacrificial strain gages, as a means of monitoring sample strain directly, have been reported [72, 76]. Herein, we make use of the image based, non-contact, high speed DIC technique, which can provide a direct measurement of the strains on the sample surface. The average strain is calculated using DIC to the traditional inferred technique and error on the order of 5 % is observed between the two sources of measurement.

A typical strain versus time response for Ti_3SiC_2 is shown in Figure 4.3, which reveals a i) near linear average strain response calculated using the two methods, and ii) a large deviation between the two methods at the point of (and beyond) surface crack formation. A linear strain versus time response is indicative of a constant strain-rate and is desirable. It is observed that the strain-time response is nearly linear at lower strains but becomes non-linear with increasing strains. This is confirmed by using a linear regression analysis, the slope of which is used to determine the nominal strain-rate (1225 s^{-1} in this case) attained in the material.

The DIC method relies on tracking the speckle pattern (see Fig. 2.3(a)), with progressing deformation and minimizing a correlation function to measure displacements, based on which pointwise strain calculations are performed, mentioned earlier in the dissertation (for further details see [79]). Accuracy of strain calculations performed using this method relies on the quality of speckle pattern. For the experiments reported herein, the quality of the speckles was checked by analyzing the histogram (See Fig 2.3(b)). The jump in DIC measurements is observed due to discontinuities caused by surface crack paths, which distort and render the speckle pattern unsuitable for correlation (for details, see chapter 5). The in situ captured image shown inset clearly reveals these crack paths. A representative transverse strain field (ε_y) is also shown in this figure, which reveals high strain localizations (red portions) at the regions where cracks are observed in the subsequent frame. Therefore, the technique is reliable only up until the point of fracture or visual distortion of the speckle pattern. Furthermore, the method can provide information about strain localizations along with the overall average strains, which makes it powerful over conventional methods like strain gages. The DIC method, used in conjunction with standard wave analysis, can therefore circumvent some of the issues encountered in classical SHPB analysis and provide additional useful information regarding the local strain fields.

The value of strain before the point of surface crack formation is treated as the maximum strain in subsequent analyses. However, it must be noted that internal cracks undetectable by the DIC method may occur at lower strain values, given the brittle nature of Ti_3SiC_2. Therefore, the strain values reported herein does not eliminate the effect of underlying microcracking. The average strains for the experiments reported herein, measured using the DIC method and the conventional wave analysis method, is compared. The comparison up to the point of crack formation gives an average relative error of ~11%, but the comparison is restricted to first change of slope in the DIC data (blue line in Fig 4.3), this error reduces to ~5 %.

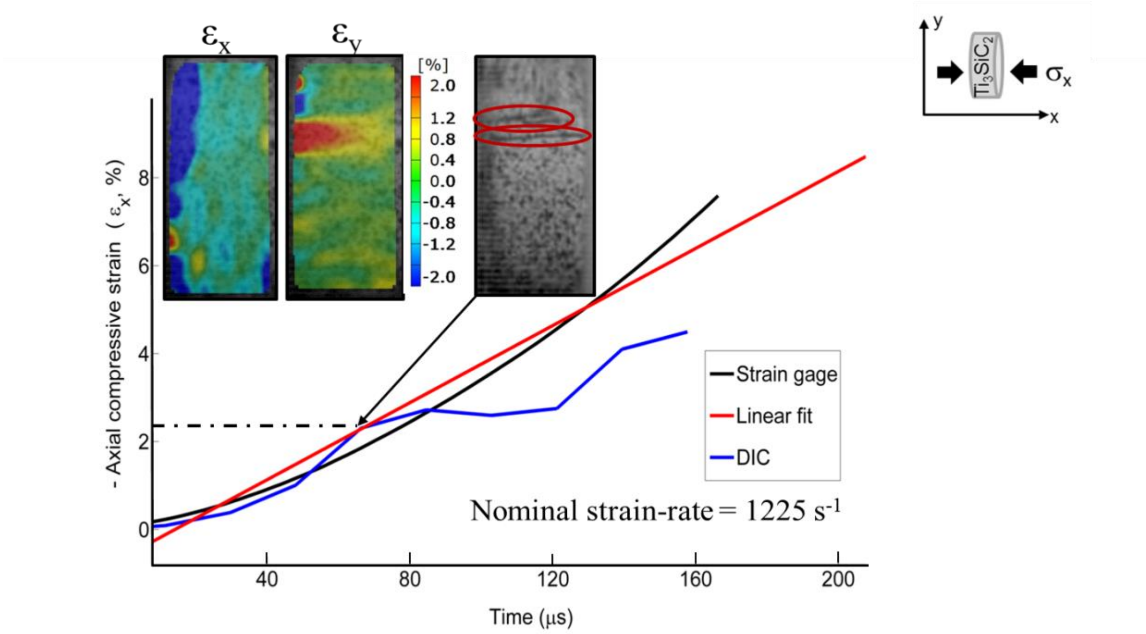

Figure 4.3 Typical strain-time responses for Ti_3SiC_2 tested at 42 m/s (nominal $\dot{\varepsilon}$=1225 s^{-1}) showing strain calculations from strain gage, DIC analysis and a linear regression analysis. Dashed line indicates the appearance of a surface crack, confirmed using high speed imaging (inset), and axial and transverse strain fields from a frame before surface cracks are observed.

The stress versus time response of Ti_3SiC_2, representative of the different samples tested at different velocities is presented in Figures 4.4 and 4.5. An analysis of stress histories of the different samples indicates two types of responses – a triangular response (see Fig.4.4) and an M shaped response (see Fig.4.5). Note that testing sample with similar dimensions at the same velocity results in one of the two behaviors. That is to say, the type of stress-time response does not correlate with test velocity.

Figures 4.4 and 4.5 illustrate characteristic stress-time and strain-rate versus time behavior obtained from testing at similar velocities (42m/s). Figure 4.4 shows the first kind of response (i.e. triangular response), wherein a marked downturn is observed after reaching the peak stress value. Figure 4.5 shows the second type of response, where a softening and hardening regime following peak stress attainment is observed. This leads to an M shaped appearance of the stress-time response. The strain-rate histories obtained from the two samples show an initial ramping. For the tests presented here, the sample with a triangular stress-time history (Fig. 4.4) has a more plateau like strain-rate versus time response, in contrast to the M shaped response (Fig.4.5).

In both triangular and M type responses, an initial upturn in the stress-time response is noticeable followed by a large linear regime and a downturn after the attainment of peak stress. The regimes are marked in Figs. 4.4 and 4.5 using vertical dashed lines. The transition stress values from the non-linear upturn into the linear regime lies in the range 100-230 MPa, and the transition stress from the linear regime into the non-linear regime before attainment of peak stress lies in the range 500-870 MPa. Note that the initial regime has a more pronounced non-linearity for the triangular response in comparison to the M type response.

The non-linear regime in the vicinity of the peak stress is reminiscent of yielding observed in classical metals. However, since slip in Ti_3SiC_2 (and MAX phases in general) is limited to basal planes only [2], yielding at the macroscale is not expected. Therefore, this phenomenon is defined as pseudo-yield, and has been observed in other MAX phases under high strain-rates [27] or at high temperatures [94]. It is acknowledged that the specific underlying causes for the two different types of responses are not clearly understood, based on the observations. To this end, recent advanced techniques such as X-ray or XDIC combined with SHPB [102] can possibly shed more light on the underlying mesoscale effects thereby furthering the understanding of deformation under high strain-rates. It is also worthwhile to note that this novel technique can quantify mesoscale heterogeneities, which have been shown to be relevant in polycrystalline MAX phases, as outlined later in the dissertation (Chapter 5).

It is observed that surface crack formations occur in the vicinity of peak stress attainment (Figs. 4.4 and 4.5 (a)-(c)). For both types of responses, cracks appear or seem to propagate in the direction of applied loading. Subsequent frames show an opening type separation of the crack faces in the transverse (y) direction, as shown in Figs. 4.4(b) and (c). This is reminiscent of a mode I type fracture. On the other hand, the M type response shows formation of numerous smaller cracks following appearance of the larger dominant cracks (similar to those observed for triangular response), as shown in Figs. 4.5(b) and (c). The images inset show the largest post-fracture fragments obtained post-fracture for the corresponding stress-time response (dust like finer particles are not shown here). It is observed that the fragments obtained following a triangular response are larger in size (~10 mm) compared to that from the M type response (~6 mm).

A stress derived strain versus time response is presented in Figs. 4.6(a) and (b) for the stress histories corresponding to Figs. 4.4 and 4.5 respectively. This response is obtained by normalizing the stress values with the elastic modulus value reported for Ti_3SiC_2 in the literature[2], assuming a linear elastic response. The objective of this analysis is to delineate what portion of the total strain accumulated in the sample is due to elastic strains in the classical sense. Radovic et al.[22] reported on cyclic loading-unloading tension tests in FG Ti_3SiC_2 under room temperatures wherein it was concluded that above 200 MPa, the macroscopic response is a combined effect of elastic, anelastic and plastic components.

The analysis presented here is aimed at quantifying the contribution of elasticity to the overall strain in the vicinity of peak stress attainment. It is observed that irrespective of the type of stress-time response (triangular or M type), maximum elastic strains for all samples in the vicinity of peak stress (in the pseudo-yield region) lie in the range 0.12-0.3%, which constitute 8-12% of the total strain accumulated in the sample. The peak stresses and maximum strains prior to macroscopic surface crack formation are presented in Table 4.2. No apparent trend of peak stress values with respect to test velocity or nominal strain-rates is observed although the strains prior to crack formation decrease with increasing velocity. Two samples are tested for each condition.

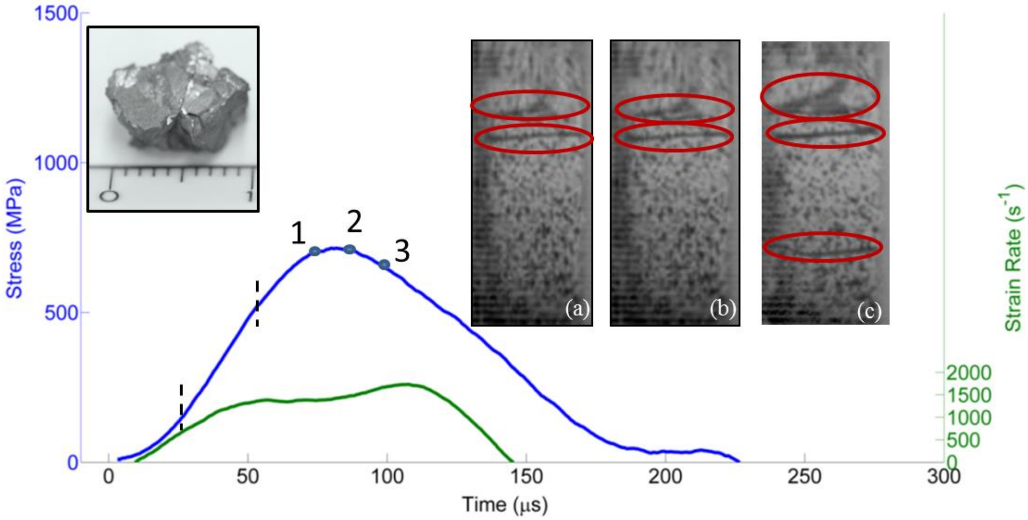

Figure 4.4 Stress, strain-rate histories, post-fracture fragment (inset) and in situ captured images of a Ti_3SiC_2 sample tested at 42 m/s, showing a characteristic triangular response and crack propagation in images (a), (b) and (c) at time instants corresponding to points 1, 2, and 3 on the stress-time plot. The red circles show cracked regions and the y-axes are color coded for clarity. The sample obtained post-fracture is shown inset.

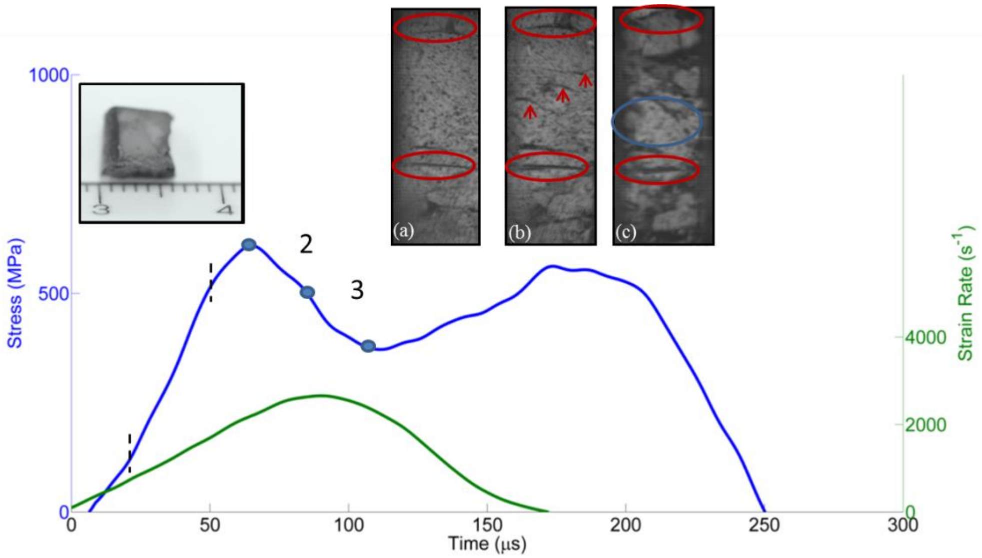

Figure 4.5 Stress, strain-rate histories, post fracture fragment (inset) and in situ captured images of a Ti_3SiC_2 sample tested at 42 m/s, showing a characteristic M shaped response and crack propagation in images (a), (b) and (c) at time instants corresponding to points 1, 2, and 3 on the stress-time plot. The red circles show cracked regions, red arrows indicate shorter cracks. The y-axes are color coded for clarity. The sample obtained post-fracture is shown inset.

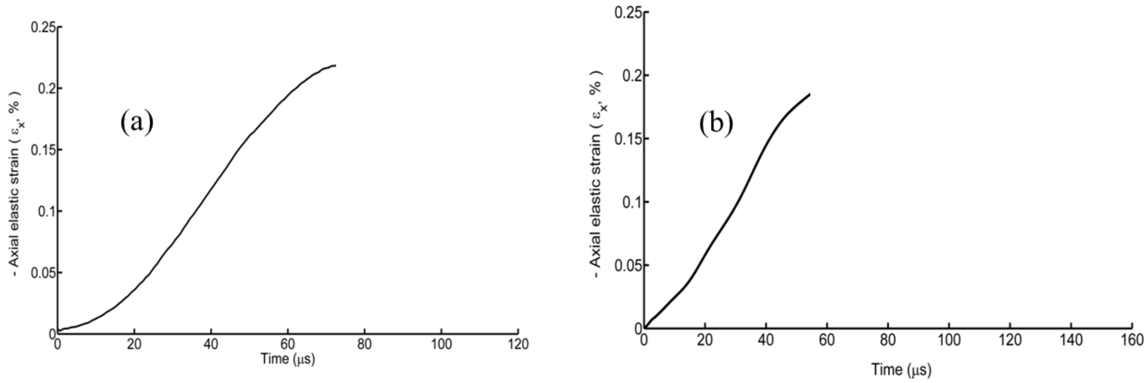

Figure 4.6 Stress derived axial elastic strain versus time for a) triangular response, and b) M type response, tested at a velocity of 42 m/s.

Table 4.2: Summary of test velocities, corresponding strain-rates and properties of Ti_3SiC_2

Velocity (m/s)	Nominal strain-rate (s^{-1})	Peak Stress (MPa)	Max. axial strain (%)
30	550	623 ± 151	4.1 ± 0.06
38	990	710 ± 92	3.3 ± 0.5
40	1090	830 ± 164	2.6 ± 0.24
42	1225	725 ± 21	2.2 ± 0.35
45	1420	729 ± 41	1.7 ± 0.15

The large scatter in the peak stress values can be attributed to polycrystallinity and inherent microscale inhomogeneity, typical of materials processed via powder metallurgy routes as mentioned earlier in the dissertation. Impurities in the powders from which the samples are fabricated often lead to secondary phases, such as $TiSi_x$ and TiC. These phases, in addition to pre-existing microflaws are likely sources which affect load carrying capacities of a sample, thereby leading to variations in bulk parameters such as peak stress. However, the variation in the types of responses (triangular and M shaped) observed for Ti_3SiC_2 cannot be ascertained to these parameters, given the localized nature of their occurrence. To this end, some larger scale flaws (for example, machining induced) can lead to variations in the response. The samples were fine ground and polished before testing to eliminate these sources and visual examination revealed no defects. Another likely source of the scatter in the peak stress values can be attributed to the grain size distributions. The tested samples had grain sizes in the range 20-32 μm with a few finer grains in the range 3-5 μm. It is possible that the samples showing higher peak stress had a greater proportion of finer grain sizes, by virtue of Hall-Petch effect, evidence of which has been observed in other MAX phases over a range of strain-rates [49]. This comment notwithstanding different grain sizes (and distributions) needs to be experimentally studied to confirm if such mechanism is indeed operative.

4.4 Microstructural analysis and fractography

Analysis of the SPSed samples are performed using X-Ray Diffraction , and scanning electron microscopy at TAMU. The results show that Ti_3SiC_2 was the primary dominant phase formed, along with some secondary phases like $TiSi_2$, TiSi, and TiC_x. Pores or microflaws were not apparently visible on the surface.

Figure 4.7(a) shows the typical XRD patterns in five SPSed samples by subjecting commercial powders to the conditions mentioned earlier (see section 2). The compositional analysis reveals that Ti_3SiC_2 is the predominant phase with 85% purity, containing up to 11% TiC, and 4% $TiSi_2$ as secondary phases. The impurities are introduced in the samples due to the commercial powders, Figures 4.7(b) and (c) show SEM micrographs obtained from polished and unetched surfaces, pointwise compositions of which are determined using Energy Dispersive Spectroscopy (EDS) analysis and summarized in Table 4.3.

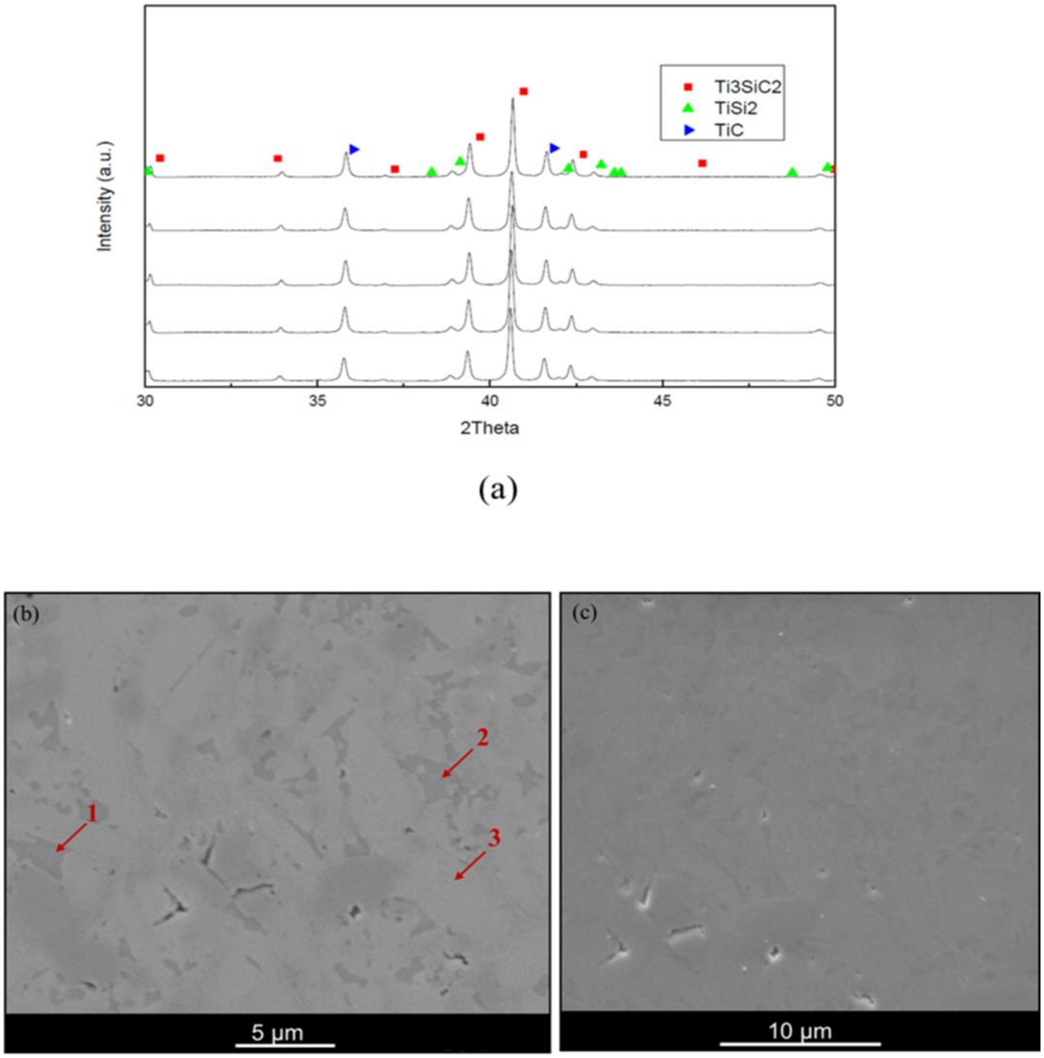

Figure 4.7 Characterization of as processed Ti_3SiC_2 samples showing a) XRD patterns obtained from different SPSed samples, and b), c) showing surface morphological features at different magnifications. The arrows point to the spots from which EDS data is collected and presented in Table 4.3 (Data and images courtesy of Rogelio Benitez and Dr. Miladin Radovic, TAMU)

Table 4.3: Energy Dispersive Spectroscopy (EDS) of the spots pointed out in Figure 4.7(b).

Spot	Ti	Si	C	Composition
1	31.3	67.2	0	TiSi2
2	34.5	47.2	16.5	TiSi
3	44.6	16.0	38.9	312

Typically, MAX phases deform by three categories of deformation modes: conventional slip (limited to basal planes), pseudo-ductile modes such as kinking and delamination, and brittle modes such as grain cracking, cleavage, etc. Herein, the fracture surface analysis of fragments, obtained after subjecting Ti_3SiC_2 samples to high strain-rates, is presented. Figure 4.8(a) shows a refined microstructure, which can be attributed to delaminations and some folding occurring at even higher magnifications (marked using arrows), as shown in Fig 4.8(b). Figure 4.8(c) shows coexistence of coarser regions at similar magnification levels. Some portions of the coarser region show cracks emanating in multiple directions (circled region), thereby indicating intergranular and transgranular cracking while other regions show extensive damage (rectangular region). Higher magnifications of the coarser regions, shown in Fig. 4.8(d), reveal grain push-outs (circled region), and cleavage type fracture (rectangular region). Shih et al.[11] reported on deformation and fracture mechanisms in the binary counterpart of Ti_3SiC_2 – SiC, and proposed a mechanism by which integranular cracking progresses in brittle materials under dynamic loading. This mechanism is related to existence of foreign or second phase particles, segregating at the grain boundaries, creating a localized strain field thereby leading to debonding or crack formations. Since the Ti_3SiC_2 samples had a significant portion of intermetallic secondary phases ($TiSi_x$) that are known to segregate at grain boundaries [27, 40], it is likely that a similar mechanism is operative here. The polycrystallinity in the samples result in different grains being oriented differently to the applied compressive loading, which combined with small amount of deformation result in incompatibility stresses, thereby leading to transgranular crack formation. It is worth mentioning that extensive kink band and buckle formations are not observed, which are ubiquitous in Ti_3SiC_2 post quasi-static loading[4, 7, 17]. Lo et al.[48] showed evidence of kinking of buckling but these regions are bounded by highly damaged or fractured regions (see Figs. 6(a) and (d) in [48]). Since, their experiments were performed at much higher velocity (380 m/s), the absence of kinking cannot be attributed to deformation rate effects. The samples used in their work were fabricated using hot pressing and higher purity levels, with TiC as the only secondary phase. In contrast, the samples presented here have a higher secondary phase content, which may have contributed to suppressing deformation via kinking. It is intuitively understood that coarser (or larger) grains favor kinking over finer grains [49] – the fact that the samples in this work has regions with grain sizes in the range 3-5 μm (not shown here) can be another likely cause. These comments notwithstanding a rigorous analysis of the role of grain sizes and grain size distributions on dynamic deformation mechanisms are required, which is a clear gap in the existing literature and a possible direction for future work. In summary, it is inferred that the pseudo-ductile modes of delamination and limited fold formations lead to a refined appearance of the microstructure, similar to Ti_2AlC and other MAX phases. The coarser regions, on the other hand, reveal the existence of brittle modes.

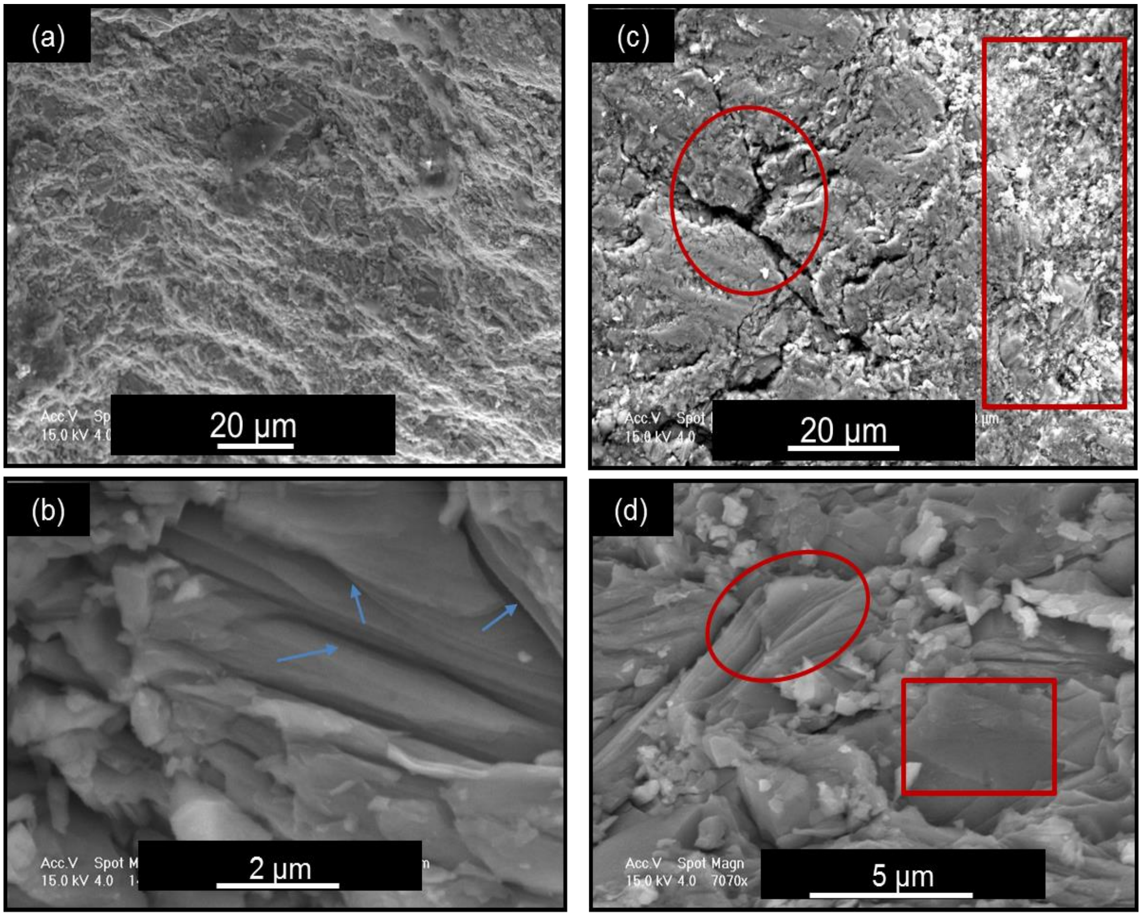

Figure 4.8 Post fracture SEM micrographs showing (a) a refined microstructure, (b) grain cracking and microcracking in multiple directions, (c) delaminated nano-laminates, and (d) evidence of grain push-outs and cleavage type fracture.

4.5 Conclusions

Ti_3SiC_2 is the most well-known representative member of the MAX phase family, which is known for excellent combinations of properties. Herein, the dynamic response of Ti_3SiC_2 was analyzed using the SHPB technique. The analyses presented here reveals Ti_3SiC_2 is relatively less damage tolerant than Ti_2AlC, the only other MAX phase that has been characterized in the similar strain-rate regime (10^2-10^3 s^{-1}). Suitable modifications to the experimental set-up are necessary for ensuring dynamic equilibrium, by optimization of specimen sizes and introducing additional platens. The inherent brittleness in Ti_3SiC_2 necessitates use of pulse shapers, which ensure a ramp type loading. The "cushioning" effect of the pulse shapers leads to slightly lower strain-rates for similar velocities. Ti_3SiC_2 is tested in the velocity range 30-45 m/s, which corresponds to strain-rates in the range 550-1420 s^{-1}. The peak stress values are in the range of 623-830 MPa, without any trend with respect to strain-rate (or velocity). Microscale analysis shows presence of secondary phases in the form of TiC and $TiSi_x$, although the predominant phase is Ti_3SiC_2. Post-fracture shows existence of brittle (transgranular cracking, grain pull-outs, etc.) and pseudo-ductile mechanism of delaminations, without any buckling or fold like formations. The absence of kink bands demonstrates lesser damage mitigation capabilities (compared to Ti_2AlC) under high strain-rate loading conditions.

Chapter 5: Heterogeneous strain field evolution in Ti_2AlC and Ti_3SiC_2

5.1 Introduction

The previous chapters outlined the macroscale response of two representative MAX phases under dynamic loading conditions along with elucidation of key features of deformation at the microscale. Average strain measurements using the full field technique of DIC was found to be critical for delineating real strains, which the inferred technique of two-wave analysis cannot capture. In this chapter, the strain field evolutions in Ti_2AlC and Ti_3SiC_2 are characterized over a range of strain-rates. This analysis facilitated the quantification of progression and accumulation of strain fields in the material that could be mapped as a function of time and stress levels. Combining the results of macroscale DIC analysis with microstructural characterizations before and after deformation, affirms the role of grain-grain interactions in the deformation of polycrystalline MAX phases at the mesoscale.

5.2 DIC methodology & validation

For DIC, images during the deformation are captured in situ and fed into the commercial software (ARAMIS® by Trillion Systems) for computing displacements and strain fields. Each image is characterized by its grey level in this space, and the mechanical transformation between the reference image grey level and the deformed image grey level is approximated using an interpolation (or shape) function. The coefficients or parameters of the shape function are obtained by finding values of the shape function for which the correlation coefficient is minimized[79, 87, 103, 104]. The correlation function is defined as:

$$C\ (\Phi) = 1 - \frac{\sum_{i=1}^{m}\sum_{j=1}^{m}[f(x,y)-\bar{f}].[g(x^{*},y^{*})-\bar{g}]}{\sqrt{\sum_{i=1}^{m}\sum_{j=1}^{m}[f(x,y)-\bar{f}]^{2}.\sum_{i=1}^{m}\sum_{j=1}^{m}[g(x^{*},y^{*})-\bar{g}]^{2}}}, \tag{5.1}$$

$where$ $\Phi = (u,\ v,\ \frac{\partial u}{\partial x}, \frac{\partial u}{\partial y}\ , \frac{\partial v}{\partial x}, \frac{\partial v}{\partial y}\ )$ contains all the deformation parameters. The function f(x, y) is the grey level for reference image coordinate (x, y) and g(x*, y^{*}) is the grey level for the target or deformed image coordinate (x*, y*). The deformed and reference coordinates are related to each other as follows:

$$x^{*} = x + u + \frac{\partial u}{\partial x}\Delta x + \frac{\partial u}{\partial y}\Delta \tag{5.2a}$$

$$y^{*} = y + v + \frac{\partial v}{\partial x}\Delta x + \frac{\partial v}{\partial y}\Delta y. \tag{5.2b}$$

The quantities $\bar{f}$ and $\bar{g}$ represent the average grayscale values of reference and deformed images, respectively. The mechanical transformation Φ(x) between the reference image grey level ($f(x)$) and the deformed image grey level ($g(x)$) is approximated using an interpolation (or shape) function. The coefficients or parameters of the shape function are obtained by determining values of Φ for which the correlation coefficient is minimized. For the strain calculations presented here, a linear interpolation is used. The components of the strain tensor in Eqn. 5.3 are obtained by numerically differentiating the displacement fields:

$$\epsilon = \begin{bmatrix} \frac{\partial u}{\partial x} & \frac{1}{2}\ (\frac{\partial u}{\partial y} + \frac{\partial v}{\partial x}\ ) \\ \frac{1}{2}\ (\frac{\partial u}{\partial y} + \frac{\partial v}{\partial x}\ ) & \frac{\partial v}{\partial y} \end{bmatrix}\ , \tag{5.3}$$

where u and v are displacements in the x and y directions respectively.

The strains obtained in MAX phases up until the point of macroscopic crack formation (greater than the optical resolution limit) is presented in the subsequent sub-section. Once macroscopic cracks form, the speckle pattern gets distorted, thereby leading to decorrelations. The DIC analysis is terminated before that point is reached. Therefore, strain smearing occurs over the following mechanisms: slip traces, kink bands, delaminations, transgranular cracking, grain pull-outs, etc.

Under a static loading condition, the values of strains obtained are on the order of ~1%. Now, based on the speckle sizes and resolution limit of the camera-lens, the window (or facet) over which strain calculations are resolvable is ~400μm (see Appendix B). Therefore, the effect of abovementioned mechanisms are *implicitly* embedded in the average values, point-wise analyses, and full-field maps, since the individual mechanisms occur at much lower length scales and only cumulative effects at the mesoscale can be captured, given the resolution limits of the current experimental set-up. To analyze the mechanisms explicitly, an experimental set-up at a lower length scale with advanced optical systems is necessary, which is the subject of future work. To this end, the methodologies identified by Valle et al.[105] i.e. subset splitting method, point-wise method, etc., to deal with discontinuities arising in the FOV (due to nanolayer separations for example) could prove to be an effective tool.

In DIC, there are two broad categories of errors: a) systematic errors and b) random errors. Systematic errors in DIC are related to the errors induced by shape function order, intensity interpolations, lens distortions, etc., which require special techniques for correction[89, 106]. To account for the error induced by interpolation, strain was calculated using two different interpolation methods (linear and spline) available in ARAMIS® [107] to analyze the error induced by linear interpolation. An error of 3.7 % between the strains calculated using the two methods was observed and there were no noticeable differences in the strain field maps (not shown here). Random or non-systematic errors can lead to false correlations, or even loss of correlations[87]. One way to avoid these errors is to apply a high contrast speckle pattern to the surface, the quality of which was assessed by studying the pixel intensity distribution histogram (see Fig. 2.3(b)).

For the majority of experimental data reported herein, 2D DIC was used to calculate strains in cylindrical specimens. This approach was validated by comparing 2D DIC results with 3D DIC. Validation tests on three cylindrical Ti_3SiC_2 samples (7 mm (dia.) x 13 mm (length)) were performed using two cameras under quasi-static loading conditions. Figure 5.1 shows a comparison between strains obtained using 2D and 3D DIC. The figure plots the average strain versus time response and strain fields at a given time instant during the test. It is observed that both the average strain calculations as well as the strain fields from the two methods have excellent agreement (average error < 5%) up to 1.5% strain. It is therefore inferred from these observations, that the curvature effects are minimal and therefore 2D DIC is employed. Based on this, the surface can also be considered nominally planar. Therefore, in the absence of significant barreling and asymmetry in out of plane motion, the planar assumption converges on the actual deformation and is a good approximation. The characteristic features of the strain fields in the two materials are presented in the remainder of this chapter. Note that strain heterogeneities are a consistent feature of all samples tested over a range of strain-rates.

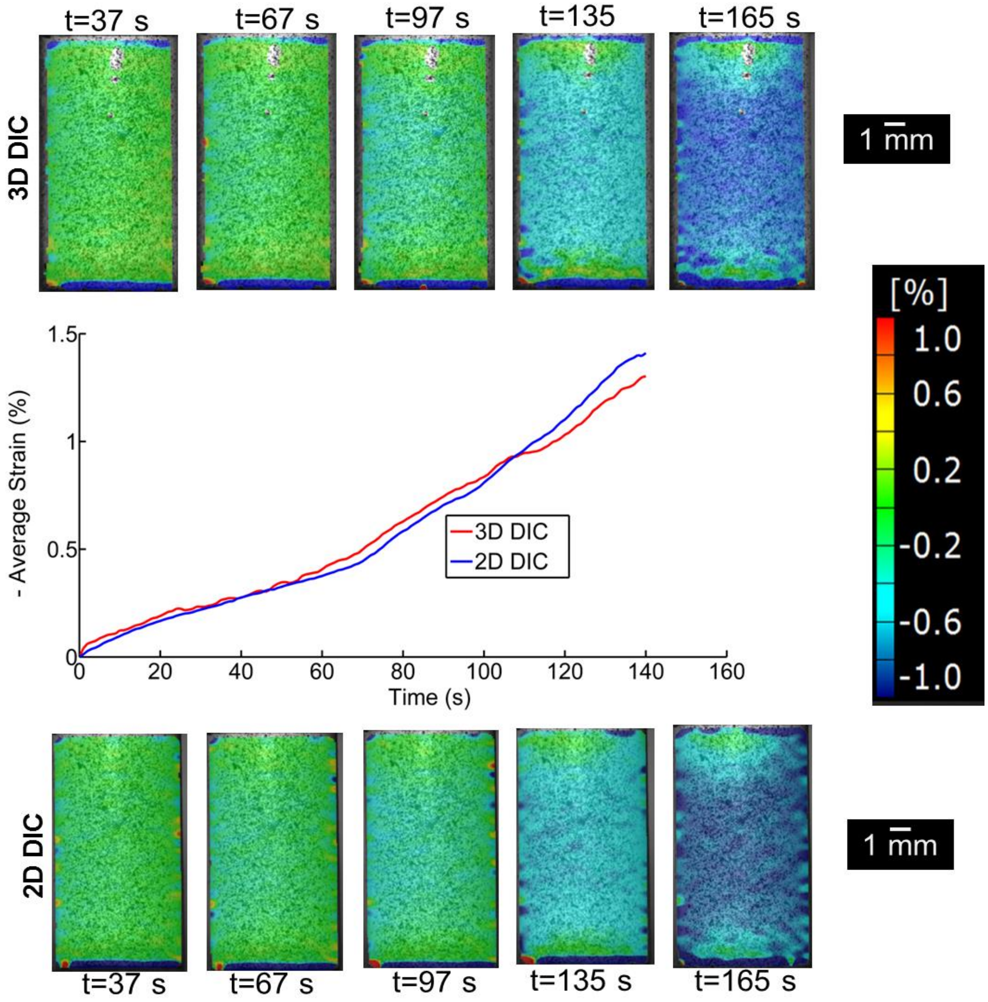

Figure 5.1 Characteristic plot of average strain versus time response for Ti_3SiC_2. The strain fields at different instants during the test, are captured using 2D and 3D DIC, which surround the plot.

5.3 Strain field characterizations

Strain fields for Ti_2AlC and Ti_3SiC_2 in the quasi-static range (10^{-3} – 10^{-5} s^{-1}) are presented in this sub-section. Figure 5.2 shows typical stress and strain versus time responses for Ti_2AlC loaded at a strain rate of 2 x 10^{-3} s^{-1}. The response has an initially flat regime after which the strain increases non-linearly. The end point of the curve indicates the last frame without visible cracks. After this point, cracks propagate unsteadily leading to near catastrophic failure of the specimen, which is indicated by an arrow pointing downwards on the stress versus time curve. The full-field images ((a)-(g)) shown in this figure depict the axial strain fields i.e. along the compressive loading direction. It is observed that up to a certain stress level (~200 MPa, as indicated by (d)), strains remain nearly homogenous. At this point and beyond, the field becomes increasingly inhomogeneous until the specimen fails. Overall, the stress versus time response has a near linear character without any significant visible transitions. Figure 5.3 shows the average strain / stress versus time in Ti_3SiC_2 loaded at a strain rate of 1.2×10^{-4} s^{-1}. The strain, in this case, initially rises sharply followed by an almost linear regime until ~ 350 MPa (point c) where a change in slope is observed leading into a non-linear regime. The non-linear portion has a hardening stage until the point of crack formation. The most interesting highlight from analyzing the average stress and strain curves is that in both Ti_2AlC and Ti_3SiC_2, there is a transition stress that coincides with the initiation of strain heterogeneity in the material. It is expected that the observations presented here will be appicable for other MAX phases as well. Furthermore, as will be discussed later, this transition point is most certainly controlled by processing induced microstructural features.

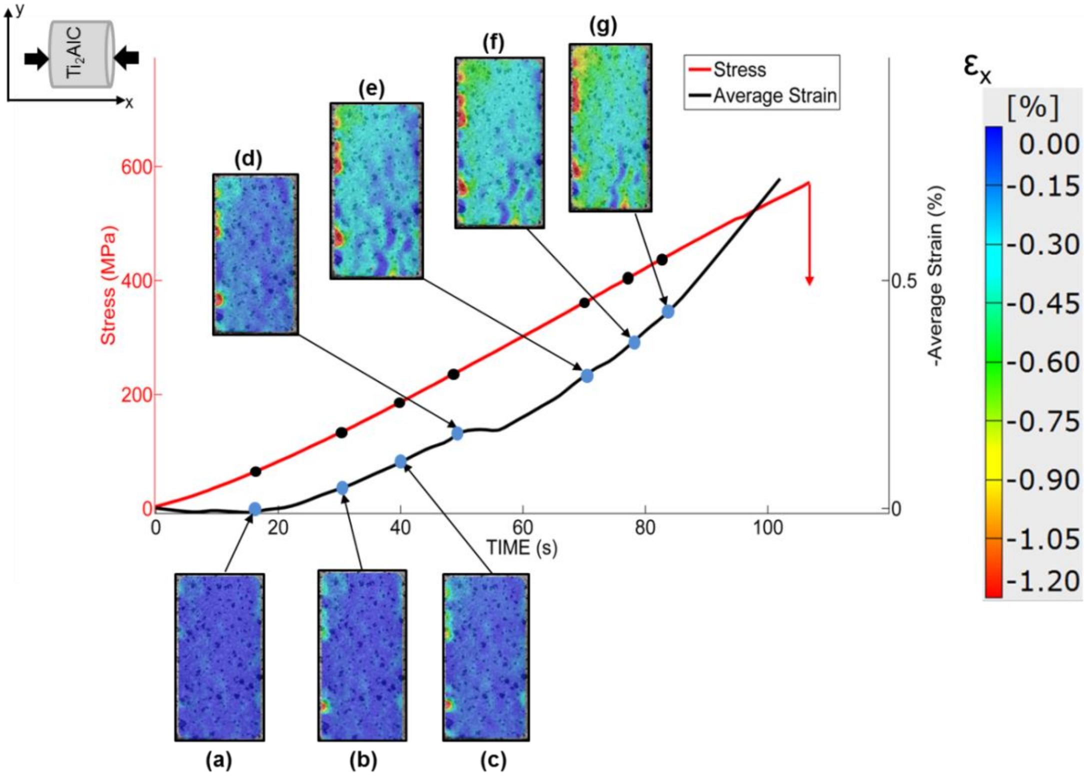

Figure 5.2 Characteristic average stress & axial strain versus time response, and strain field evolution ((a)-(g)) in the axial direction for Ti_2AlC. The blue and black dots indicate the time instant at which the field images are taken on the average strain / stress versus time response, respectively.

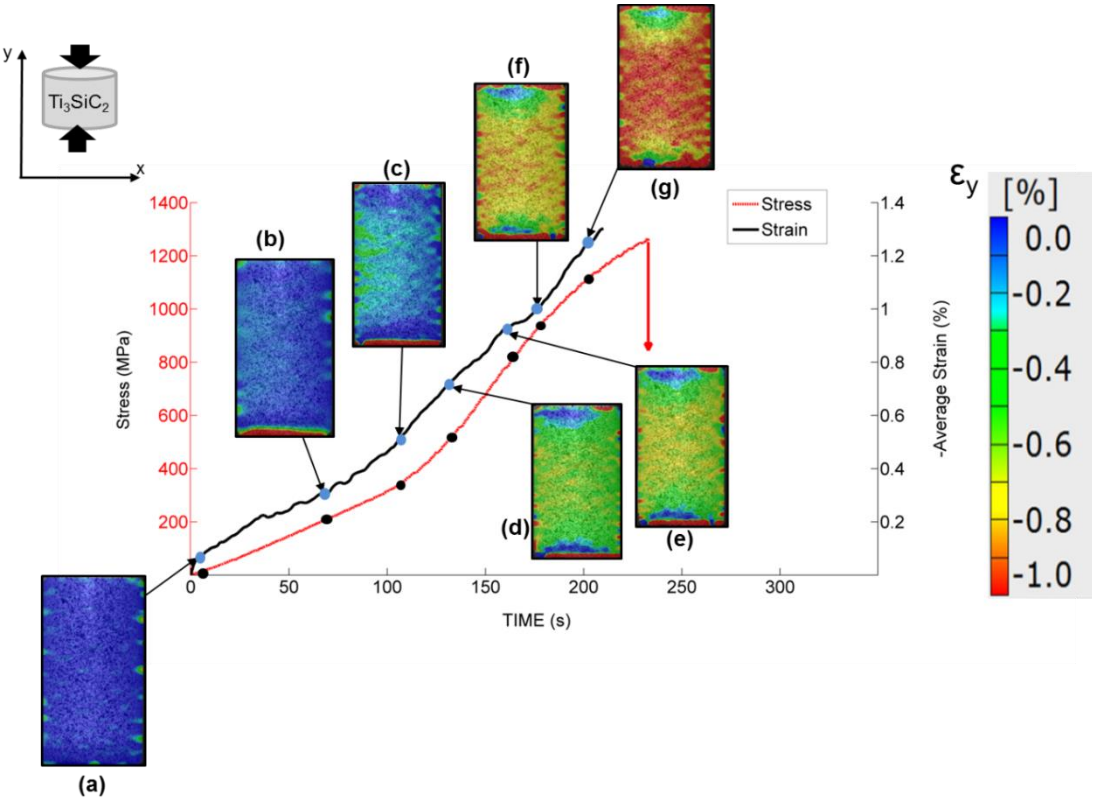

Figure 5.3 Characteristic stress/average axial strain versus time response, and strain field evolution in axial direction ((a)-(g)) for Ti_3SiC_2. The blue and black dots indicate the time instant at which the field images are taken taken on the average strain / stress versus time response, respectively.

The inherent inhomogeneities in the strain fields are analyzed by considering points along and transverse to the compression axis and analyzing the strain evolution of individual points. Figures 5.4(a)-(d) and 5.5(a)-(d) show the axial and transverse strain variations along and perpendicular to the axis of compression, in Ti_2AlC and Ti_3SiC_2, respectively. Overall, for most of the points in both materials, the strain has two regimes: i) a collated shallow regime and ii) a splayed steep regime. The transition from an initially slow rate of strain accumulation (indicated by a near flat regime) followed by a marked increase indicates a sudden change in the global dominant deformation mechanism. This occurs at a critical stress and is consistent across the sample. This change in slope is also approximately coincident with the splay or divergence of the different point strains. In other words, the critical stress signals a transition from relatively homogeneous strain in the sample to heterogeneous strain. The initial linear region is associated with coordinated elastic deformation mechanisms; subsequent heterogeneous strains are caused by multiple simultaneous deformation modes active within the material i.e. delamination, kinking, grain slip etc. The variations in point-wise strain accumulation slopes suggest localized mechanisms as opposed to a coordinated global progression. The rates at which average strain accumulate in the two materials are similar (pointing to similar mechanisms) but the initial near flat regime is smaller for Ti_2AlC. In Ti_3SiC_2, the axial strain rises more sharply compared to Ti_2AlC but for the transverse strain field, Ti_2AlC has a sharper rise.

The degree of inhomogeneity is quantified by a ratio D_i, which takes into account the difference between the maximum and minimum values at a point (over the entire loading cycle), normalized by the average global strain:

$$D_i = \left| \frac{\epsilon_{max}^{pt} - \epsilon_{min}^{pt}}{\epsilon_{avg}} \right| , \tag{5.4}$$

where the superscript *pt, min, max,* and *avg* indicates point strain, maximum, minimum and average strains, respectively. A summary of the average degree of heterogeneity for the two MAX phases under static loading conditions is presented in Table 5.1. If the strain field is homogeneous in its entirety, D_i would go to 0. A higher value of D_i is indicative of greater splay in the field along that direction. Overall, it is observed that the scatter is higher for points taken along the loading axis (thereby indicating higher degree of strain localization) as compared to the transverse direction.

The effect of strain-rate on the heterogeneities was also studied. This portion of the analysis builds on previous work on Ti_2AlC (Chapter 3), where optimal specimen sizes required to attain dynamic equilibrium conditions for Split Hopkinson Pressure Bar (SHPB) testing were established. It was verified that the samples reached dynamic equilibrium using front and back end stresses, obtained from the wave pulses. Furthermore, the signals had minimal or no wave dispersion effects (such as oscillations), demonstrating that one dimensional wave propagation was maintained during the experiments. Figure 5.6 shows a typical strain field distribution observed in Ti_2AlC from loading under higher high strain-rates. It is evident from the full field images and broadened strain histogram that the strain fields are also heterogeneous under high strain-rates. The magnified version further highlights the length scale at which the heterogeneous regions occur on the sample. The dynamic average strain versus time response is similar in nature to the quasi-static response detailed in this chapter i.e. there is an initial near flat regime followed by a non-linear rise. The most interesting highlight from the analysis is that the critical stresses beyond which heterogeneities are observed lie in the range 200-300 MPa for Ti_2AlC, and 320-400 MPa for Ti_3SiC_2 – this is consistent with the transition stress values under quasi-static loading conditions and hence points towards deformation mechanisms that are independent of strain-rate. The analysis presented in this section leads to the conclusion that the strains in MAX phases are heterogeneous. Possible origins for the heterogeneous character of strain fields are discussed in the subsequent section to provide further insight.

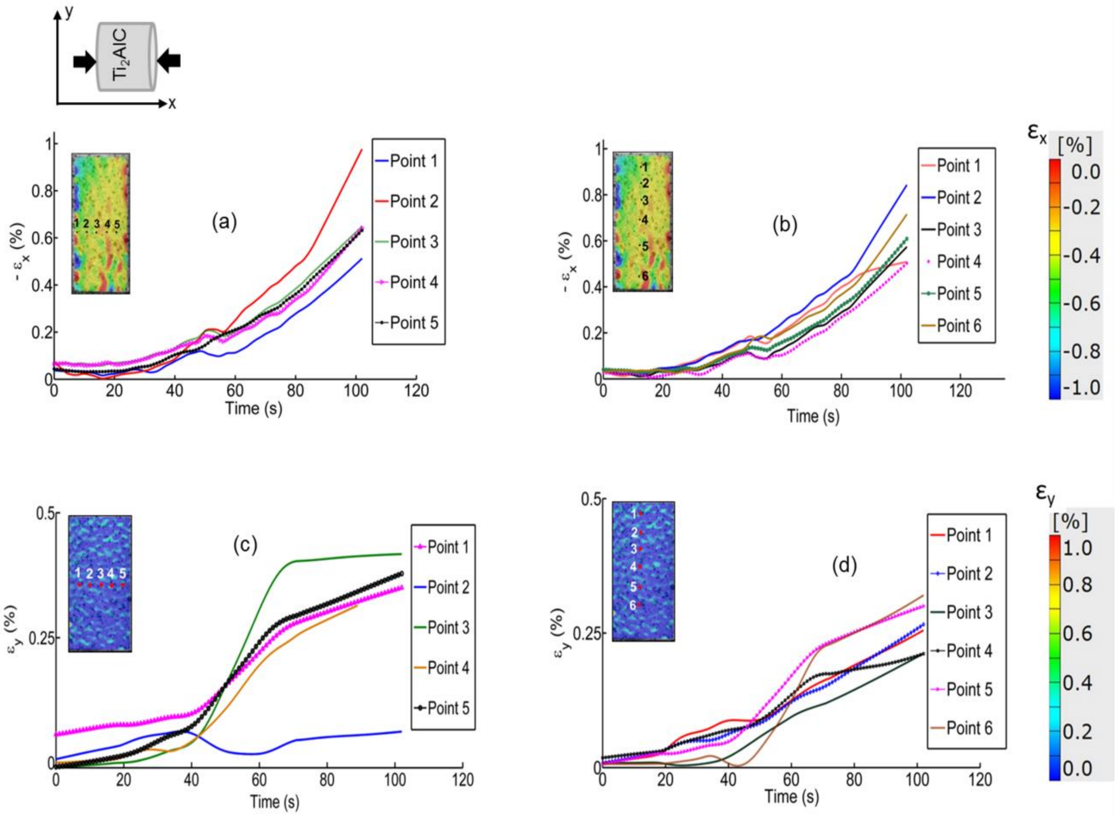

Figure 5.4 Representative point-wise axial(a)-(b), and transverse(c)-(d) strain evolution in Ti_2AlC for points taken along and perpendicular to the direction of applied compressive load.

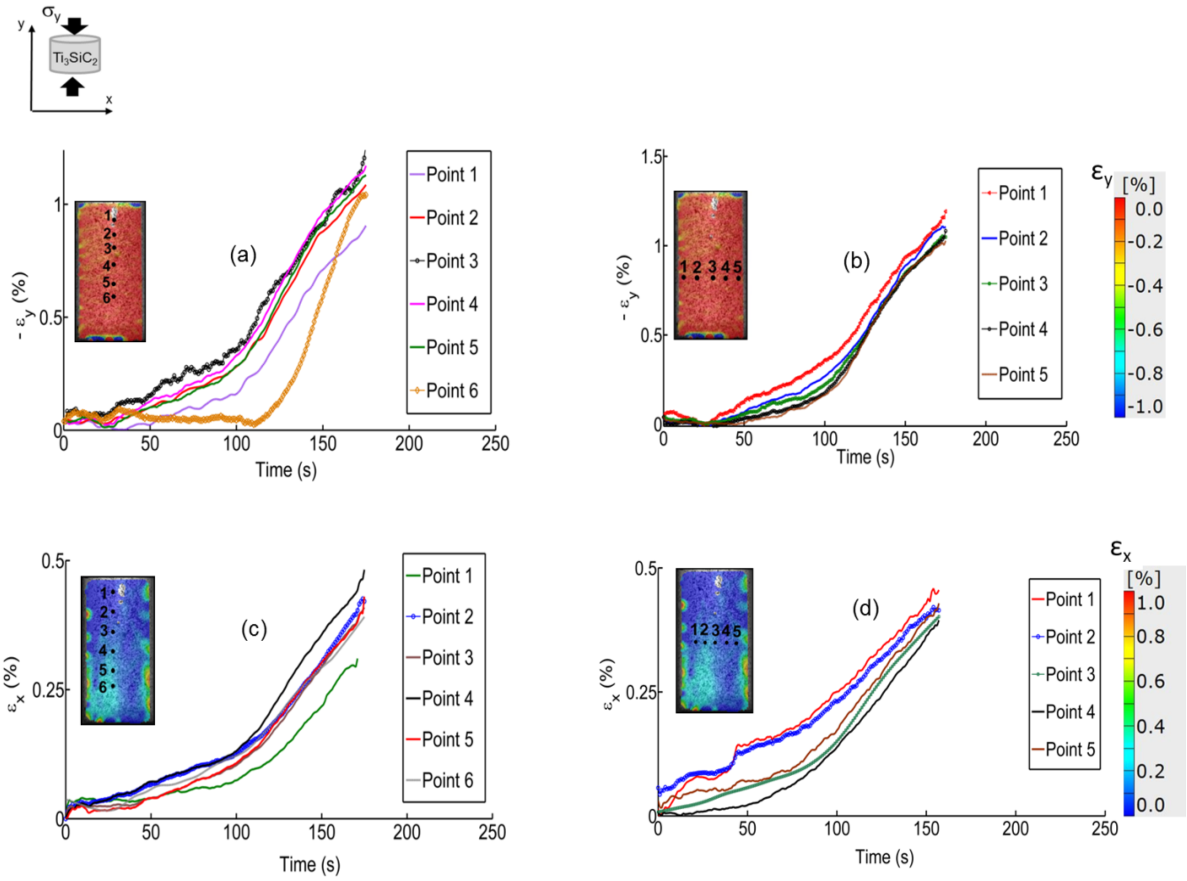

Figure 5.5 Representative point-wise (a)-(b) axial, and (c)-(d) transverse strain evolution in Ti_3SiC_2 for points taken along and perpendicular to the direction of applied compressive load.

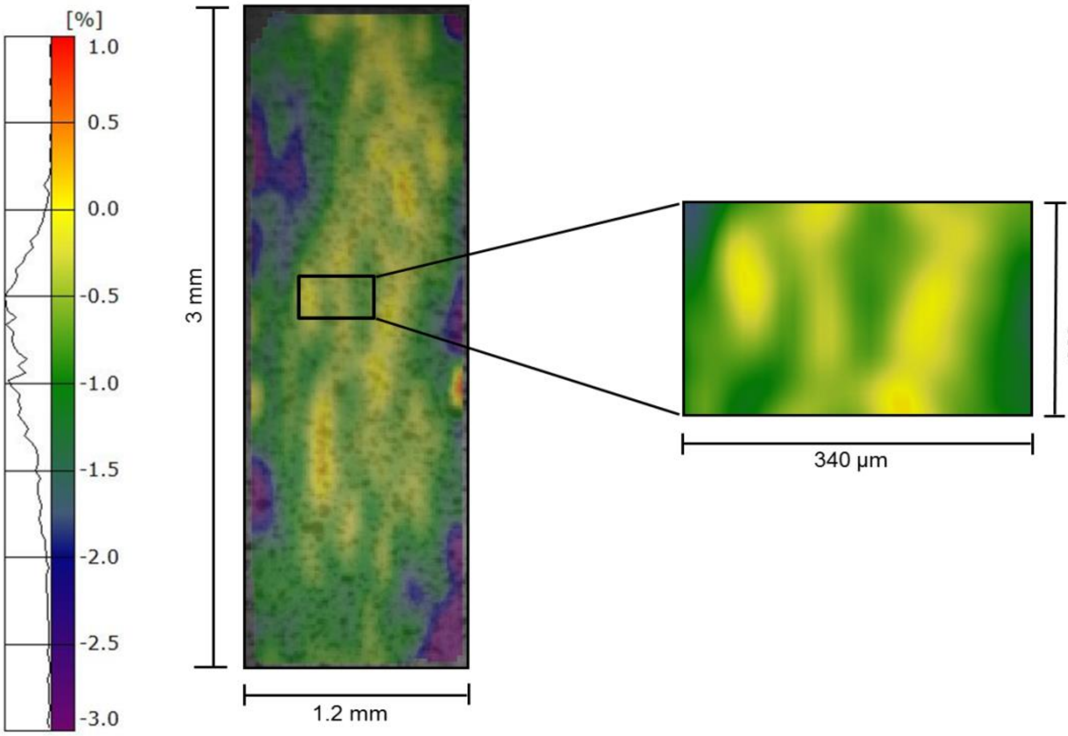

Figure 5.6 Strain field heterogeneity distribution in Ti_2AlC due to loading at strain-rate of ~3000 s^{-1}. The magnified version is shown to highlight the length scale of heterogeneous regions.

Table 5.1: Quantification of the parameter Di for the two representative MAX phases for point strains in axial and transverse directions.

Material	Strain field direction	Points taken for D_i calculation	D_i
Ti_2AlC	Axial	Axial	0.7
		Transverse	0.5
	Transverse	Axial	1.2
		Transverse	0.4
Ti_3SiC_2	Axial	Axial	0.6
		Transverse	0.2
	Transverse	Axial	0.8
		Transverse	0.4

5.4 Multi-scale mechanisms and heterogeneous strain origins in MAX phases

In this section, a multi-scale deformation map to account for heterogeneous strains in MAX phases is constructed. It has been shown that the response is heterogeneous and reported salient characteristics of how strain accumulates or is distributed in the material with increasing load. The heterogeneities develop after the material deforms past the low strain regime, where the deformation is near elastic. Beyond this regime, the response of polycrystalline MAX phases is pseudo-ductile since deformation proceeds via unconventional deformation modes. A low symmetry crystal structure (hcp) and lack of five independent slip systems means limited slip in a polycrystalline material [1-3]. The high mobility of dislocations leads to specific structural arrangements, thereby resulting in changes in the microstructure. The nano-layered grain structure is notably susceptible to the formation of kink bands. Kink bands have well defined boundaries known as kink boundaries, resulting from the specific arrangement of dislocations, which has been confirmed by Transmission Electron Microscopy (TEM) studies reported in the literature [2, 12]. These boundaries and fully formed kink bands, accompanied by interlayer delamination and void formations, can be observed on the fractured surface by SEM (see Fig 5.7). Indeed, a typical fracture surface studied by SEM will reveal the existence of not only ductile but also brittle modes at the nano- and micro- scales including grain pull-out, transgranular cracking, and cleavage[2, 97]. Figure 5.7 shows some of the typical modes observed by SEM fractography. The objective is to provide a link between the mechanisms at the nano- and micro-scales to the in situ strain data that was collected at the macro / meso scale to provide insight on the origins of observed heterogeneous strains.

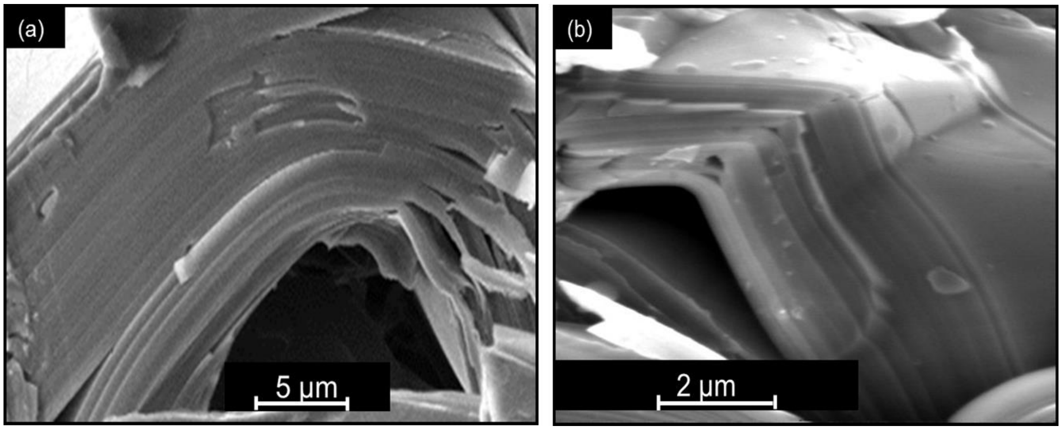

Figure 5.7 Post-fracture micrographs, showing a) buckling, delamination and b) kinking of nano-layers in Ti_2AlC.

Now, to study the strain fields in more detail, analyses of enlarged FOVs are performed. The contribution of DIC input parameters (subset, step and computation size) to strain smearing or averaging is elucidated in Appendix B. The subset (or facet) size is an indicator of the spatial resolution to which strains can be measured. Based on the optics used in the experiments and software technique in calculating strain, the strain at a ‘point’ is smeared strain that represents a calculation over a fixed number of grains, as mentioned earlier. The average number of grains per subset (See Table 2.2) is ~20. This range is calculated by assuming an average grain size ~15-18 μm, based on microstructural characterizations.

A portion of the microstructure obtained from SEM is shown in Figure 5.8 (a). It is observed that: i) the grains have a random orientation, ii) there is a size distribution of grains (~10-100 microns), and iii) second phase particles (shown by black circles). At slightly higher magnifications (not shown here), some microflaws or pore like features are observed due to incomplete densification. It is expected that with progressing deformation, these flaws grow thereby facilitating buckling and subsequent kink band formations of the nano-laminates adjacent to them. For kinking to proceed, the grains have to be oriented favorably with respect to the loading direction. Figure 5.8(b) shows a typical strain field distribution in Ti_2AlC under quasi-static loading.

The central portion of the strain field is magnified for further analysis, which spans a cluster of grains on the sample surface. This *mesoscopic* element reveals an emergent pattern in the strain field, order of which corresponds to the length scale of microstructural features (shown in Fig 5.8(a)). There are regions of low strain surrounded by regions of high strain on the order of a few hundred microns. The patterned character of strain in the mesoscopic element indicates that grain clusters (based on the size), as well as grain-grain interactions play a central role in the deformation of MAX phases. Grains which are favorably oriented for deformation to progress via basal slip and kink band formations will strain more in comparison to its neighbors. On the other hand, unfavorably oriented grains strain less and facilitate deformation via quasi-brittle modes. Therefore, the results presented here indicate that a mesoscopic combination of favorably and unfavorably oriented grain clusters lead to heterogeneous strain fields. Guitton et al.[59] investigated the strain field evolution in polycrystalline Ti_2AlN, another representative MAX phase, using in situ neutron diffraction and observed that all families of grains show heterogeneous strains. This pointed towards mechanisms other than orientations i.e. role of neighboring grains in a polycrystal that lead to a multi-axial state of stress in a grain. The observation presented in their work was further validated by Shamma[66], and Benitez et al.[40] for Ti_2AlC. Orientation of a particular grain, however, does dictate whether the grain will deform by conventional slip (Schmid factor) but the pseudo-ductile modes of deformation i.e. kink bands and associated delamination, is due to a combination of orientation and neighborhood effects. The deformation patterns presented here are however at a higher length scale i.e. the mesoscale. The most important result of this analysis is the clustering of grains in MAX phases that are identified as discrete homogeneous patterns on the strain fields (see Figs. 5.10-5.12). Said otherwise, a grain cluster can be defined as a region of several grains over which a strain is smeared. The optics of the current set-up and software (ARAMIS) parameters chosen show strain smeared over a region of ~400 μm (see Appendix B), wherein the heterogeneous patterns observed are due to a smeared or combined effect of grain scale mechanisms[84]. The high strain regions can be therefore be mapped to softer grains in a soft neighborhood – that is to say, the neighbors that accommodate deformation while maintaining the overall integrity by deforming without fracturing. Similarly, low strain regions can be thought to represent a relatively harder neighborhood that tend to deform by elastic modes and eventually fracture.

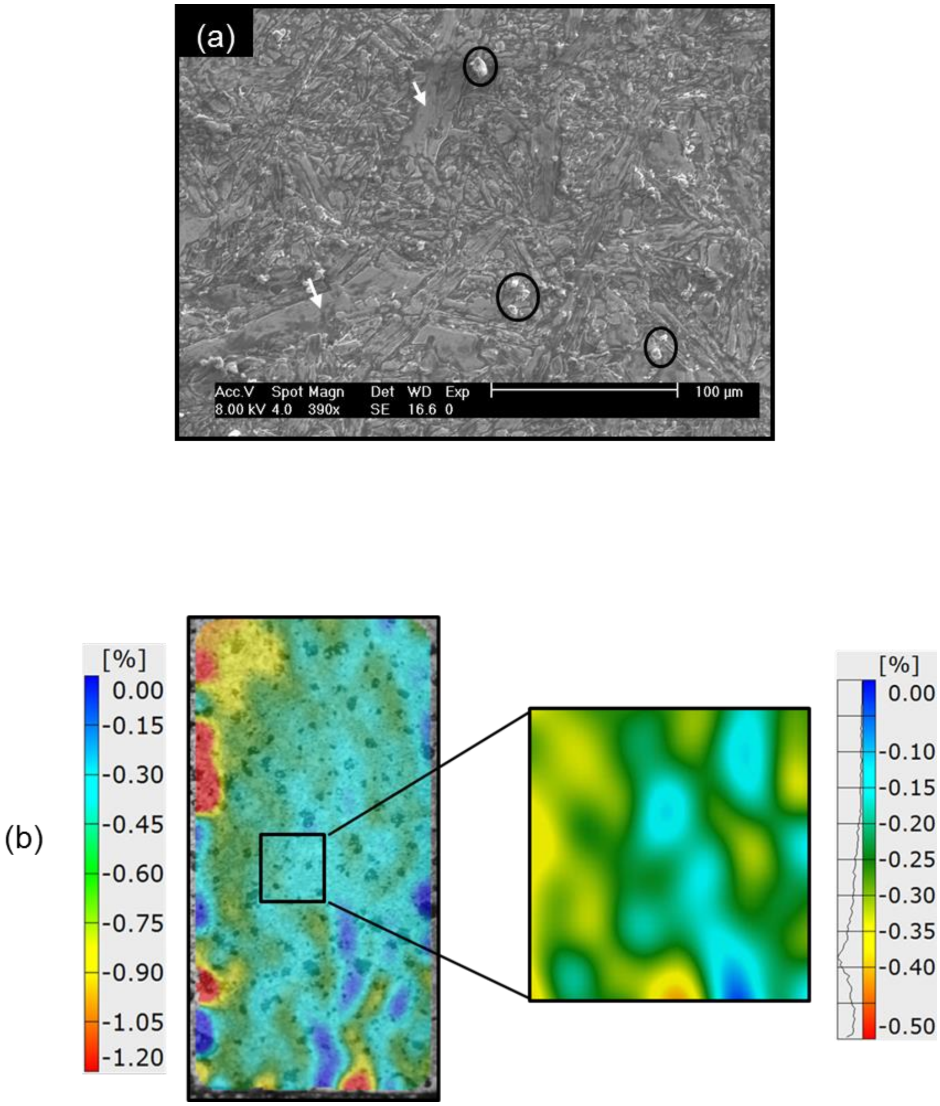

Figure 5.8 a) As processed microstructure showing the random grain orientations, size distribution, and secondary phases, and b) strain field distributions for a Ti_2AlC specimen under quasi-static loading conditions.

Figure 5.9 shows the full FOV of a Ti_2AlC sample tested under static loading conditions, segmented into approximate squares of side lengths ~ 2 mm. The central regions are analyzed further by magnifying them and the circles indicate reference speckles used to track them at different time stamps (i.e. levels of average global strain) during the test. The magnified versions of the strain fields from the regions marked 1,2 and 3 are shown in Figures 5.10(a)-(i), 5.11(a)-(i), and 5.12(a)-(i) respectively where an emergent pattern is clearly revealed. It is observed that regardless of the level of strain, there are regions of high strain (shown by rectangles) surrounded by regions of low strain (shown by ellipses). It must be noted that for regions where neighboring low strain regions are obvious from the legend, ellipses are not included to avoid cluttering the images and thereby facilitating clearer view of the emergent patterns. These patterned regions of low and high strain are on the order of a few hundred microns (or tenths of millimeters), which would represent a cluster of ~20 grains or fewer larger grains based on the optical resolution limits. The units change in form and size, and there appears to be some rotation with increasing strain. This can be possibly attributed to the grains deforming plastically to accommodate the deformation and maintain integrity at the grain boundaries. A signature of this is manifested on the fracture surface in the form of kink bands, nano-laminate buckling and even slip traces. Furthermore, the pseudo-ductile (or inelastic) mechanisms such as delaminations lead to a refinement of the microstructure and can also be likely sources of strain localization at the mesoscale. On the other hand, the regions of low strain are likely indicative of grains which deform (or distort) elastically, followed by a brittle failure mode, observed on post-fracture micrographs. Based on ex-situ SEM analysis, and reports in the literature on other representative MAX phases[59, 108, 109], qualitative microscopic origins of strain localizations and patterned strain field evolution is presented here.

The exact microstructural feature contributing to this and strain fields in general, is difficult to quantify with the current optical resolutions and will require strain field resolution at the sub-grain level, which is the subject of future work.

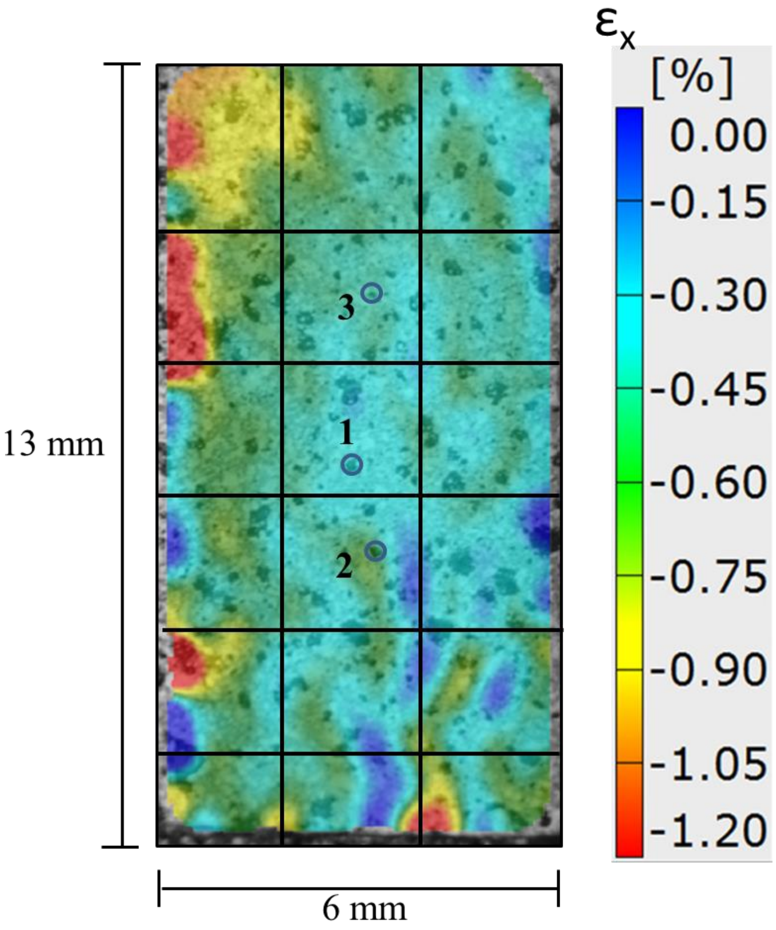

Figure 5.9 A Ti_2AlC specimen showing strain fields under static loading and the segmented FOV showing the size and reference points of the regions, where strain fields are analyzed by studying magnified versions.

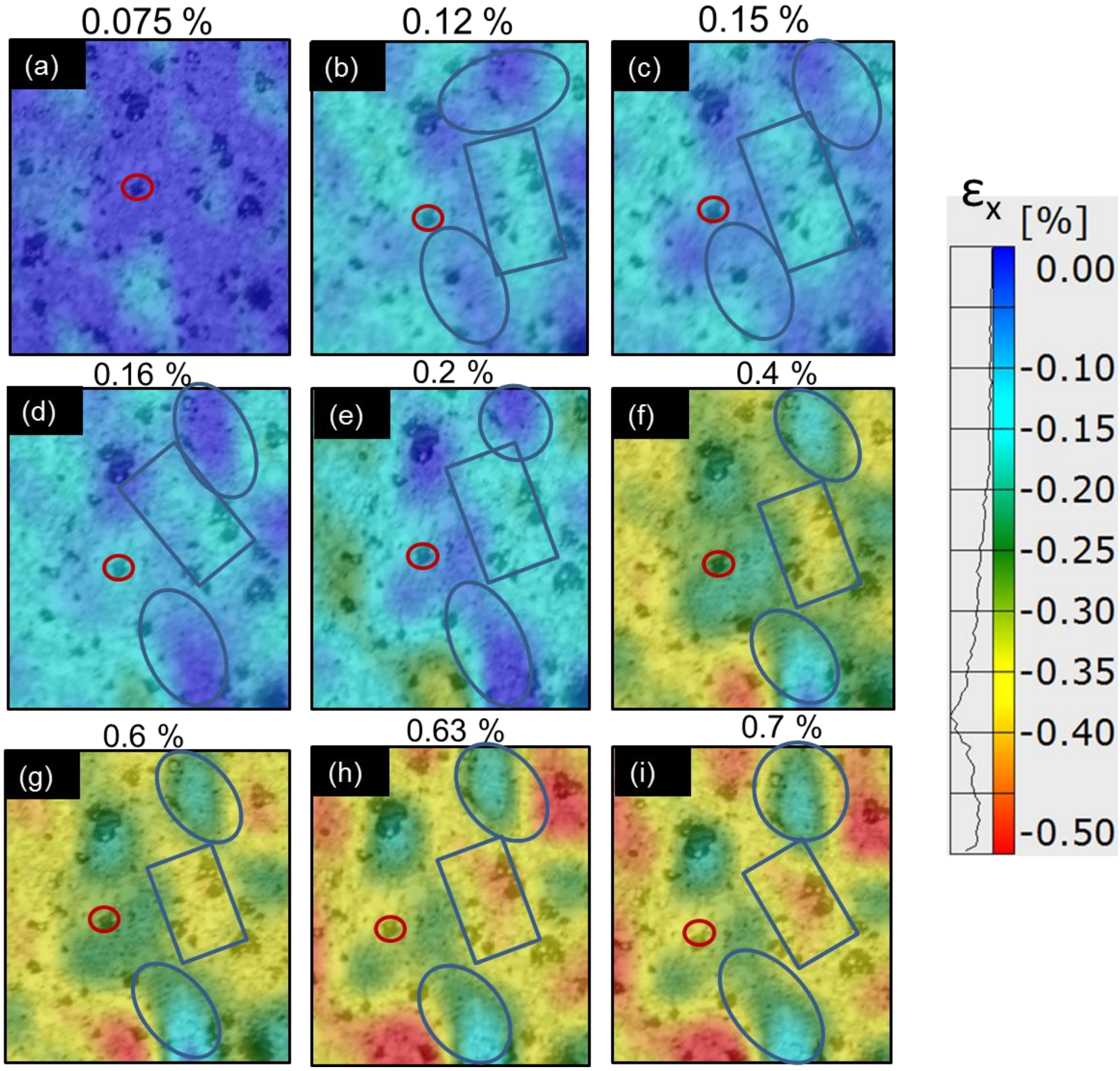

Figure 5.10 (a)-(i). Magnified views of the axial strain field taken from the central portion (Region 1) of a Ti_2AlC sample tested under static conditions, at different instants. The values at the top of each image indicate the average axial strain accumulated, and the boxes highlight two regions where higher strains (shown by rectangle) are bounded by lower strains (shown by ellipses). The red circles denote the reference points used for comparison.

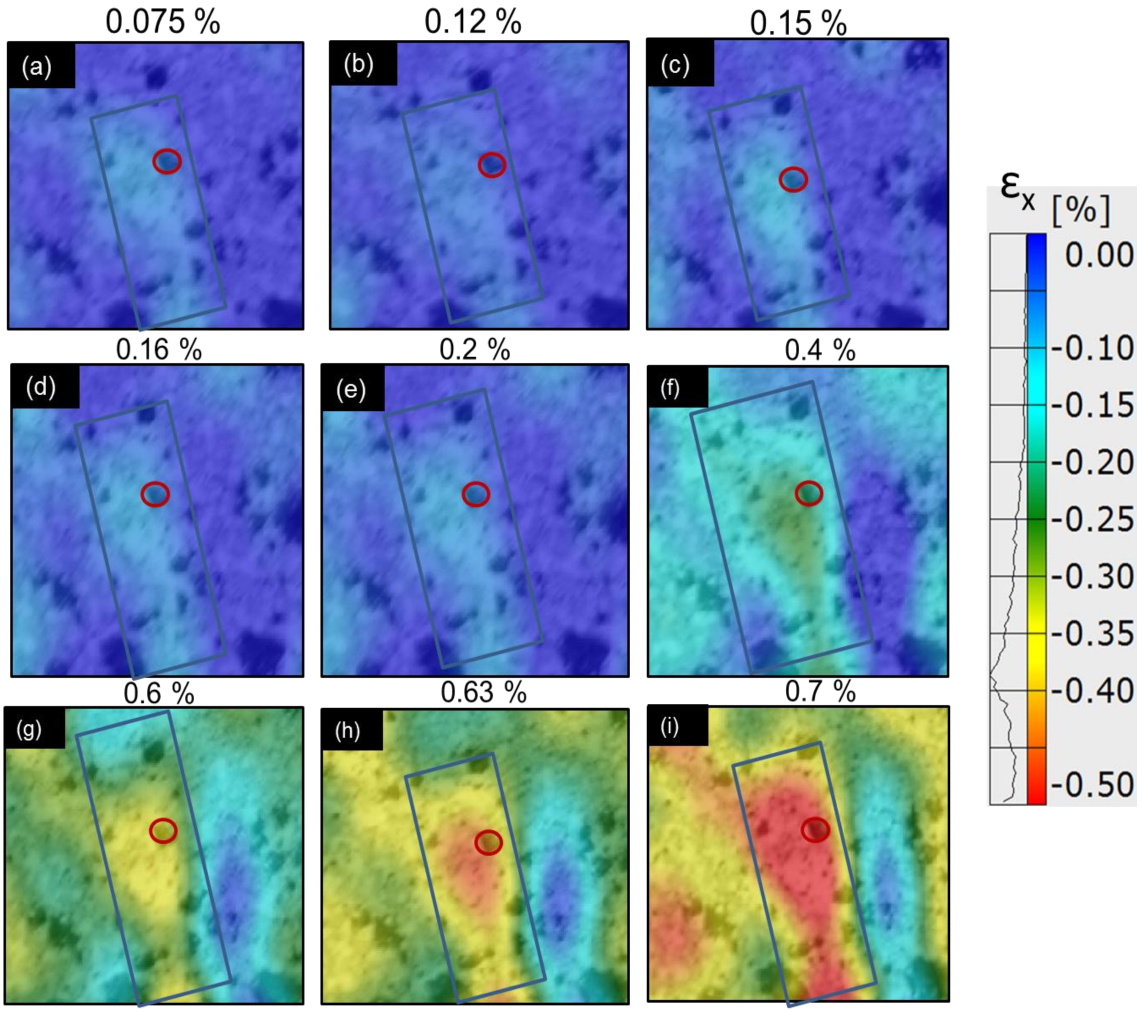

Figure 5.11 (a)-(i). Magnified views of the axial strain field taken from the central portion (Region 2) of a Ti_2AlC sample tested under static conditions, at different instants. The values at the top of each image indicate the average axial strain accumulated, and the boxes highlight two regions where higher strains (shown by rectangle) are bounded by lower strains (left unmarked). The red circles denote the reference points used for comparison.

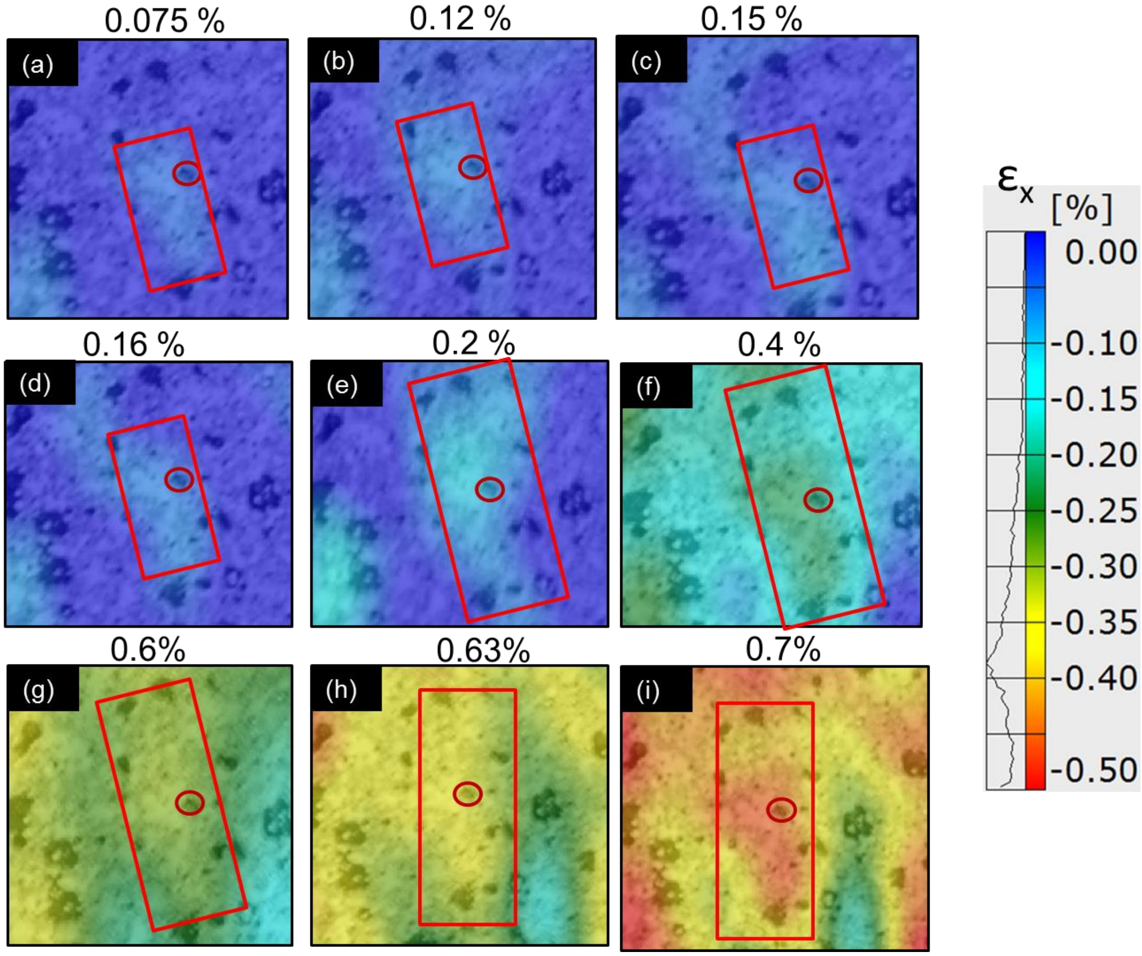

Figure 5.12 (a)-(i). Magnified views of Region 3 of a Ti_2AlC sample (shown in Fig.5.9) tested under static conditions, at different instants. The values at the top of each image indicate the average axial strain accumulated, and the boxes highlight two regions where higher strains (shown by rectangle) are bounded by lower strains (left unmarked). The red circles denote the reference points used for comparison.

5.5 Conclusions

In this chapter, the strain field evolution in representative MAX phases (Ti_2AlC and Ti_3SiC_2) was characterized and quantified under static and dynamic loading conditions for the first time. It is observed that the strain field is heterogeneous, which is due to a cumulative effect of mechanisms occurring at lower length scales. At the macro-scale, it is observed that the inhomogeneities in the strain field begin to appear when the stress level in the material reaches a critical stress. For Ti_2AlC, this value is found to lie between 200-300 MPa and for Ti_3SiC_2 this value is slightly higher and lies in the range 320-400 MPa, independent of the strain-rate. The strains are on the order of ~1% for both materials under quasi static loading conditions. Our experimental results show that the critical stress signals a transition from homogeneous to heterogeneous strain.

In depth analysis of the strain fields reveal an underlying meso-structure comprised of soft and hard grain clusters. In summary, a macroscale full field technique shows presence of grain clusters that play a central role in the deformation of Ti_2AlC and Ti_3SiC_2. Since slip is limited and twin formation is not possible in these materials, the relatively soft grains can deform by nano-layer buckling, kinking and delamination. On the other hand, the relatively hard grains deform elastically and then by quasi-brittle modes. At the macroscale, the simultaneous coexistence of these deformation modes give rise to soft and hard grain clusters that manifest as heterogeneities in the strain field. It will be important to assess the role of processing and fabrication on the emergent mesostructure..

Chapter 6: Deformation modes in an idealized multi-layered grain

6.1 Introduction

The previous chapter revealed the presence of an inherent mesoscale in the deformation response of representative polycrystalline MAX phases. Generally speaking, the results presented in this dissertation and reports in the current literature point towards three categories of deformation modes occurring in polycrystalline MAX phases , as i) linear elastic, ii) plastic or conventional ductile, and iii) pseudo-ductile modes. The mechanisms associated with these modes appear at four distinct length scales: the atomic scale, the nanoscale, the microscale, and the meso-scale. Bridging the scales in a cohesive and consistent theory remains an open research area. The origins of the pseudoductile modes are a central focus of current research efforts. In this chapter, one of the pseudo-ductile manifestations of deformation i.e. kinking (within a single grain) is captured using a 3D numerical model in an idealized representative grain, formulated in ABAQUS®. The model presented herein assumes a pre-existing layered sub-grain structure (i.e. nanolayer delamination is not explicitly treated), anisotropic elastic material properties, and neighboring grain effects that are of relevance in MAX phases. The simulations are categorized into two groups. In the first group, linear elastic buckling theory is used to illustrate how a critical load would lead to geometric restructuring of a grain (i.e. instability) based on structural mechanics considerations alone. The second group of simulations can be used as a visualization tool to show how grain-to-grain interactions could lead to bending as a result of multi-axial stresses transferred through neighboring grains to a local grain of interest.

6.2 Background and model objectives

6.2.1 Current state of the art and objectives

The evolution of local strain fields by in situ deformation in representative MAX phases demonstrates the heterogeneous nature of strain at the meso-macro scale (i.e. hundreds of grains assemblies of which are referred to as grain clusters in this thesis). MAX phases have been shown to consist of soft and hard grains at the microscale by in situ deformation under x-ray and via simulations[110]. Concurrent and more recent works in the literature have tried to explain the origins of reversible hysteresis by pointing to local 'heterogeneous' strain fields which are comprised of coexisting elastic and plastic deformations at the microscale (i.e. few grains) . Guitton et al. [59] studied the deformation behavior by in-situ compression in polycrystalline Ti_2AlN using in situ neutron diffraction. The samples used in their work were fabricated using the powder metallurgical route of HIP, resulting in two different microstructures – "small grain" structures with mean grain size of 17 μm and a bimodal microstructure with sizes of 20 and 88 μm, both of which exhibited granular anisotropy.

The initial elastic strain was found to be heterogeneous according to grain family orientation, which was presumed to be a result of grain to grain stress variations (polycrystal effect). It was found that beyond a critical stress level, different grain families strain differently. The grains parallel to the compression axis were observed to deform via elastic modes of deformation and plastic deformation occurred in grains perpendicular to the compression axis beyond the initial elastic regime. To account for recoverable hysteresis, it was theorized that elastic bending of grains would occur as a result of grain-to-grain interactions among larger grains. Plastic behavior was attributed to a combination of dislocation based microstresses (low density dislocation nucleation that can be recovered upon unloading) and multiaxial stresses from bending. It was suggested that the open loops in the macroscopic response point to a changing microstructure (elastically distorted grains) brought upon by complex multiaxial stress-strain path. Based on an analysis of the microstructural landscape before and after deformation it was theorized that neighboring grains create a multi-axial state of stress for a local grain.

Benitez et al[40] analyzed the microstructure of cyclically compressed high purity spark plasma sintered Ti_2AlC using an EBSD technique and observed the formation of Low Angle Grain Boundaries (LAGBs) in grains independent of their Schmidt factors (which is a measure of their orientation). This observation was considered as evidence of the theory that orientations alone do not govern the occurrence of kinking in MAX phases as previously believed. That is to say, the conjecture that favorably oriented grains deform by slip (45 degrees to loading direction) and unfavorably oriented grains (along loading direction) deform by kinking. It must be noted that the grain aspect ratios observed in this work were lower (almost close to a ratio of ~1:1) as opposed to the samples studied here or reported earlier[10, 17]that have a more elongated appearance. The proliferation of kinking in low aspect ratio grains irrespective of their orientation to the loading axis provided further evidence that kinking is a dislocation-based phenomenon and not just elastic or elasto-plastic buckling of the nanostructured grain. Their analysis and recent work by Shamma et al.[66] have reported that LAGBs form not only due to their orientation (relative to the loading direction) but also due to incompatibility stresses between grains, that is to say caused by neighboring grains and associated plastic anisotropy. The stress-strain hysteresis loops are attributed to grain refinement and misorientations. The development of substructures, due to kinking and delamination, and subgrains in soft grains, occur at the microscale. Of these substructures, reversible dislocation glide is ruled out as a major energy dissipation mechanism and it is theorized that reversible movement or 'bowing' of dislocations (boundaries) is the primary source. The LAKBs or LAKB loops are provided as evidence that recoverable and irrecoverable kink formations are the likely mechanism by which hysteresis loops are formed. This work provides a counter theory to Guitton's work which suggested that grain bending (macro-stresses) plays a major role in the hysteresis response as opposed to dislocation based kinking (micro-stresses). The third major theory of plastic deformation in MAX Phases concerns the opening/closing and propagation of microcracks, which is not explicitly considered here and which we rule out as a basis for closed hysteresis behavior. Although this mechanism is likely relevant for open hysteresis loops and a precursor for eventual fracture as acknowledged by both Guitton et al.[59] and Benitez et al.[40].

The objective of the study presented in this chapter is to visualize the relevant deformation modes observed in MAX phases i.e. visualize kinking and bending without pre-subscribing to a particular theory regarding its origin. The simulations are created by considering i) elastic buckling and ii) elastic bending in multilayered nanostructures representative of a MAX Phase grain in a polycrystalline solid. The results are of use to both theoretical groups though in different ways. The influence of geometric parameters and physical constraints is identified through a series of extensive computational simulations. This model underlies the theoretical grain-scale conditions hypothesized in both Guitton et al.[59] and Shamma et al.[66] and provides a visualization of the likely stress and strain fields under multiaxial loading that lead to gross bending and buckling in a grain. Reports by Shamma and Benitez et al.[40, 66] show evidence of Low Angle Kink Boundaries (LAKBs) and Low Angle Grain Boundaries (LAGBs) that appear on all grains irrespective of the Schmidt factors though more favorably in medium to high Schmid factor grains. Simulations were also carried out to represent the grain-scale conditions underlying the hypothesis presented by Benitez et al.[40]

For clarity, nomenclature consistent with Benitez et al.[40] is used to refer to soft/hard grains. Guitton et al.[59], on the other hand, referred to two grain families that are a) either near parallel or b) near perpendicular to the loading direction that either deform plastically or show a purely elastic behavior. In their nomenclature, they use the angle that a plane normal makes with the loading axis to define preferable orientations. In other words, their “low angle” grains are equivalent to transversal hard grains following Benitez et al.’s definition. Similarly, their “high angle” grains are equivalent to longitudinal hard grains. The definitions (soft / hard) by Benitez et al. have been used throughout this chapter to denote the orientations to externally *applied* load and the terms “soft” and “hard” should not be interpreted to be an indicator of the response.

6.2.2 A 2-D model for buckling of layered structures

The multi-layered nature of MAX phases at the sub-grain (or nanolaminate) length scale has been well established in the literature, detailed analysis of which has been presented in earlier chapters. This layered nature gives rise to Kink Bands (KB) when subjected to different loading conditions. Multi-scale experimental analyses in the literature have revealed that these features form due to presence of mobile dislocations at lower length scales, which eventually coalesce in a narrow region forming Dislocation Walls (DWs)[10], which appear as kink boundaries at the nano-laminate length scale. Typical kinking ~~f~~eatures observed in SEM micrographs of Ti_2AlC post high strain-rate loading have been presented earlier in the dissertation (see Figs 1.5(a)-(d)). It is observed that the features are strikingly similar in appearance to different types of fold formations observed in geological materials that are naturally multi-layered[50]. In the last decade, the mechanics of different types of fold formations in geological materials have been studied by Wadee et al[111-113], wherein a test configuration using a stack of papers have been used to mimic the multi-layered nature observed in geological rocks. The boundary conditions in their work were tailored by using different surrounding materials to obtain different fold configurations in the stack of papers. Dodwell et al[114] recently reported on void formations along with the folding typically observed in these materials. In their work, an analytical formulation is developed wherein a stack of Euler-Bernoulli (EB) beams are used to model folding along with void formations under uniaxial compression, using a constrained minimization approach. The results show how geometry and relative loading conditions influence the characteristics of the folded structures. In the context of MAX phases, geometry, orientation, loading conditions, and boundary conditions of as processed grains all contribute to the observed kinking deformation (Figs.1.5 and 1.6).

A parametric analysis of the 2D Dodwell model, incorporating varying aspect ratios and boundary conditions that are of importance to MAX phases, is first presented in the subsequent section. The model captures periodic voiding in a multi-layered stack by extending their single layer model, which is consistent with voids observed near kink formations in SEM micrographs (see Eqn 2.2 in [114]). The model however does not account for inter-laminar interactions (neither through friction nor cohesion), which would be of interest in future work, and is inherently 2D. The kink bands observed in MAX phases post fracture are associated with inter-layer splitting (nanolayer delaminations). In order to probe the mechanics of the deformation behavior for a host of complex loading and boundary conditions whilst varying the geometry in 3D, a computational platform is employed to generate a large number of simulations in a short amount of time and at low computational cost. The simulations facilitate the visualization of stress and strain fields of a layered beam structure. The inherent layered geometry, material anisotropy (arising from hexagonal crystal structure), and the multi-axial loading conditions due to neighboring grains, relevant for MAX phases, are easily implementable in a computational environment like ABAQUS® (see section 6.4). The layers present in the model had identical material and geometric properties, representative of a MAX phase grain.

From an experimental perspective, processing of multi-layered single crystal MAX phases is not possible due to thermodynamic instability of nano-layers and layer-by-layer deposition methods to obtain bulk single crystals are cost prohibitive. In the absence of single crystal testing, we would suggest that the development of an *in situ* multi-scale experiment to simultaneously capture the microstructural and grain-level landscape would be worth pursuing. Given the current state of the art, it is therefore valuable and insightful to analyze the deformation mechanics of a single grain using numerical and computational tools to supplement single-length scale experimental studies being carried out. Here, the evolution of deformation features is studied using a numerical model that simulates the MAX phase polycrystal i.e. a single grain within a body of surrounding grains that provide nonuniform boundary and load-transfer conditions. First, the 2D model for bending of a multilayered stack is employed, parameterized and analyzed for a representative MAX phase in Section 6.3. This is followed by 3-D computational model simulations (performed in ABAQUS) presented in section 6.4, which accounts for material, geometric and neighboring grain effects encountered by a MAX phase grain.

6.3 Dodwell model and MAX phases

The model formulated by Dodwell et al. [114] is parameterized by incorporating relevant geometrical properties for nanolayers within a representative MAX phase grain. Figure 6.1 shows a schematic of the Dodwell model formulation set-up that has been modified parametrically to represent MAX phases. In the Dodwell model, an infinite beam element is considered which folds into a V-shaped region bounded by rigid elements, as shown in Figure 6.1(a). The fundamental formulation proposed by Dodwell et al. is used and the boundary conditions are tailored to allow for finite rotations at the two ends (i.e. a simply supported beam versus the infinitely long layer employed in [114]), thereby representing a layer bounded by grains that permit rotation. A typical response for a single representative layer is shown in Fig. 6.1(b). This single layer representation is then extended to multiple layers by introducing a geometric parameter that accounts for inter-layer voiding (see equation 3.1 in [114]), as shown in Fig.6.1(c). The formulation is able to effectively capture the chevron type folding observed in MAX phases along with inter-layer voiding that are strikingly similar to post-fracture micrographs. However, the analytical formulation cannot readily capture the key effects of multi-axial loading, which motivates the development of a computational model. The simulations allow an efficient calculation of different 3D geometries, material anisotropy, and with relatively low computational expense can be easily extended to capture dynamic effects, finite deformations, and material nonlinearities that may be of future interest. Furthermore, it can facilitate visualization of stress and strain fields in three dimensions. This aspect could also prove to be useful in making comparisons with multiscale experimental characterizations of MAX phases, as they continue to evolve.

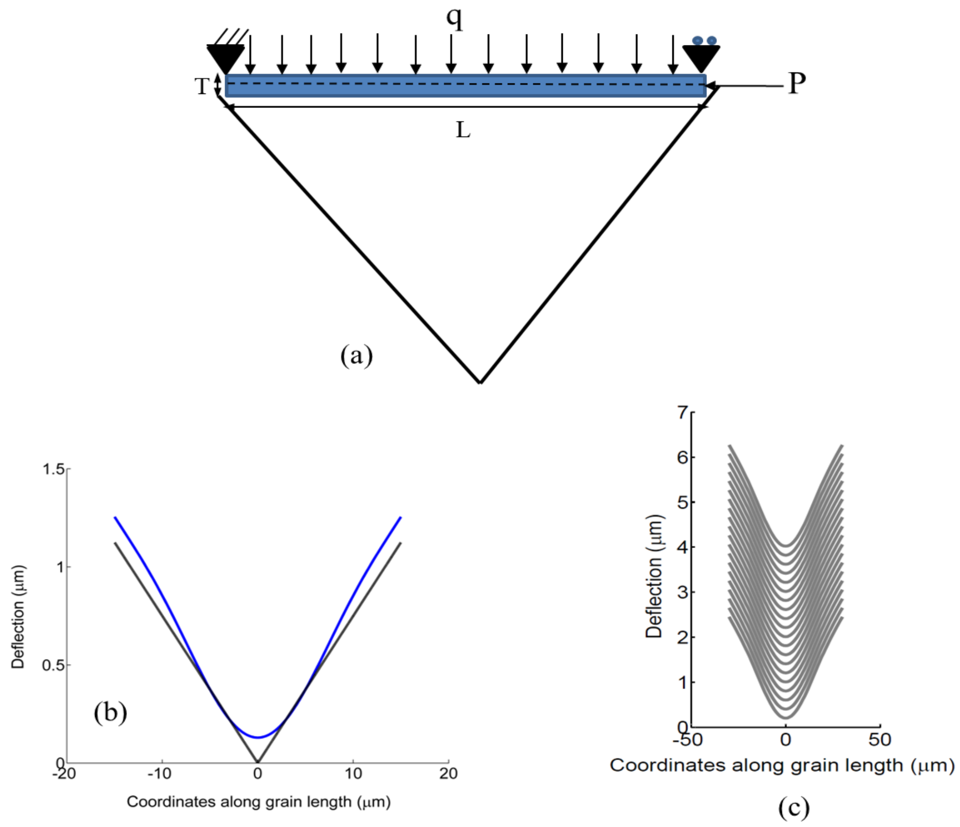

Figure 6.1 (a) Representative layer model set-up in Dodwell et al [ ] that has been adopted to qualitatively represent the folding observed in MAX phases, (b) a typical response of a layer bending into an obstacle thereby creating a void, and c) extension of this response to multiple layers.

6.4 Multi-layered idealized grain model

6.4.1 Model geometry and formulation

A 3-D finite element model is developed in ABAQUS to simulate the multi-layered nature and loading conditions of an idealized MAX phase grain, which constitutes part of a polycrystalline solid. The two categories of inputs to the model are a) material properties or constitutive response, and b) geometric properties. Since MAX phases have a hexagonal crystal structure at a lower length scale, it is assumed that the hexagonal crystals are oriented in a way that the basal direction is the length direction (see Fig. 6.2). The values components of the 3D stiffness matrix for representative MAX phases are obtained from reports on ab initio calculations available in the literature [10]. It is inherently assumed that any intermediate length scale between the crystal unit and sub-grain layers are smeared. In other words, it is assumed that there are no defects and the crystals are perfectly arranged within the idealized grain structure with the basal planes aligned parallel to the layering. A hexagonal crystal has five independent parameters, values of which for Ti_2AlC are listed in Table 6.1.

Table 6.1: Material properties of the anisotropic grain [10]

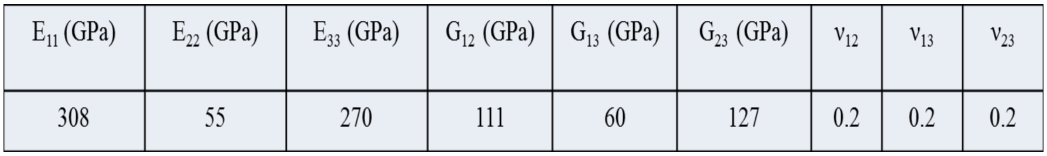

E_{11} (GPa)	E_{22} (GPa)	E_{33} (GPa)	G_{12} (GPa)	G_{13} (GPa)	G_{23} (GPa)	ν_{12}	ν_{13}	ν_{23}
308	55	270	111	60	127	0.2	0.2	0.2

The model consists of layers stacked together to form a grain, geometrical properties of which are inspired by SEM micrographs of as processed Ti_2AlC specimens (and all MAX phases by extension). A grain size distribution has been observed for Ti_2AlC for the results presented in this dissertation and in the literature. Elongated grains having lengths (L) in the range 10-50 μm, and thicknesses (T) of 3-4 μm are observed. The nano-laminate thicknesses (t) are observed to lie in the range 300-1500 nm (0.3-1.5 μm). For the purposes of creating the model, two aspect ratios are varied (see Table 6.2) along with orientations of applied load. The width (W) of the grains (z direction in Fig. 6.2) is found to be on the order of ~5-10 μm. The length-width ratio (L:W) of the grain and length-thickness (L:t) ratio of the nano-layers are the two geometrical parameters varied in the model. The exact values of these parameters are listed in Table 6.1. Each combination is run for the structure oriented at a) 0^{o}, b) 45^{o}, and c) 90^{o} to externally applied compressive loads.

Figure 6.2 shows a 10-layer model (with L:t=33:1 and L:W=4:1) highlighting the dimensions of the representative grain. The x (11 direction) or the length direction is representative of the basal (0001) direction, as mentioned earlier. The y (22) and z (33) directions correspond to the thickness and width directions, respectively.

Table 6.2: Parameters of the grain and sub-grain layers that were studied using the 3D stack model

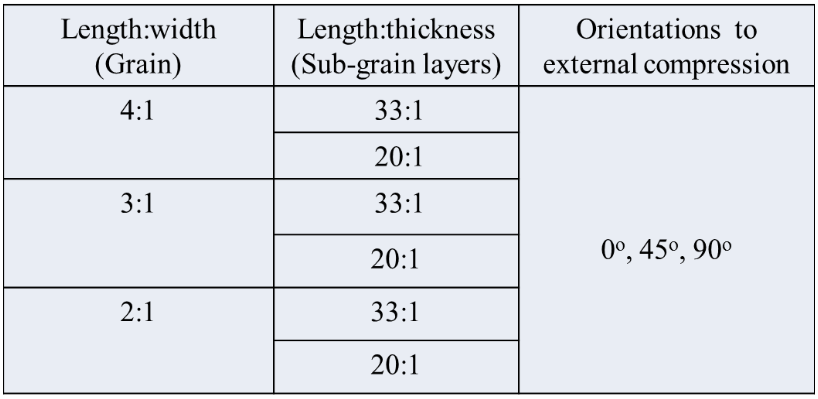

Length:width (Grain)	Length:thickness (Sub-grain layers)	Orientations to external compression
4:1	33:1	0^{o}, 45^{o}, 90^{o}
	20:1	
3:1	33:1	
	20:1	
2:1	33:1	
	20:1	

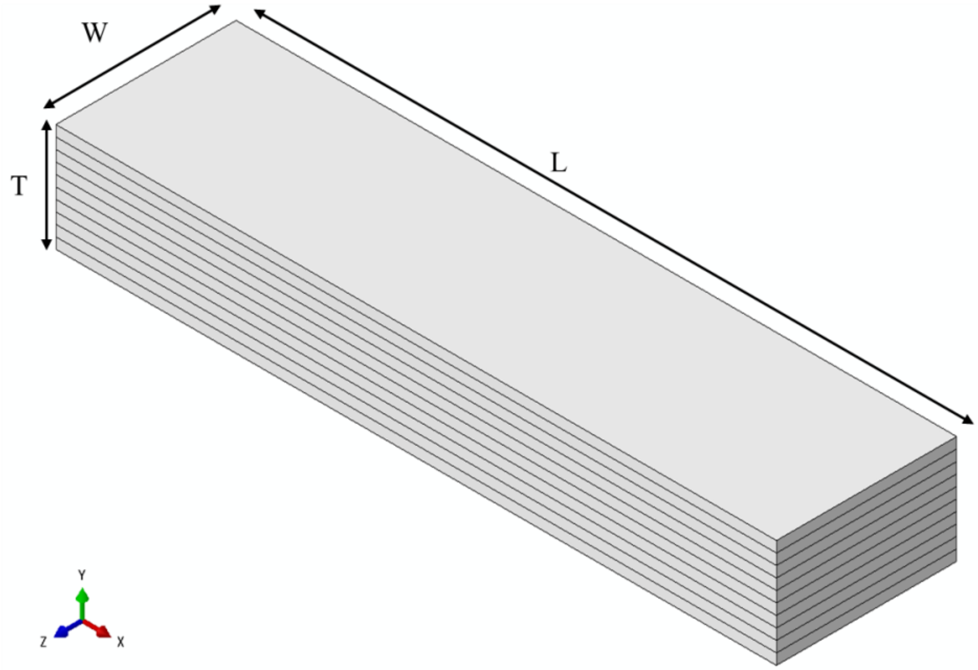

Figure 6.2 Multi-layered 3D model showing an idealized MAX phase grain structure.

The first set of simulations represent the proposed hypothesis central to Guitton's thesis that focus on the continuum scale phenomena of bending and buckling due to the grain-to-grain interaction. The second set of simulations represent the grain neighborhood effects central to Benitez et al.'s work, which is further correlated with reversible motion of mobile dislocations. In the first set, the boundary and loading conditions are chosen based on the post deformation micrographs presented by Guitton et al.[59]. The microstructural analyses in their works reveal large or coarser grains in a "matrix" of equiaxed grains. Coarser grains are oriented randomly (with respect to loading direction) due to the polycrystallinity of the sample and the grains are connected to neighbors at certain connection points. When an external (compressive) load is applied, the grains with different orientations to loading, in contact with each other deform to different degrees (and also via different modes) thereby exerting forces and transferring loads. This leads to a multi-axial loading condition in a grain.

Non-linearity in the geometry is introduced by allowing large rotations, facilitated by the function *NLGEOM in the FE software ABAQUS v6.14[115] for all the simulations. Since the exact interfacial condition between the nano-layers is not currently known, two approaches are used: first, where the inter-layer bonding is perfect which does not allow for any decohesion, and second, where interlayer splitting is allowed by simply stacking the nano-layers (similar to reports on stack of papers, see [111, 114]), except at the boundaries and/or connection points where they are held together. Connection points can be defined as regions on the grain *surface* where it intersects neighboring grains. In three dimensions, the connection *point* translates to a line or even a small area to have enough contribution to the deformation mode at the global level. In this chapter, results on the perfect interface model are discussed. The layers in the perfect interface are “bonded” using a node-merging functionality in ABAQUS. In this procedure, sets of nodes that lie within a tolerance value (specified by the user) are merged to regenerate new nodes that represent an average or smeared condition. This numerical procedure represents a physical bond between the sub-grain layers by treating them as a continuum. The objective of using this approach is to eliminate any interfacial effects (such as stress concentrations or voiding/decohesion) and isolate the deformation modes caused by a multi-axial loading condition.

In the simulations, a non-linear post-buckling analysis is performed as an exercise of extending the Dodwell[114] approach to a three dimensional computational environment.

This analysis is representative of a grain where the applied compressive load is parallel to the basal plane (or layering) and there are no surrounding grain effects. A linear eigenvalue analysis is first performed followed by the non-linear Riks arc-length method to determine the post-buckle response. The zero stress state for the Riks analysis step is the buckled configuration, scaled to different degrees and systematically varied to study the role of imperfections, using the function *IMPERFECTION in the input file of ABAQUS v6.14.

Figure 6.3 shows a grain stack with all the boundary conditions that are incorporated in the model to create a multi-axial loading scenario [59]. The arrows and circles point to the BCs that are present due to neighboring grain effects. Two specific conditions hypothesized in Guitton's work are mechanistically represented here as follows:

i) First, at the connection point between grains, a neighbor can resist the deformation of the grain under consideration, modeled using a clamp type BC, as shown on the top surface in Fig. 6.3. The other possibility is that it can allow for some constrained deformation as modeled using a localized roller bed.

ii) Second, the neighboring grains can also push and external additional on the grain under consideration due to an externally applied load, in the vicinity of the connection points. The yellow arrows encircled by orange circles represent this condition.

The effect of other layers (and grains) in the confined polycrystalline solid is represented by an overburden pressure type loading in Y and Z directions that are in the ratio 1:10 to the applied external load. The external load is applied as concentrated loads on nodes on the right and top surface, as shown in Fig. 6.3.

For the second set of simulations, a representative grain underlying the hypothesis in Benitez et al.[40] is modeled. Figures 6.4(a) and (b) show the boundary conditions on a confined grain depicting these scenarios – first, where the considered grain is completely surrounded by small equiaxed grains (Fig. 6.4(a)) and second, wherein the grain under consideration is partially surrounded by the equiaxed grains and is connected to one large grain (circle in Fig. 6.4(b)). The results from this portion of the analysis are discussed in section 6.4.2.

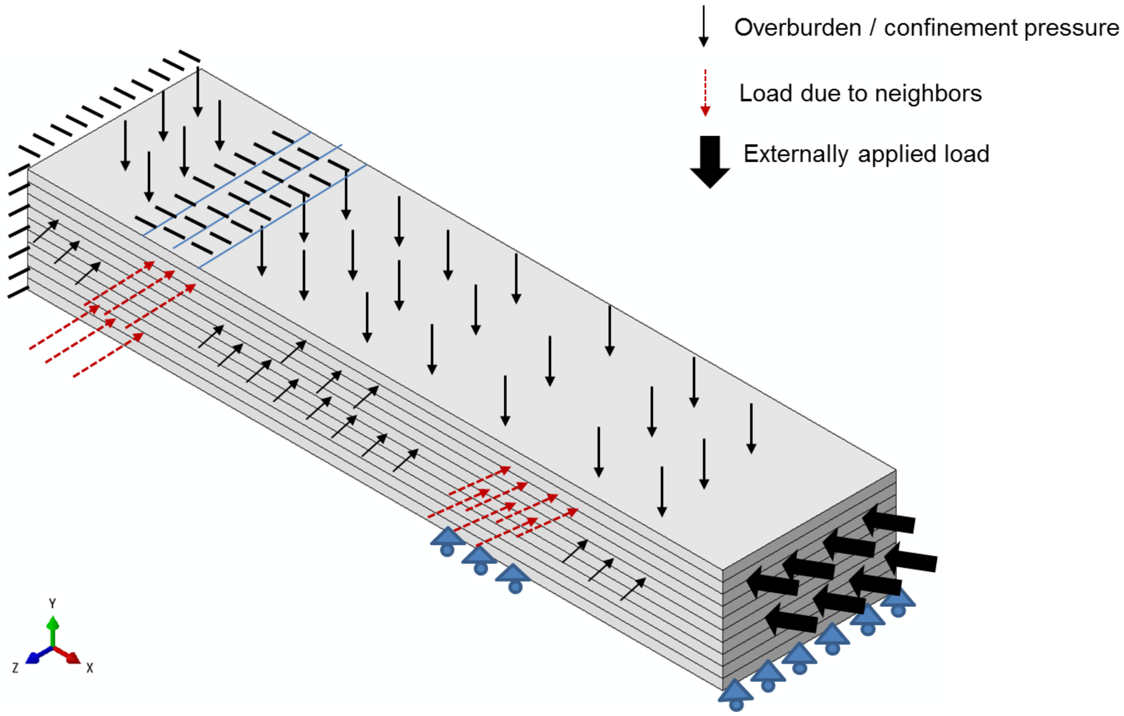

Figure 6.3 Boundary and loading conditions depicting multi-axial loading in an idealized MAX phase grain .

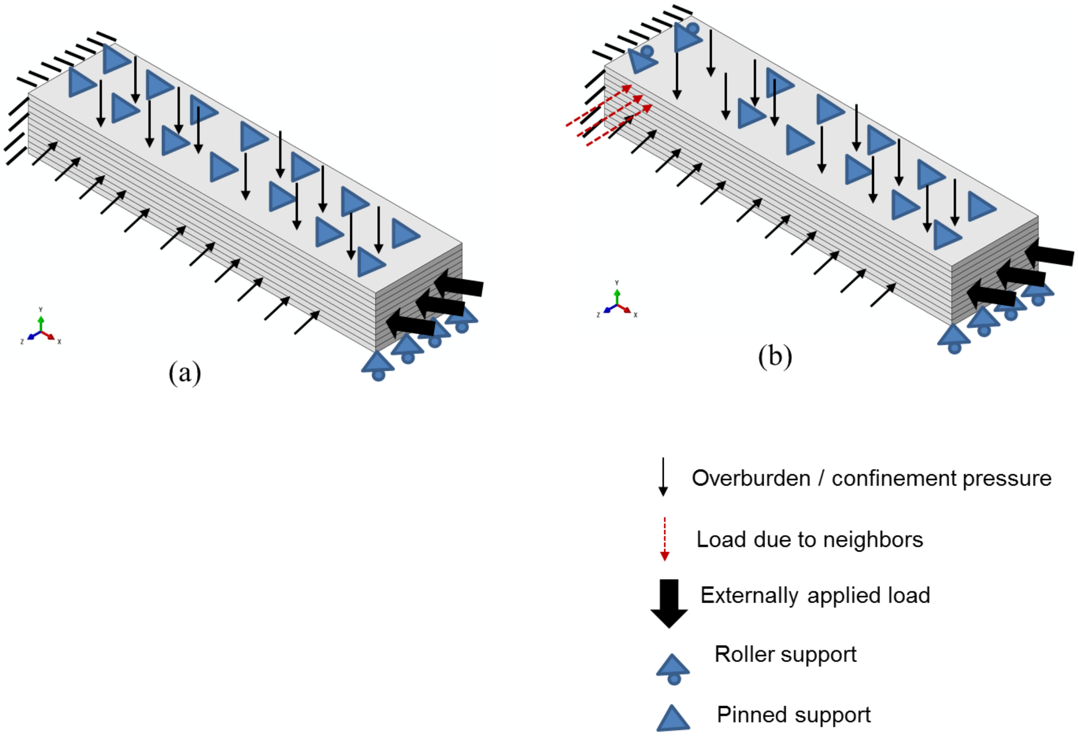

Figure 6.4 Boundary and loading conditions representative of equiaxed surroundings in accordance to micrographs in Benitez et al.[40], showing a) a fully constrained condition, and b) one connecting large grain (circled region).

6.4.2 Simulation results and discussion

i) Uniaxial loading

An initially straight beam (representing a series of bonded nanolayers in a grain) undergoes elastic buckling and the deformed configuration is used as input to perform the post-buckling analysis using Riks' approach. The initially buckled configuration is considered as an initial imperfection whereby the curvature is defined as the angle that the curved beam makes with the horizontal (x) axis. The grain geometry considered for this portion of the analysis is shown in Table 6.3. A node-wise uniaxial displacement control is applied along the x-axis (11 direction) on surface 2(Fig. 6.3(a)) to obtain the eigenvalues and eigenmodes. The first eigenmode is used to perform post-buckling analysis.

Typically, Riks method is used following an eigenvalue buckle analysis step, and therefore any loads that exist are treated as "dead" loads with constant magnitude. A load which is defined / prescribed during setting up of this method is a "reference" load. The prescribed loads are ramped from an initial dead load values. The total load can therefore be expressed as:

$$P_{total} = P_0 + \lambda\,(P_{ref} - P_0)\ldots\ldots\ldots\ldots\ldots\ldots\ldots\ldots\ldots\ldots\ldots\ldots\ldots\ldots(6.1)$$

P_0 is the dead load, and P_{ref} is the prescribed load during the set-up of the Riks analysis. λ is a load proportionality factor that is found as part of the solution.

Newton's method is used to solve the nonlinear equilibrium equations, where the user inputs an initial increment in arc length along the equilibrium path (Δl_{in}), when the analysis is set-up (similar to an initial guess). The initial load proportionality factor is computed on the basis of this input, as:

$$\Delta\lambda_{in} = \frac{\Delta l_{in}}{l_{period}}\ldots\ldots\ldots\ldots\ldots\ldots\ldots\ldots\ldots\ldots\ldots\ldots\ldots\ldots(6.2)$$

l_{period} is user-specified total arc length scale factor which is typically set to 1. Subsequent iterations and increments involve automatic computation of increments of λ, which forms a part of a solution and is not "controlled".

Table 6.3: Geometry of grain and orientation to external loading for buckling and Riks' analysis

Length:width (Grain)	Length:thickness (Sub-grain layers)	Orientation to external compression
4:1	33:1	0°

The results from uniaxial buckling and Riks analysis is first presented in this section, followed by a detailed discussion on the effect of geometry and orientation on the multi-axial state of stress. Figure 6.5 shows typical stress-strain output following a Riks analysis in an anisotropic idealized grain structure, for different degrees of beam curvature. Therefore, no imperfection implies a flat grain (i.e. no initial curvature). Overall, it is observed that the stress in the grain structure for a given applied displacement decreases with increasing imperfection. The stress-strain response for no or small imperfections (0 and 1 degree) show an initial linear regime following which a small transition regime leading into a non-linear regime is observed. This transition regime is plateau-like for the perfect grain (no imperfection case). On the other hand, the transition shows a certain drop in stress for the beam with small imperfection. As the imperfection is increased, the transition regime disappears and the response becomes increasingly non-linear.

Figure 6.6(a) shows a one-to-one mapping of the global stress-strain response to the local stress field evolution. It is clearly observed that the beginning of the transition in the global stress-strain regime corresponds to the point where buckling of the grain begins. The fact that the transition regime vanishes with increasing imperfection points towards existence of a critical angle of the buckled configuration, beyond which the response is always non-linear (for example, 3 and 10 degree cases).

Analyses of the stress / strain contour maps shown in Fig. 6.6(b) reveal that the maximum principal direction coincides with the 11 direction, which is typical for an elastic isotropic solid. This observation indicates that the post-buckled response is not due to the inherent material anisotropy. Therefore, the non-linearity in the stress-strain curve in Fig. 6.6(a) can be attributed to the initial curvature of the beam. This shows how beam curvature could be of relevance in determining the deformation response of a multi-layered structure under pure uniaxial compression. Next, an idealized grain is systematically studied under multi-axial loading.

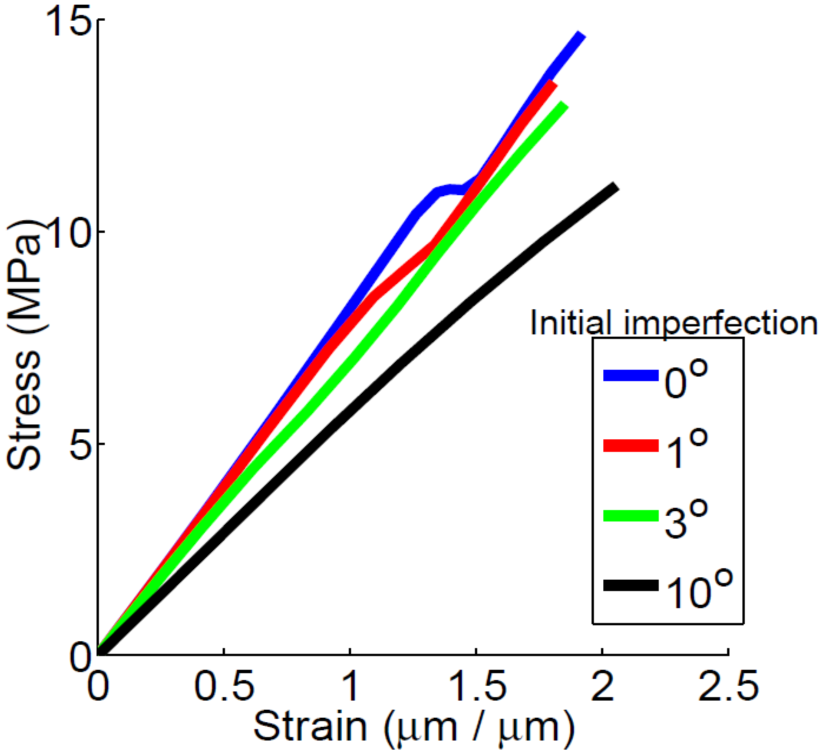

Figure 6.5 Global stress-strain response of the idealized grain structure following a post-buckle analysis under uniaxial compressive loading.

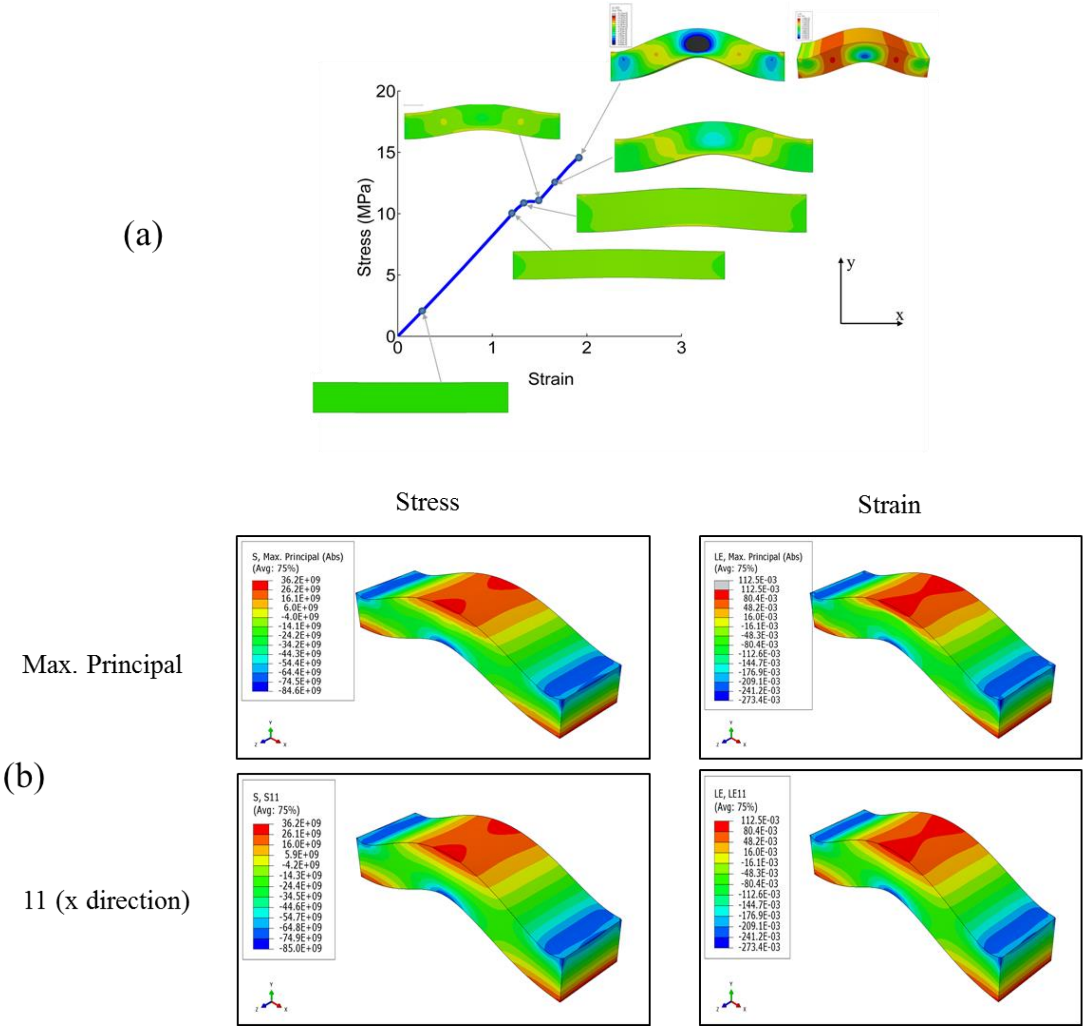

Figure 6.6 a) Global stress-strain response and field evolution characteristics in the 22 (y direction) corresponding to points in the plot demonstrating that the transition regime corresponds to the initial buckle, and b) stress and strain field contours showing similar field patterns in maximum principal and 11 directions.

The uniaxial buckling compression is a direct extension of Dodwell's approach to 3D and captures further information regarding the stress-strain field evolution patterns. In the 22 (y direction) field maps surrounding the stress-strain plot, a high stress / strain region is observed at the apex region of the buckled structure. Therefore, it is likely that with further increase in loading, that region will form a localized sharp hinge typically observed in a chevron type fold. An important result from this portion of the analysis is the role of initial curvature that demonstrates existence of a critical angle beyond which the stress-strain response is fully non-linear with negligible linearity in the small stress/strain regime.

The role of anisotropy in the x-y deformation plane is analyzed by comparing the deformation mode post-buckling with a linear elastic isotropic material having the exact same properties (elastic modulus and poisson’s ratio) as Ti_2AlC. A uniaxial loading case using Riks analysis method is used for the comparison to isolate the effect of material properties. Figure 6.7 shows the post-buckled configurations for the two different material properties. It is observed that the anisotropic elastic material shows bulging in the limb regions (defined earlier in chapter 1) with tendency to form a hinge like zone at the apex. This region also shows existence of a high localized compressive stress. The isotropic elastic case, on the other hand, has a more even rounded like configuration where the stress distributions are evenly distributed without any localization. Therefore, the simulation result points to the role of material anisotropy in controlling the shape of the response

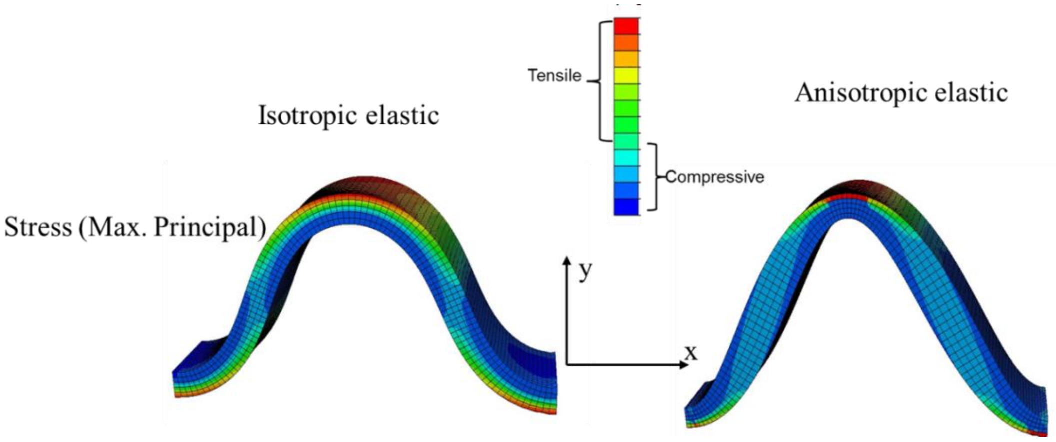

Figure 6.7 Maximum Principal stress contours for isotopic and anisotropic elastic beams subjected to uniaxial compressive load following a Riks postbuckle analysis.

ii) Multiaxial loading

The case of multi-axial loading representing the idealized MAX phase grain is now considered. Three representative cases from Table 6.2 are considered, which are representative of all the data sets obtained from the simulations, as follows: i) Case I, where L:W=4; L:t=33, ii) Case II, L:W=4; L:t=20, and iii) Case III, L:W=2; L:t=33. For all the cases, the global load versus displacement relationship for the entire grain is first discussed followed by 3D stress/strain field evolutions for the three orientations. It is worthwhile to reiterate here that the choices of orientations represent longitudinal hard grain (0^o), soft grain (45^o) with respect to preferable orientation for slip, and a transversal hard grain (90^o) according to the definition provided by Benitez et al. (see Fig. 1 in [40]). Angles with respect to direction of loading are in a completely different sense to the imperfection analysis presented earlier.

The direction of the loading with respect to the layering direction (x / 11 direction) was constant in the previous case, which is varied in this portion of the analysis to represent grain classes, thereby contributing to the multi-axial effect among other factors. It must be noted that Riks arc-length procedure is strictly valid for uniaxial loading and therefore a general/static loading with nonlinear geometry (*NLGEOM) functionality is used for the analyses presented in this portion.

Furthermore, the stress-strain response in the previous case was obtained by outputting the force-displacement response and normalizing it with respect to geometrical properties (i.e. cross sectional area of loading face and length of grain) of the idealized grain given the response was uniaxial. However, for a multi-axial condition and with evidence of anisotropy in response (as shown later), deriving the accurate stress-strain response is non-trivial. Therefore, a load versus displacement relationship is presented.

i) Case I: L:W=4; L:t=33

Figure 6.8 shows the load-displacement relationship obtained from simulation under multi-axial loading, as dictated by the BCs pointed out earlier (Figure 6.3). Note that the displacement shown here is the axial compressive displacement (11 direction) before the grain structure starts bending.

It is observed that the response is near-linear for layer parallel compression. However, with increasing angles between the layer parallel direction and direction of loading, the response shows an upturn after an initial displacement until which it closely follows the zero degree response. This observation indicates an orientation dependent hardening mechanism during the axial pre-bend regime.

Further insight and details regarding the deformation modes are obtained by analyzing the stress/strain contour plots. Figures 6.9(a)-(f), 6.10(a)-(f), and 6.11(a)-(f) show the stress and strain field contours for the zero, 45^o and 90^o cases respectively in the principal, 11 and 22 directions. The zero degree case shows a bending type configuration in the x-z (11-33) plane along with stress concentrations in regions that are representative of grain connection. This observation is in agreement to Guitton's hypothesis made from post deformed micrographs wherein it was pointed out that layer parallel compression would to lead to a distortion type deformation mode, typically observed in post fracture SEM micrographs here. The connection regions (circled in Fig. 6.9(d)) indicate stress concentrations that occur due to the additional BC introduced at those points. Some localized folding like modes are observed that are not widespread on post-fracture SEM images presented here. This comment notwithstanding it must be noted that a one to one mapping of the applied external compressive load direction and folds observed in the SEM is unknown, and therefore their connection is still largely unresolved hence the current debate between the different proposed theories. The contour maps reveal that the maximum principal stress contour has similar stresses in comparison to stresses in the 11 direction, thereby indicating that the 11 direction is the direction of maximum principal stress.

Figures 6.10(a)-(f) show the stress and strain contours for the 45^o orientation to external loading. A clear difference in the deformation mode (grain bending in the x-y plane) is observed in comparison to the axial loading scenario. It must be noted that all the deformation contours presented in this chapter are scaled two times to clearly reveal the features of deformation. The maximum tensile stress (and strain) occurs in vicinity of one of the connection points (red regions on the contour plots) whereas the maximum compressive stresses (and strains) in the middle portion of the structure, as expected. The regions of high strain and stress for each direction (max principal, 11, and 22 directions) match. Furthermore, it can be clearly observed from contour maps that the 11 direction is the maximum principal direction. An analysis of Figs. 6.11 (a)-(f) show a similar result with respect to the bending deformation mode, direction of maximum principal stresses and matching of high stress and strain regions for a given direction. The observations from this portion of the analysis on 45^o (soft grain configuration) and 90^o (transversal hard grain configuration) shows how bending deformation under a multi-axial state of stress. On the other hand, the 0^o (longitudinal hard grain case) shows a mode different from a bending type configuration in the x-y plane.

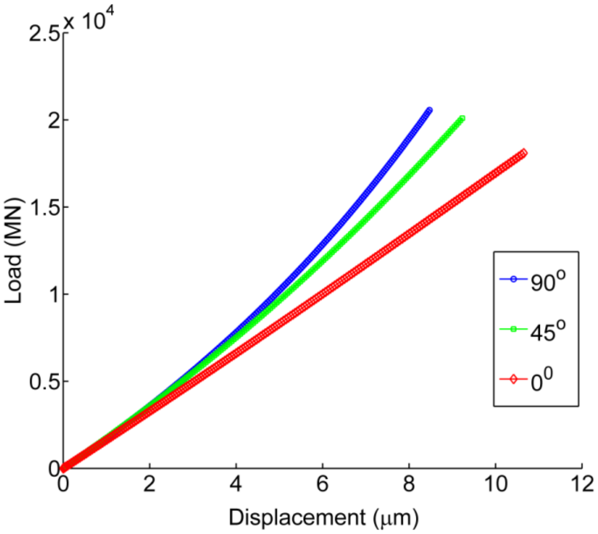

Figure 6.8 Load versus displacement relationship for an idealized grain structure with geometrical parameters, L:W=4 and L:t=33.

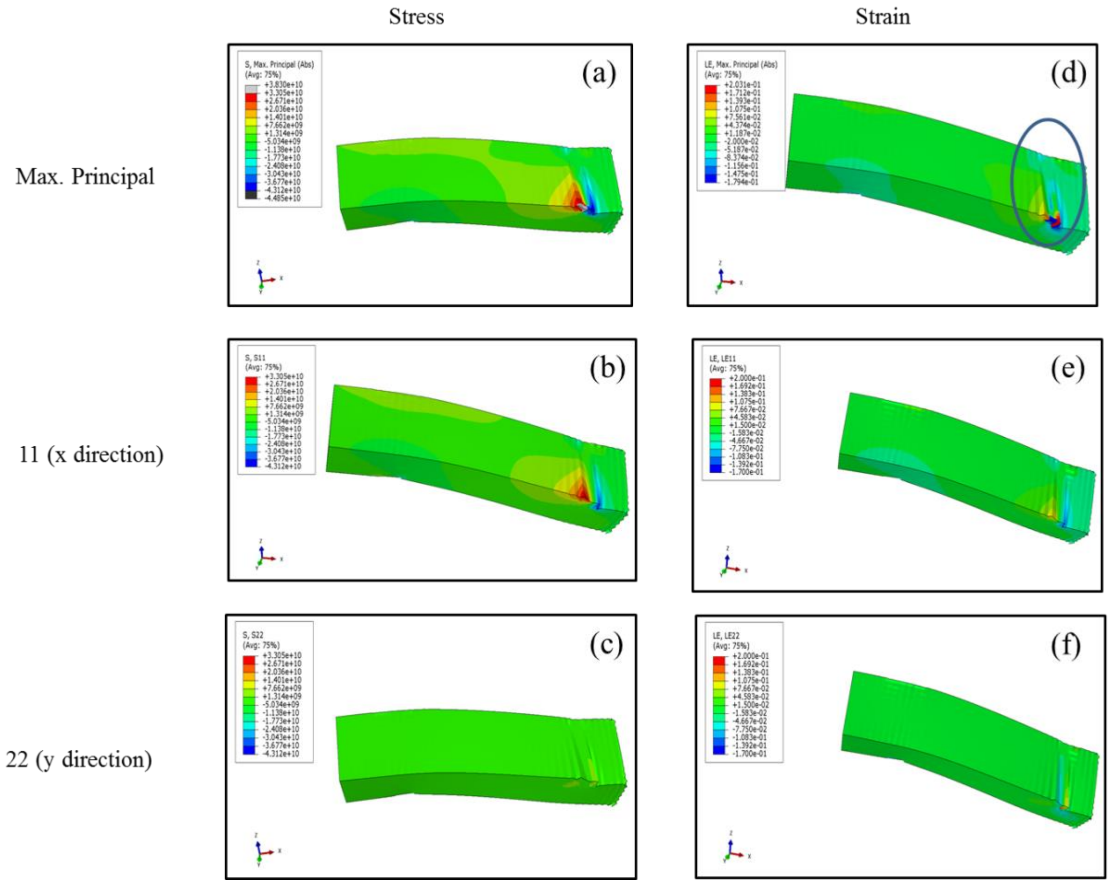

Figure 6.9 Maximum principal, 11, and 22 direction stress (a-c) and strain (d-f) field contours for L:W=4 and L:t=33, showing the deformed mode following a multi-axial loading condition with external load applied parallel to the layer direction (x direction).

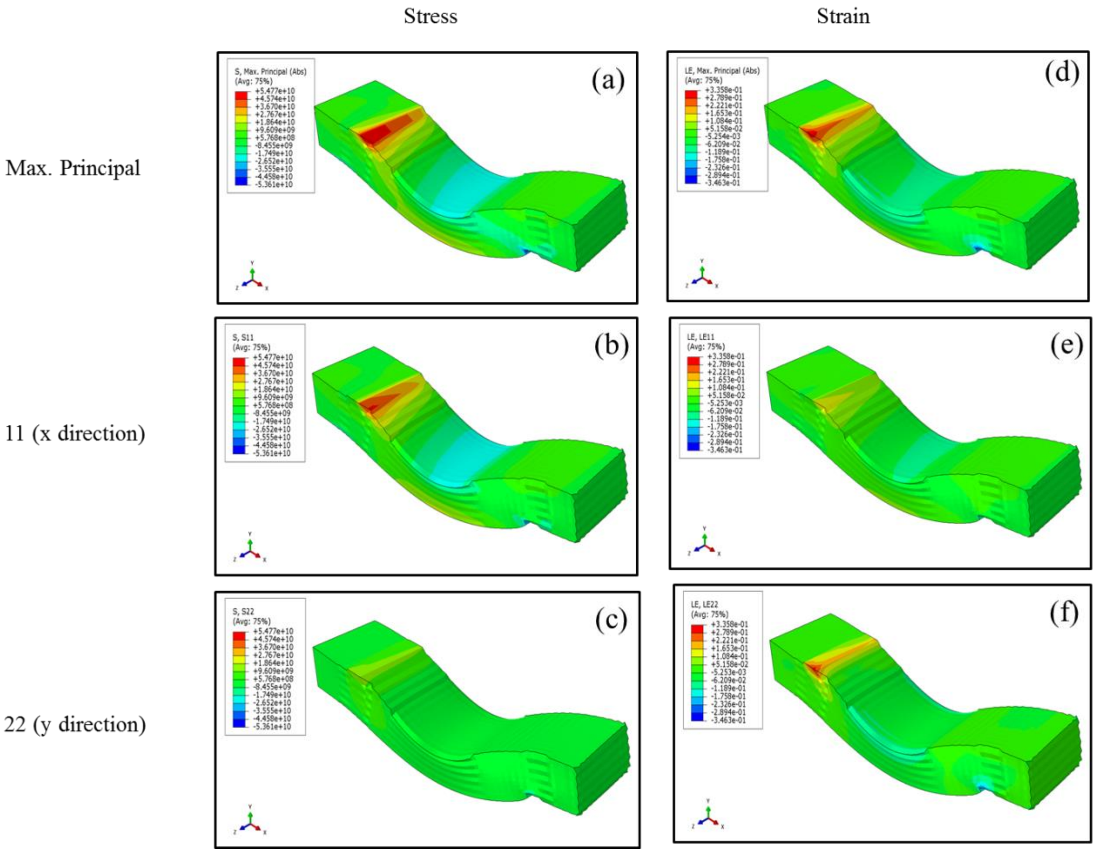

Figure 6.10 Maximum principal, 11, and 22 direction stress (a-c) and strain field (d-f) contours for L:W=4 and L:t=33, showing the deformed mode following a multi-axial loading condition with external compressive loading applied at an angle 45^o to x direction.

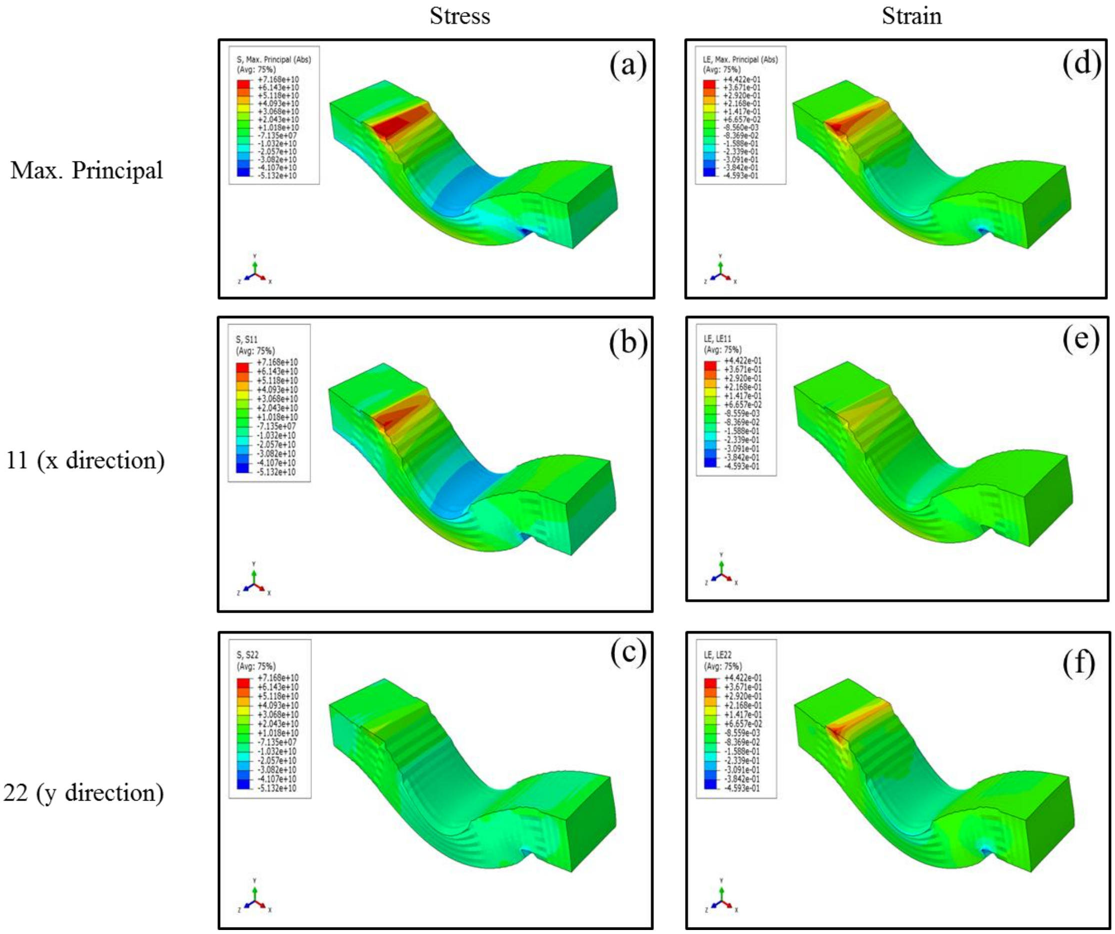

Figure 6.11 Maximum principal, 11, and 22 direction stress (a-c) and strain (d-f) field contours for L:W=4 and L:t=33, showing the deformed mode following a multi-axial loading condition with external load applied perpendicular or transverse to the layer direction (x direction).

ii) Case II: L:W=4; L:t=20

Now, the effect of the number of layers on the response is studied by varying the aspect ratio of the representative nano-laminate or sub-grain layer (L:t). The global geometrical properties of the grains are exactly the same as the previous case. That is to say, the numbers of representative nano-laminates are reduced (6 as opposed to 10) to maintain the overall aspect ratio. This parameter is varied in accordance with SEM micrographs where a range of nano-laminate thicknesses from 300-1500 nm has been observed and reported. The previous case was the lower bound with an aspect ratio (L:t) of 33:1 and this case represents a value approximately in the median of that range (~760 nm).

Figure 6.12 shows the load versus displacement plot of a grain oriented axially, at 45^o, and transverse to the applied external compressive load similar to previous case. Note that the boundary conditions due to neighboring grains were exactly the same. A similar variation of the global load versus displacement is observed where the axial loading has the highest displacement for a given load (all analyses were load controlled) which gradually reduced with increasing orientation angles. A near-linear response was obtained for all cases, in contrast to the previous case. An interesting contrast in the response (compared to case I) however is the order of magnitude of loads at which the idealized grain deforms. A comparison with the response in Fig. 6.8 shows a drop in load by nearly 3.5 times. This points towards the fact that for a given grain, having a higher number of layers (assuming they are all perfectly bonded) provides greater resistance to applied load and compresses axially by a greater degree before bending and/or kinking (indicated by higher displacements).

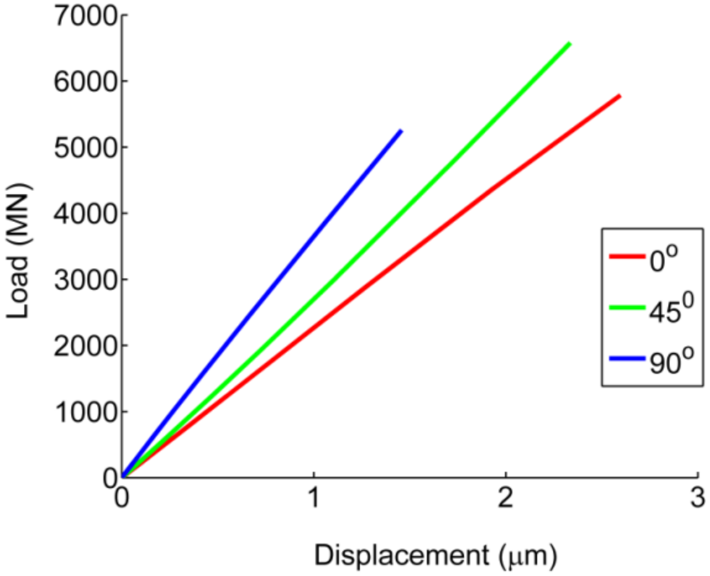

Figure 6.12 Load versus displacement relationship for an idealized grain structure with grain L:W=4 and L:t=20.

Figures 6.13(a)-(f), 6.14(a)-(f), and 6.15(a)-(f) show the stress and stress contours in maximum principal, 11, and 22 directions for the 0, 45 and 90 orientations respectively. The zero degree or layer parallel external loading (or longitudinal hard grain) shows a distorted structure, similar to case I. However, the deformation in the x-z plane is not as pronounced and instead a ridge like deformation mode, reminiscent of a stove pipe type kinking (along the x-y plane) is observed. This ridge formation (shown by circle in Fig. 6.13(b)) is observed in the vicinity of a grain connection region (see Fig.6.3) and it is inferred that connection regions can act a stress raiser thereby contributing to localized modes and even kinking.

The stress and strain patterns in 11 direction are in good agreement with the maximum principal direction patterns for all three different orientations (see (a) and (b) contour maps in Figs. 6.13-6.15). The higher stress and strain regions however don’t occur at the same spot for a given direction (both 11 and maximum principal). These observations indicate role of anisotropy in the deformation modes as well as occurrence of localized modes that are either stress controlled or strain controlled.

A bulging or out of plane curving mode of deformation is observed for both soft grain and transversal hard grain type orientations i.e. 45^o and 90^o to applied compression respectively. These are shown by arrows in Figs. 6.14(d) and (e) It must be noted that these features of deformation were less pronounced for the previous case. Furthermore, stress variations from layer to layer are not visibly prominent in comparison to the modes shown in case I.

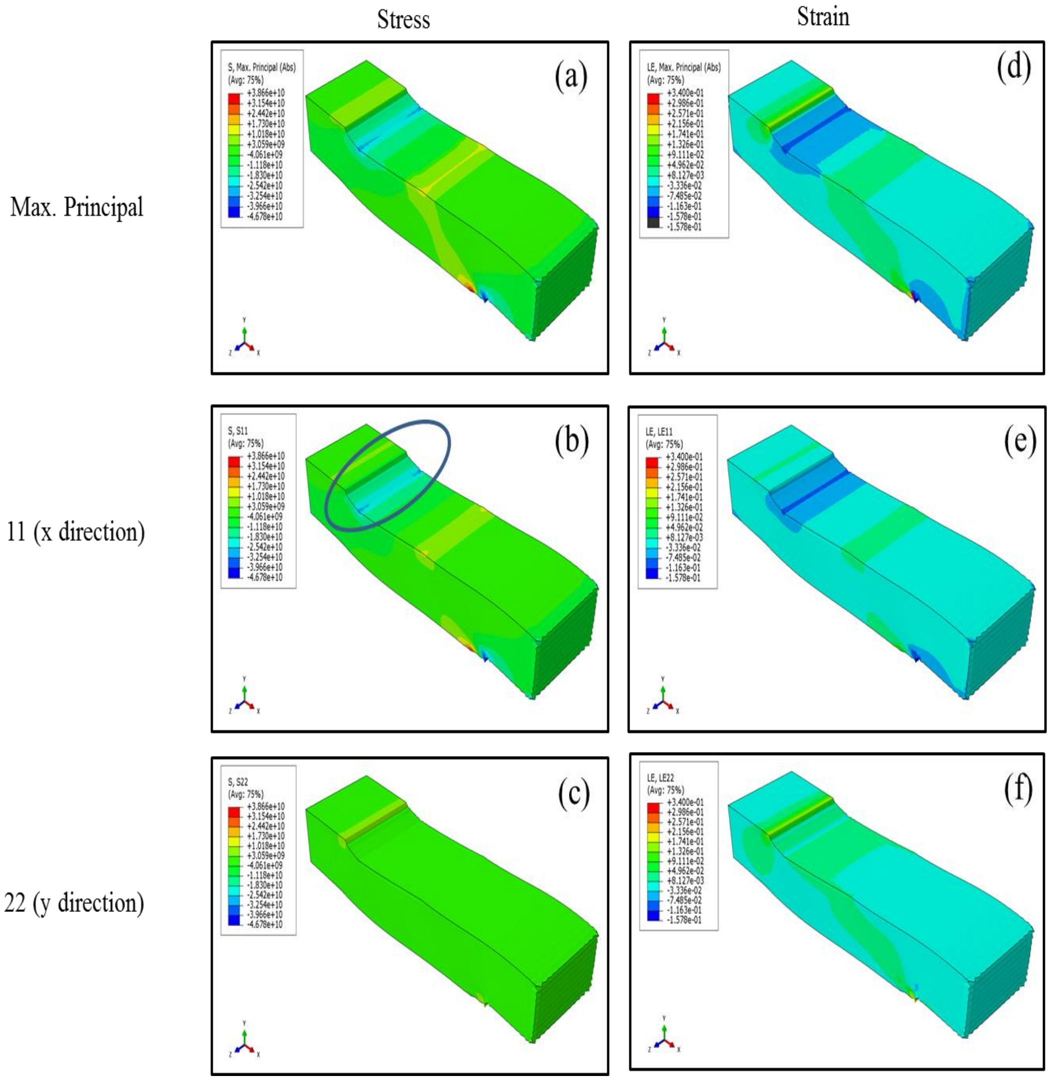

Figure 6.13 Principal, 11, and 22 direction stress (a-c) and strain (d-f) field contours for L:W=4 and L:t=20, showing the deformed mode following a multi-axial loading condition with external load applied axial or parallel to the layer direction (x direction).

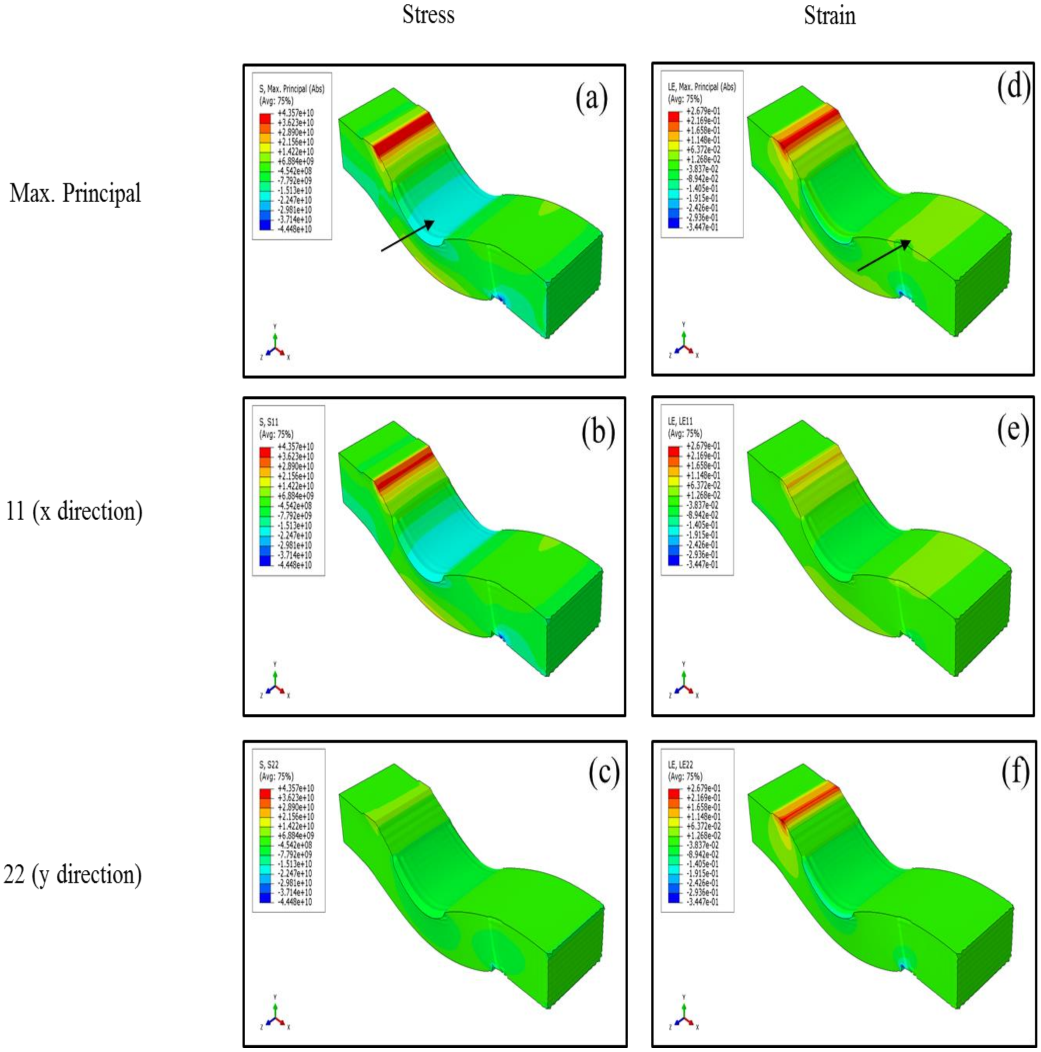

Figure 6.14 Principal, 11, and 22 direction stress (a-c) and strain (d-f) field contours for L:W=4 and L:t=20, showing the deformed mode following a multi-axial loading condition with external load applied at 45^{o} the layer direction (x direction).

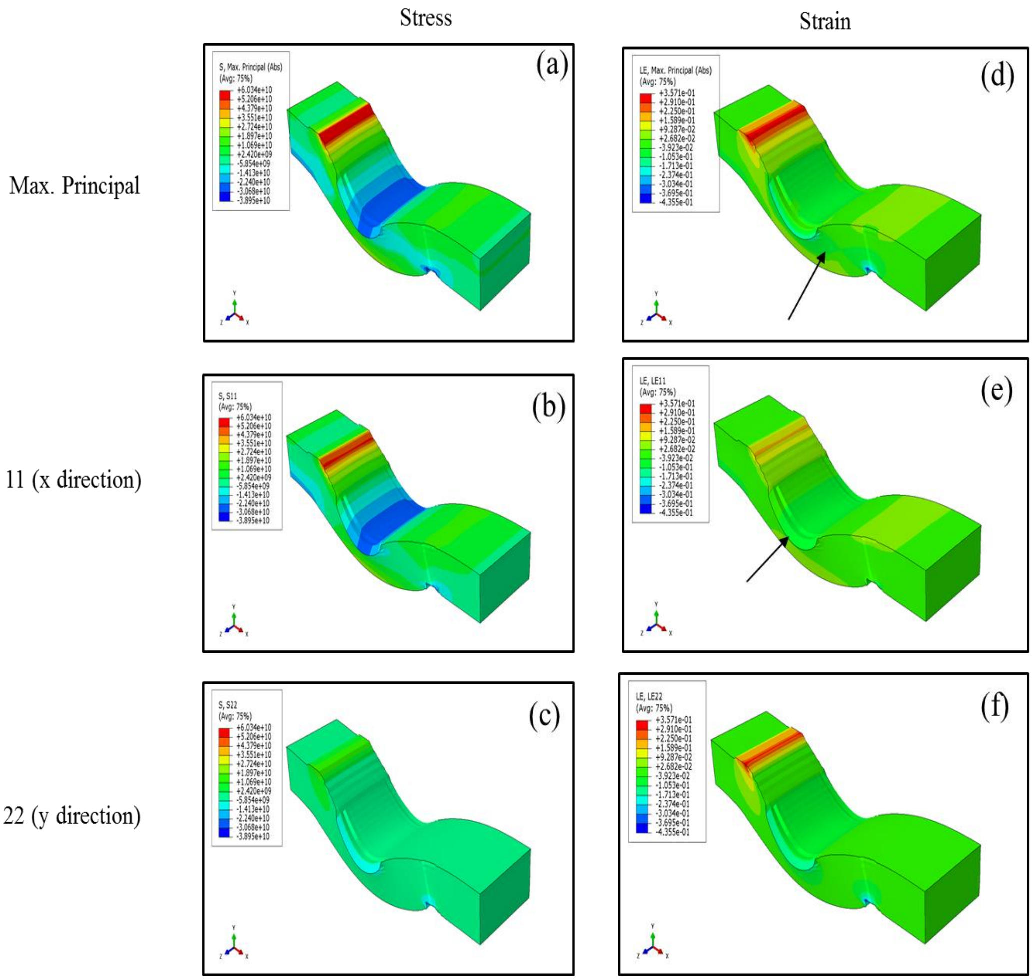

Figure 6.15 Principal, 11, and 22 direction stress (a-c) and strain (d-f) field contours for L:W=4 and L:t=20, showing the deformed mode following a multi-axial loading condition with external load applied transverse to the layer direction (x direction).

iii) Case III: L:W=2; L:t=33

The case with a lower L:W ratio of the grain and aspect ratio of sub-grain layers similar to the first case (33:1) is presented here. Figure 6.16 shows the global stress-strain response of the wider grain for three different orientations similar to the previous cases. The displacements are found to be much lower thereby indicating a stiffer response, which agrees with intuition. The stiffnesses of the three configuration relative to one another also showed a similar trend ($90^o > 45^o > 0^o$). Furthermore, the response becomes increasingly linear compared to the previous cases.

Figures 6.17 (a)-(f) show the stress/strain contour maps for the longitudinal hard grain configuration (or layer parallel external loading). The deformation mode shows primarily axial deformation with negligible bending. This is due to the increased stiffness of the structure due to a lower L:W ratio. Figures 6.18(a)-(f) and Figs. 6.19(a)-(f) show the corresponding contour maps for the 45^o and 90^o orientation (soft and transversal hard grains) respectively. The contour maps and deformation modes for two different orientations resemble each other very closely, in contrast to previous cases. In the previous cases, transversal hard grains (90^o to externally *applied* loading) showed a greater degree of bending compared to the soft grain (45^o to externally *applied* loading) configuration. However, in this case, there isn’t an observable difference. This indicates that for certain aspect ratios of the grain, changing orientations does not affect the deformation modes under a multi-axial loading.

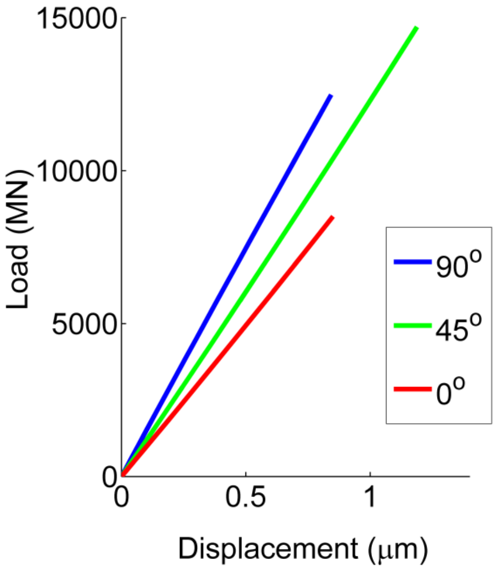

Figure 6.16 Load versus displacement relationship for an idealized grain structure with grain L:W=2 and L:t=33.

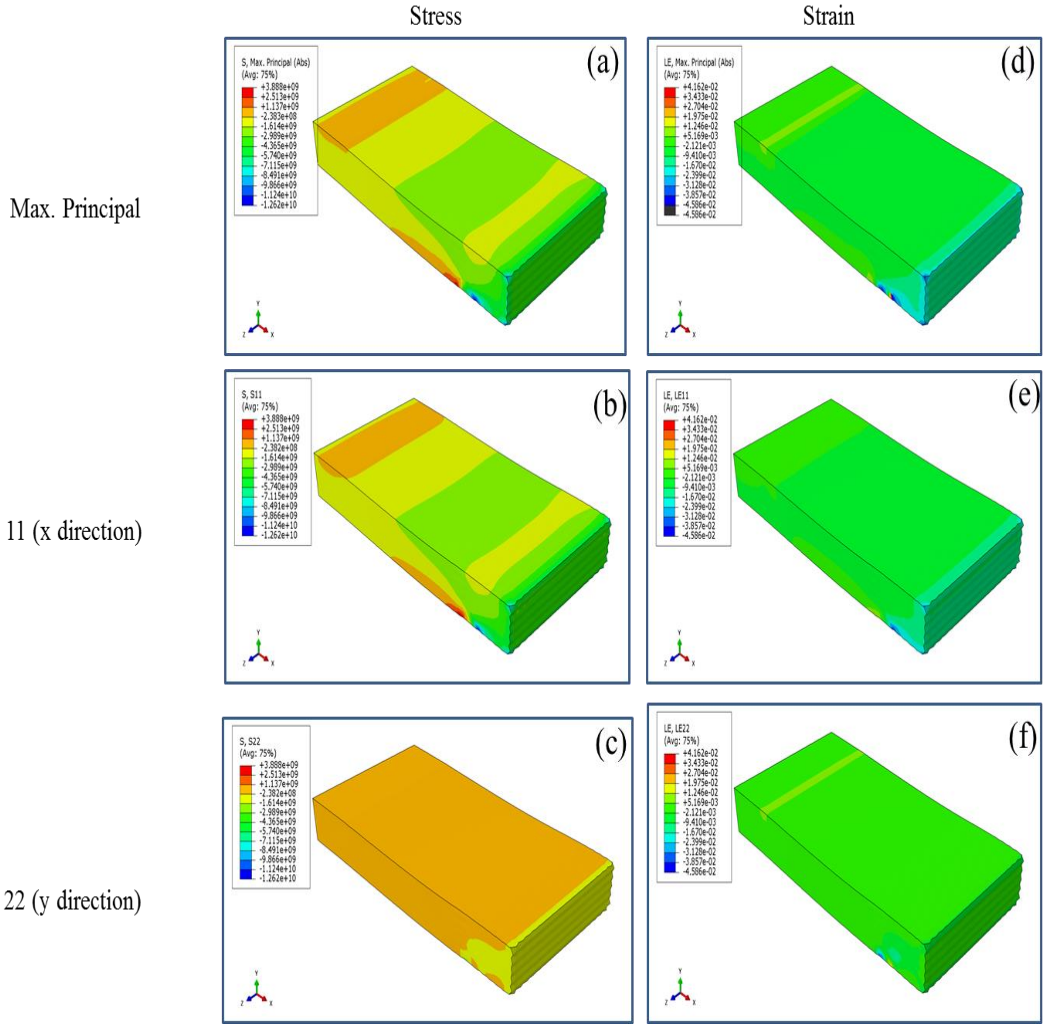

Figure 6.17 Maximum Principal, 11, and 22 direction stress (a-c) and strain (d-f) field contours for L:W=2 and L:t=33, showing the deformed mode following a multi-axial loading condition with external load applied parallel to the layer direction (x direction).

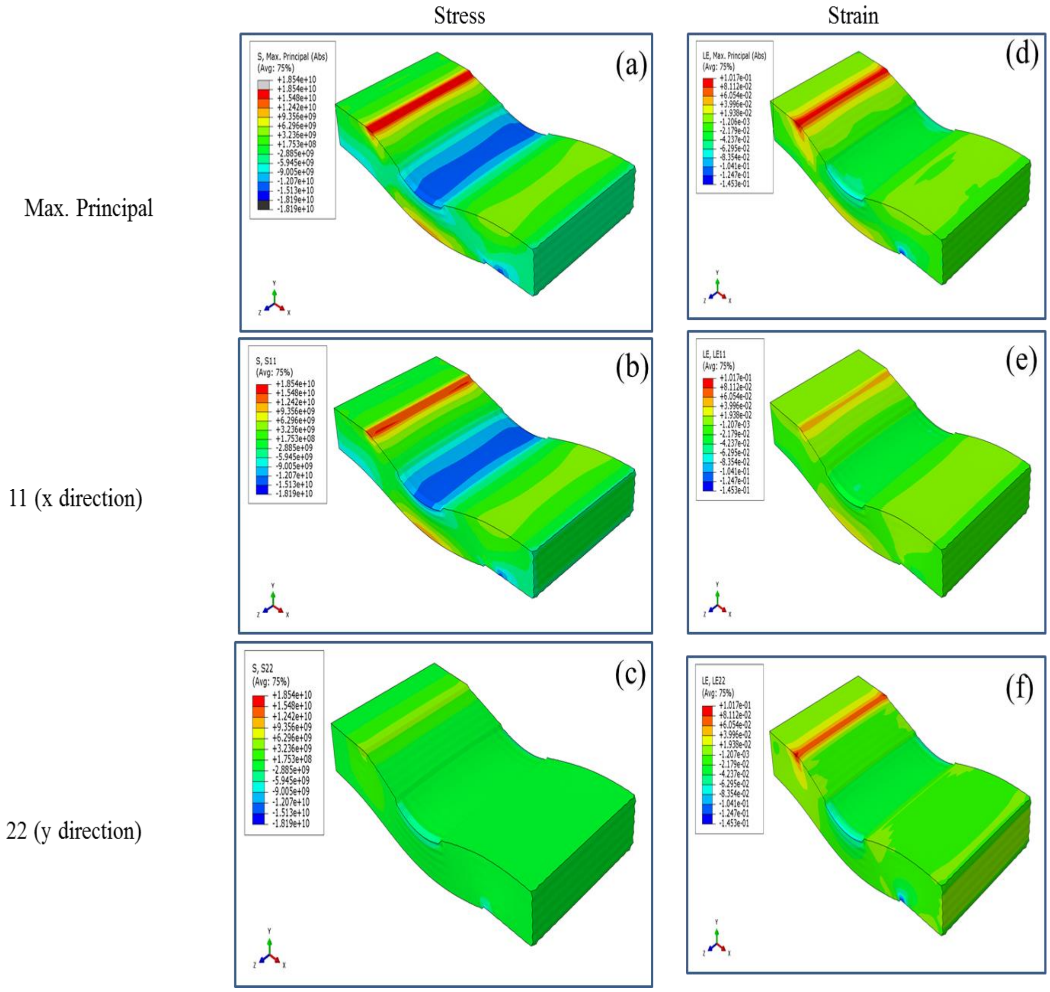

Figure 6.18 Maximum Principal, 11, and 22 direction stress (a-c) and strain (d-f) field contours for L:W=2 and L:t=33, showing the deformed mode following a multi-axial loading condition with external load applied at 45^{o} to the layer direction (x direction).

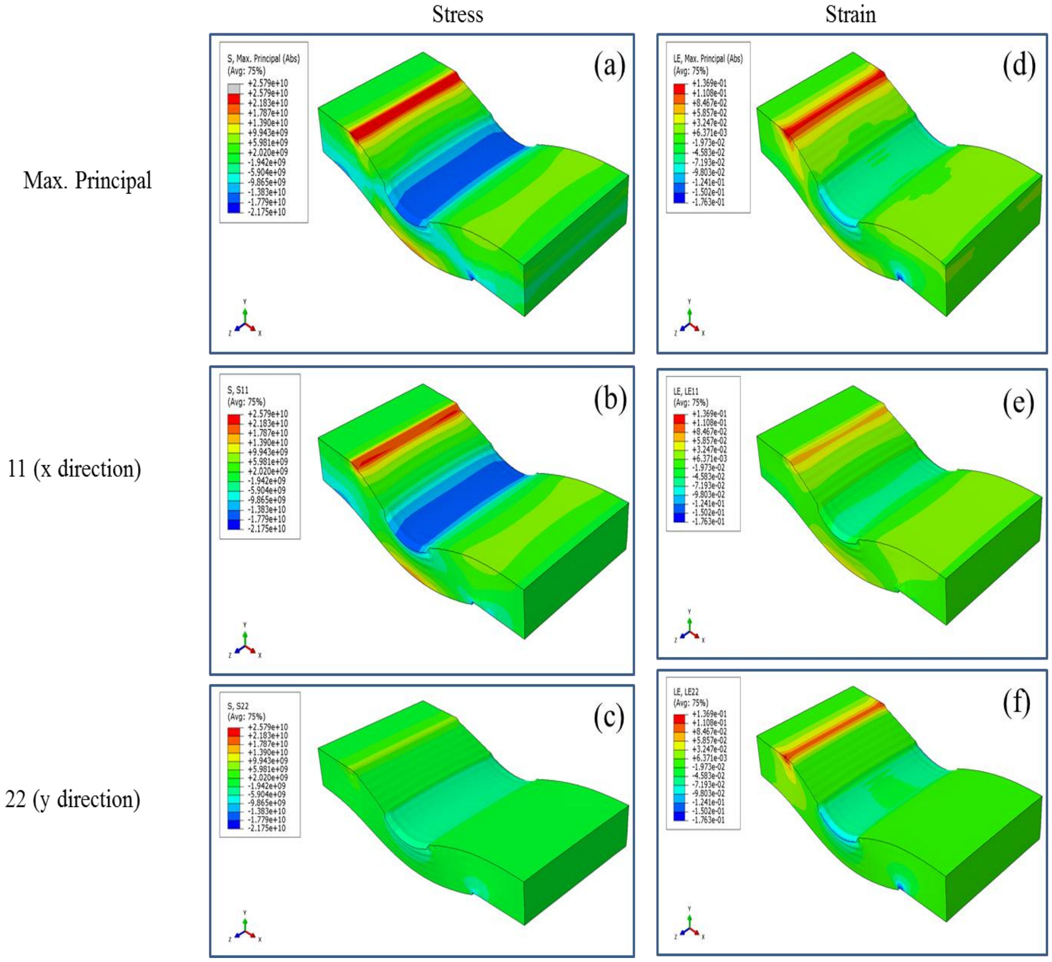

Figure 6.19 Maximum Principal, 11, and 22 direction stress (a-c) and strain (d-f) field contours for L:W=2 and L:t=33, showing the deformed mode following a multi-axial loading condition with external load applied parallel to the layer direction (x direction).

6.4.3 Critical Analysis and Summary

The results obtained from three cases representative of different geometrical parameters of a MAX phase grain are combined together and discussed in much greater detail here. Figures 6.20(a)-(i) present a summary of observations by combining the maximum principal stress contours for different orientations and geometries. A careful analysis is performed by focusing on the stress field and deformation mode in the x-y plane that is of primary importance and relevance to the layered beam approach. The deformation modes in different grain orientations to loading i.e. longitudinal hard, soft, and transverse hard configurations, (0^o, 45^o, and 90^o to externally *applied* loading) are discussed and analyzed in much greater detail in this section, by analyzing the images in Fig. 6.20 row and column wise.

The row wise analysis reveals the effect of geometry for the different orientations to externally applied loading. The circled regions in the top row indicate areas of stress concentrations due to connection points with other neighboring grains. The slight tapering of the grain structure from left to right in Figs. 6.20 (a) and (g) is due to deformation of the beam in the x-z (11-33) plane, that is not clearly visible in this direction. The lower number of sub-grain layering (Fig. 6.20(d)) leads to a ridge or stove pipe type kink formation at the point of grain connection, as shown by an arrow. The 45^o loading configurations show some differences with regards to the extent of folding observed in grains with different geometries (Figs. 6.20(b)-(h)). The higher L:W aspect ratios (Fig. 6.20(b) and (e)) show an asymmetric type folding which becomes more symmetric with a lower L:W ratio.

Furthermore, a comparison between Figs. 6.20(b) and (e) reveals that a higher aspect ratio of the sub-grain layers (i.e. L:t), the amount of bending is higher and has a bulge type appearance, where portion of the beam protrudes in the z direction (shown by an arrow). For the grain structure with a lower L:W ratio, the degree of folding is the least which is attributed to the increased stiffness of the structure due to increased width.

To summarize, a more focused analysis on the x-y plane reveals the following: first, a bulging type deformation mode (shown by arrow in (b)) is existent for 45^o orientation for all geometries, which becomes less pronounced for 90^o orientations, except for the case where the sub-grain layers are thicker (middle column) where the opposite is observed. Secondly, a comparison of the images (h) and (i) reveals close resemblance between 45^o and 90^o that gives mechanistic credence to the observations of Benitez et al[40] that kinking is possible due to neighboring effects independent of orientation. Third, overall analysis of all the maps reveal that thicker sub-grain layers show local deformation features (for example, banded stress distribution pattern) that are noticeably different with respect to the other two cases, where the sub-grain layers are of same thicknesses. This indicates that the sub-grain layering (or nano-laminates in the MAX phase jargon) plays an important role in determining the local modes of deformation in a grain structure with geometrical properties similar to that of a MAX phase grain.

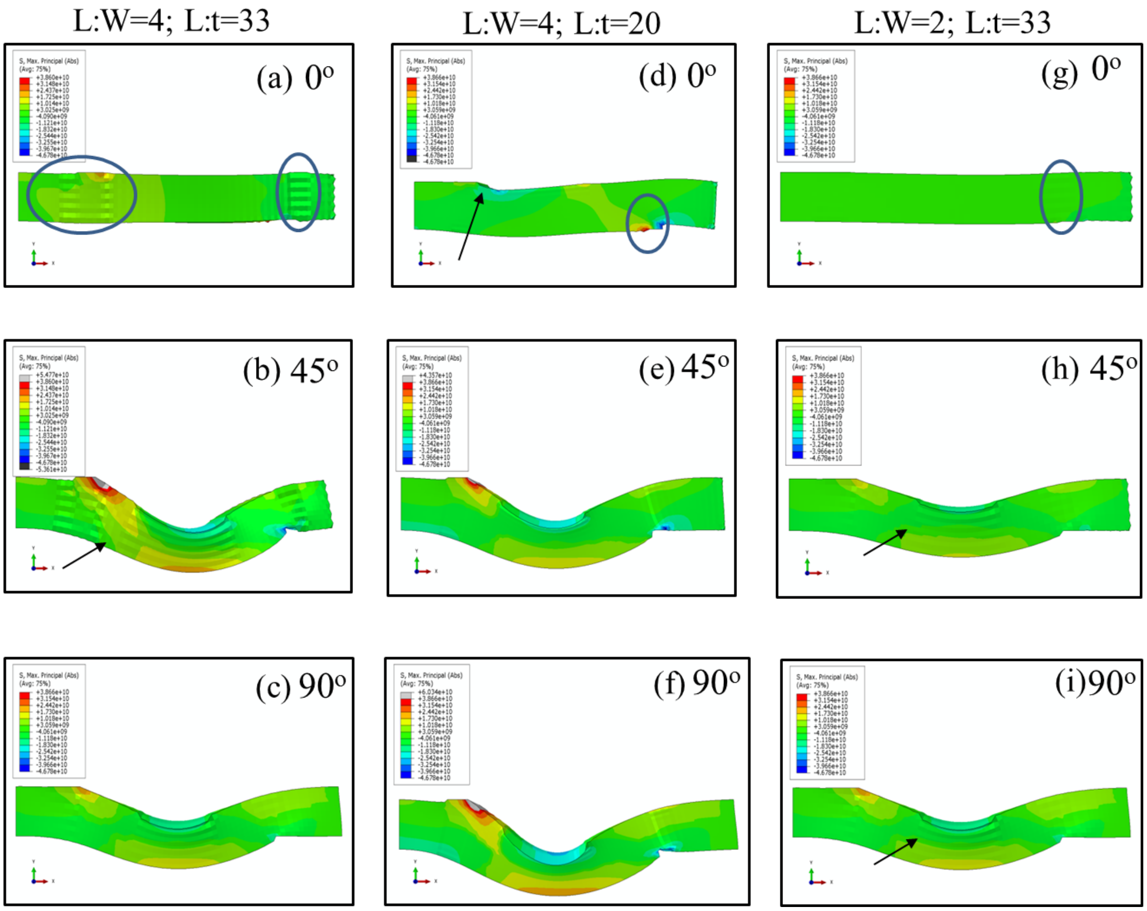

Figure 6.20 Maximum Principal stress contours for idealized grain at different orientations to loading direction, shown for (a)-(c) case I, (d)-(f) case II, and (g)-(i) case III geometrical parameters.

The analysis is now extended to predict the grain scale response of specific cases reported by Guitton et al.[59]. A schematic of their grain structure is shown in Fig.6.21. The arrows show the direction of external compression. It must be noted that for the parametric analysis presented earlier, different geometries and orientations of grain 1 were considered.

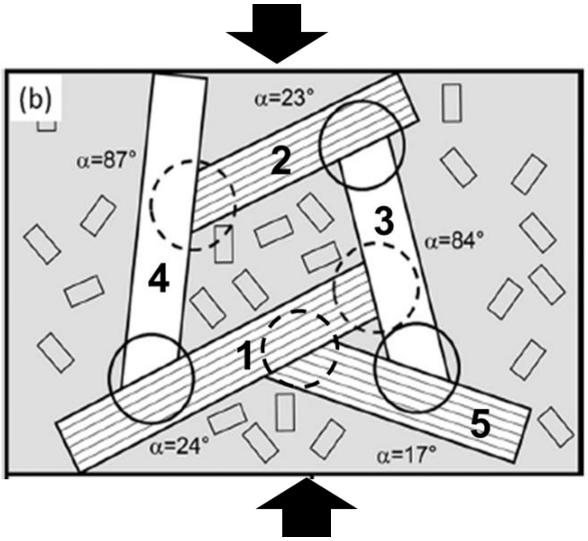

Figure 6.21 Schematic of orientations and connections between grains in a polycrystalline MAX phase (taken from Guitton et al.[59] in accordance with “fair use” policies). The arrows indicate direction of uniaxial external compression.

Figures 6.22 (a)-(e) show the responses of different grains, numbered 1 through 5 in the schematic (Fig. 6.21). It must be noted that the same magnitude of load was applied to all the grains. Therefore, it is inherently assumed that the externally applied load is uniformly distributed between the grains. Grains 1 and 2 (see Figs. 6.22(a) and (b)) have nearly similar orientations. However, the connection regions in grain 2 are less constrained (shown by circles in Fig. 6.21) compared to grain 1. This leads to a greater degree of bending in grain 2. The contour maps show stress concentrations in the vicinity of the grain connection points, as enumerated earlier. Furthermore, due to greater degree of bending in grain 2, the central inner region of the bent configuration has a higher stress (black region in Fig. 6.22(b)) compared to grain 1 (blue central region in Fig. 6.22(a)). Similarly, grains 3 and 4 have nearly same orientation to externally applied loading and show different modes of deformation. That is to say, grain 3 deflects in the x-z plane, as shown in Figs. 6.22(c) whereas grain 4 has a partially bent region in the x-y plane. The difference in stress distributions and deformation modes is attributed to the fact that grain is bounded by large grains on both ends (modeled using a clamp-sliding restraint condition). On the other hand, grain 4 has one end is in the equiaxed region. This leads to a more constrained deformation in grain 4. These results indicate that for similar orientations and same magnitude of externally applied loading, neighboring grains lead to different degrees of deformation. The results show that all families of grains are likely to bend under a uniaxial external load applied to a bulk MAX phase. To this end, the deformability of neighbors and specific end conditions determine the degree or extent of deformation.

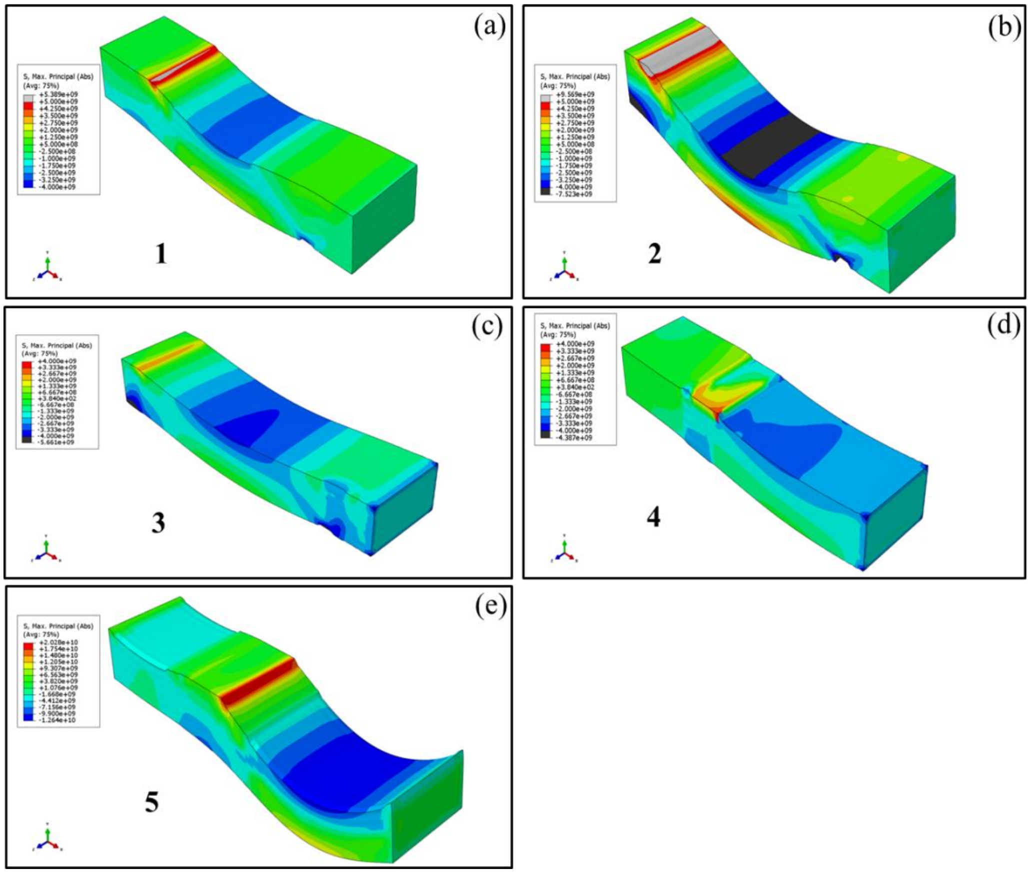

Figure 6.22(a)-(e) Response of a grain to externally applied loading and different neighboring conditions, numbered 1 through 5 in Fig. 6.21.

Figures 6.23(a) shows a representative micrograph taken from Benitez et al.[40]. Figures 6.23(b)-(d) show stress and strain fields in two representative grains (marked as 1 and 2 in Fig. 6.23 (a)) where the neighbors are all equiaxed or connected to one large grain (marked with an arrow in Fig 6.23(a)). An axial compressive load along the x (or 11) direction is applied to the two grain representations, that are fully constrained or partially constrained (see Fig. 6.4). It is observed that the fully constrained grain (Fig. 6.23(a)) deforms or shortens axially without any noticeable bending. On the other hand, the partially constrained grain deforms locally in the region where multi-axial stress is induced by a connecting grain. This could be interpreted as indicative of a micro-stress field that would initiate dislocation nucleation and wall formation and hence kinking and the creation of other substructures. It is anticipated that this would cause gross response of the grain via misorientation and self-consistent deformation (along its aspect ratio). The results presented here show how at the grain continuum level, a multi-axial stress state can be created by the grain neighborhood.

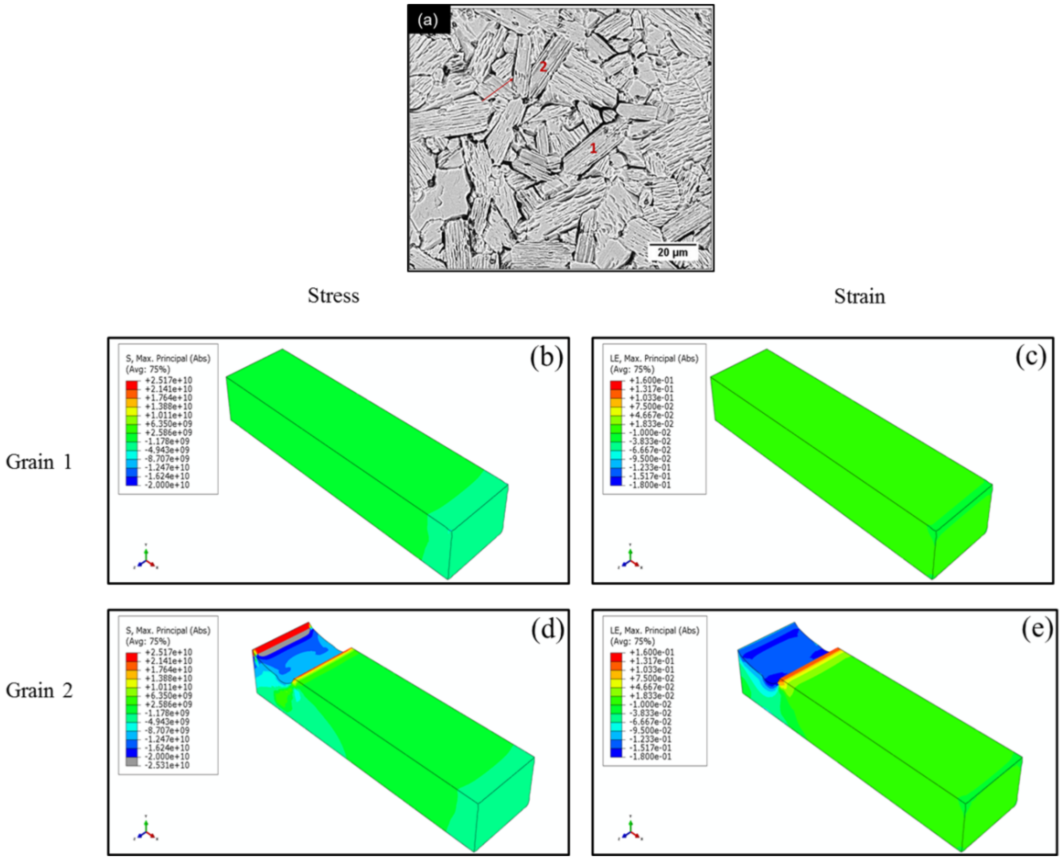

Figure 6.23 Response of a grain in a) complete, and b) partial equiaxed neighborhoods that are representative of micrographs in Benitez et al.[40].

A computational modeling approach is presented herein that accounts for material anisotropy, geometrical parameters, and loading conditions is shown to capture key features associated with the deformation of a representative grain. A multi-axial state of stress exists by virtue of its situation in a polycrystal, that is to say microstructural landscape combined with external loading, anisotropic and geometric effects become important. To this end, it is observed that the number of layers (and hence the thickness of a nano-laminate) in a grain is an important controlling parameter in dictating deformation modes. This is an elusive (if not impossible due to thermodynamic stability reasons) parameter to study experimentally given the current state of the art. Bulk processing methods cannot control this parameter although layer by layer methods such as Molecular Beam Epitaxy (MBE) have been reported in the literature. The geometrical analysis reveals several different deformation modes, the most widespread of which is the grain bending. Guitton et al. [59] in their work hypothesized this to be a possible dominant ramification of plasticity in a MAX phase grain. The current model is limited to the continuum scale and therefore it is impossible to make any comments regarding plasticity or dislocation motion from the results presented here although some mechanistic correlations to Benitez et al.'s[40] was also observed.

6.5. Conclusions

Development of a continuum FE model to represent an idealized MAX phase grain is presented here where the properties of Ti_2AlC are used to contextualize the results to the rest of the dissertation. However, this model can be used for representing any MAX phases by tailoring the properties accordingly. The model takes into account the sub-grain layering ubiquitous in MAX phases and the geometrical parameters are decided based on observation of as processed Ti_2AlC specimens. From a deformation mode standpoint, the thickness of the nano-laminates or sub-grain layering also plays a dominant role mechanistically speaking. A postbuckle analysis on a layered idealized grain shows an imperfection angle beyond which the stress-strain response for an isolated grain is expected to be fully non-linear. A consideration of multi-axial stress states, in accordance to the most recent understandings of the microstructural landscape in a polycrystalline MAX phase, provides credence to the most recent theories in the literature. More specifically, it is observed that longitudinal hard grains show the least stiffness at a global level, when geometric parameters are taken into account. The transversal hard grains are the stiffest with the soft grains having an intermediate stiffness. Irrespective of the orientation, the axial displacement of a grain before it undergoes bending or fold type deformations is dependent on the aspect ratio of sub-grain layers (or indirectly on the number of layers that form a grain). More importantly, it was shown how multiaxial loading leads to bending and folding in multilayered structures provided the grain neighborhood and hence constraint and load-transfer conditions are favorable. By considering heavily constrained grains, credence for localized regions of stress that may cause microstresses and hence a mechanism for self-consistent deformation via kinking was shown. Further work on linking the length scales and developing multiscale methods is crucial for providing a complete deformation map that can settle the debates on the theories of kinking in MAX phases.

Chapter 7: Conclusions and original contributions

In this dissertation, experimental protocols for testing two representative MAX phases (Ti_2AlC and Ti_3SiC_2) under high strain-rates using a SHPB technique has been presented. The macroscale response demonstrated that Ti_2AlC is damage tolerant and retains its pseudo-ductility even under high strain-rates of up to ~5 x 10^3 s^{-1}. Ti_3SiC_2, on the other hand, has a response typical of a conventional ceramic and were tested up to nominal strain-rates of ~1.5 x 10^3 s^{-1}. The average peak stress values lie in the range 608-900 MPa and 600-830 MPa respectively for Ti_2AlC and Ti_3SiC_2. The use of in situ imaging and DIC facilitated visualization of local strain fields, which were observed to be heterogeneous. This motivated further analysis of strain fields over a range of strain-rates (quasi static and dynamic), which revealed an emergent pattern thereby pointing towards mesoscale mechanisms operative in polycrystalline MAX phases. The unique nano-layered structure at the sub-grain level had been the center of attention ever since the bulk processing methods were reported by Barsoum et al[4] in late 1990s. The nano-layered structure forms a kink band when subjected to loading and this leads to higher damage tolerance in MAX phases. The results presented in this dissertation demonstrate that the damage tolerant behavior is retained under high strain-rates for polycrystalline Ti_2AlC. On the other hand, kinking in Ti_3SiC_2 post dynamic loading is not extensively observed although a refined appearance of the grain-structure pointed towards delaminations occurring at a lower length scale. A computational technique was employed to carry out a host of simulations to model the deformation behavior of MAX phases at the microscale. The model clearly showed the influence of neighborhood grains on the deformation and stress of a local grain. The results lend credence to the two competing theories of closed loop hysteresis in the literature. Heavily constrained (large) grains surrounded by a sea of grains will not deform much and develop localized stresses (and hence microstresses and perhaps kink by dislocation based mechanisms). On the other hand, connected networks of large grains will bend and the overall grain scale. This dissertation provides the first mechanistic evidence of grain-scale deformation as a result of the grain neighborhood in MAX phases.

TEM studies in the literature [12]show that highly mobile dislocations lead to the formation of kink bands. Generally speaking, it has been observed that the 211 type MAX phases have a lower elastic stiffness in comparison to the 312 and 413 types. In other words, a lower c/a ratio of the HCP crystal structure leads to lower modulus and therefore are expected to deform more easily in the elastic regime. Recent experimental reports in the literature have pointed to multi-axial stresses in a grain (due to the grain neighborhood) as playing a significant role in inelastic phenomena such as closed loop hysteresis. There still exists a discrepancy in the research community regarding the origins of the inelastic response. Ruling out microcracking as a source (for now), the remaining schools of thought interpret the localized fields as either leading to i) grain bending or ii) self-consistent kinking within the grain due to mobile dislocation activity. Both scenarios are considered in the computational simulations carried out in this dissertation (Chapter 6). As our understanding of inelastic mechanisms in MAX phases evolves, it would be of interest to concurrently probe the influence of the c/a ratio on pseudo-ductile behavior. More specifically, the suggestions for future work can be listed as follows:

1) The dynamic response and deformation mechanisms presented here were for a specific batch of samples processed using a particular method (PS, SPS, etc.). Extending this analysis by understanding the role of grain sizes/geometry, processing route and temperature in the dynamic deformation response mechanisms of MAX phases would shed more light on the deformation mechanisms under high strain-rates. In this regard, a recent report by Parrikar et al.[49] deserves mention, where fine grained Ti_2AlC was studied under high strain-rates over a range of temperatures. In this regard, understanding the role of secondary phases like TiAlx, which are common in powder processing routes, on the mechanical behavior could be important. In this way, acceptable limits could be proposed as a set of guidelines for processing. Therefore, computational models could prove quite useful whereby a systematic analysis of various composite representations consisting of the different phases could be carried out.

2) An extension of the previous point is related to understanding the role of brittle modes of deformation in the dynamic deformation process. The in situ method (DIC) used in this dissertation can only provide surface level measurements. However, recent work in the literature on Ti_2AlC has shown degradation of modulus due to microcracking under static loads. Therefore, it is likely that underlying microcracks develop under dynamic deformation conditions as well. To this end, state of the art methods like in situ x-ray techniques combined with DIC can provide information about sub-surface level localized damage mechanisms, as has been reported most recently for SiC[102].

3) Preliminary results have shown that Ti_2AlC retains its integrity post thermal quench and even retains some of the pseudoductility under high strain-rates of ~3500 s^{-1}. A clearer picture of thermal shock mechanisms and a complete understanding of the post quench dynamic response is still an open question.

4) The mechanisms and theories underlying kinking and how that connects from the fundamental length scales to the bulk macroscale has been the topic of several works in the literature and new theories are evolving, mechanistic aspects for some of which has been discussed in this dissertation. A complete understanding in this regard through multiscale analysis is a promising direction.

5) Lastly, from a structural application perspective, for example, in high temperature aerospace applications, MAX phases are interesting for their damping properties. Therefore, their integration with SMAs to form composites has led to promising results, as reported in recently published literature. Although this is not a direction extension of the work presented in this dissertation, this point connects back to idealized FGHC structure briefly discussed in the first chapter.

Appendices

Appendix A: SHPB Data Processing and MATLAB Code

An overview of the method has been presented in the dissertation with relevant equations for equilibrium time achievement in chapters 2, 3, and 4 along with the key equations for a 2 wave analysis. In this appendix, further information regarding the checking points for stress equilibrium condition (a very important consideration) and code for analyzing the data and plotting the results is provided. Note that the code gives a step by step procedure of how to deduce the data – the output of interest might be different based on the user's preferences (for example, stress-strain, strain-rate vs strain, etc.) and appropriate "plot" functions needed to be inserted in the code accordingly. It is generally recommended that the output is plotted after performing each step to carefully delineate the portion of the data that is representative of true material response. To this end, if a camera is used in conjunction with the set-up, the frames need to be matched to the times on the signal after time shifting and start time determination procedures.

Stepwise development of MATLAB code for data processing

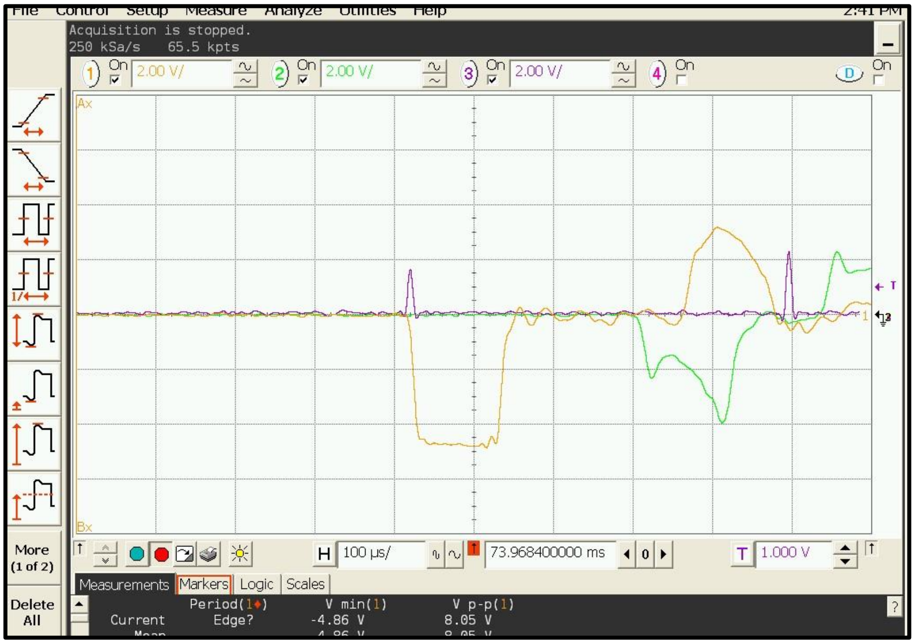

Figure A.1 A typical SHPB signal output on an oscilloscope

STEP 1: Import csv filed generated from Oscilloscope into the script for analysis. Usually recommended that the memory is cleared to avoid overlap due to similar variable names. A typical SHPB experimental data looks like the following image shown above.

```
clc;clear all;

Datainp=importdata('MAXSample#_Test#.csv');%csvread function can also
be used

% Define variables:

Time=max(:,1);Incident=max(:,2);Transmitted=max(:,3);
```

STEP 2: Convert outputted voltage to strains using gain and excitation voltage and plot. Comparison with image file outputted from scope is generally a good practice.

```
Strain_inci=(4/(Gain*V_excitation)).*Incident;

Strain_trans=(4/(Gain*V_excitation)).*Transmitted;

Time_plot=(t(:)-t(1)).*10^6;%Zero out start time and convert to
microsseconds
```

STEP 3: Input bar and specimen material, geometric parameters for calculation

```
L_inci=#; %Incident bar length

L_trans=#; %Transmission bar length

L_spec=#; %Length of specimen

Den_bar=#; % Density of bar material

Den_spec=#; %Density of specimen

E_bar=#; %Modulus of bar material

E_spec=#; %Modulus of specimen material

Cb=sqrt(E_bar/Den_bar); % Wave Speed in bar material

Cs=sqrt(E_spec/Den_spec); % Wave speed in specimen material

A_bar=#; %Cross sectional area of bars

A_spec=#; %Cross sectional area of specimen
```

STEP 4: Perform time shifting of the waves to line up the waves at the specimen-incident bar interface.

```
%Multiplied by 10^6 to convert to μs

delt=(((L_inci/2) + (L_trans/2))/Cb + L_spec/Cs).*10^6;

delt2=(L0/Cb).*10^6;
```

STEP 5: Determine the start and end times of the pulses, and save them into variables as follows. These will be used for data processing below.

```
Strain_inci1=Strain_inci(start_time1:End_time1);

Strain_ref1=Strain_inci(Start_time2:End_time2);

Strain_trans1=-Strain_trans(Start_time2:End_time2);
```

STEP 6: Calculate the incident strain by adding the reflected and transmitted pulses. Make sure the signs are correct, depending on whether tensile or compressive load is applied

```
Strain_calc=Strain_ref1 + Strain_trans1;
```

Compare strain_calc with Strain_inci – for a good set of signals lined up correctly, the wave pulses should have an appearance similar to the image shown below:

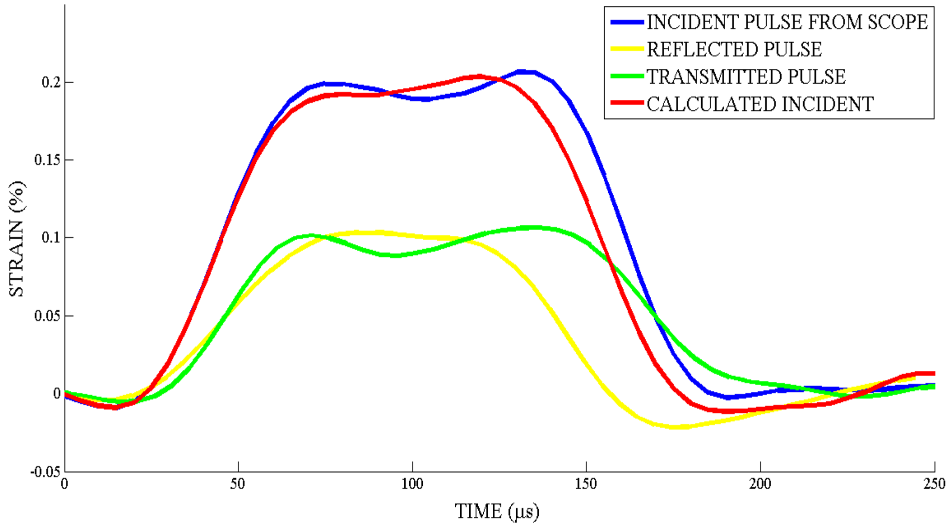

Figure A.2 A typical example of lined up pulses. Note that the strain in the y-axis is the strain obtained from the bars as raw data. This needs to be analyzed using the 2 wave analysis equations (see chapter 2) to deduce the material data.

STEP 7: An additional check for stress equilibrium should also be performed to make sure that dynamic equilibrium exists for the time for which stress-strain behavior is calculated, as given by the code snippet below:

```
Stress_front=(A_bar/A_spec).*E_bar(Strain_inci1 + Strain_ref1);
```

```
Stress_back=(A_bar/A_spec).*E_bar(Strain_trans1);
```

STEP 8: Calculate the Stress, Strain and Strain-Rate in the specimen and plot whichever quantities are of interest

```
%Multiplied by 10^-6 to convert units to MPa

Stress=((A_bar)/(A_spec)).*E_bar.*(10^-6).*Strain_trans(Start time: End time);

%Multiplied by 100 to convert strain to (%)

Strain=((2*Cb/LS).*cumtrapz(t(Start:End),Strain_ref(Start:End))).*100;

Strain rate =(2*Cb/LS).*Strain_ref(Start:End);
```

STEP 9: Plot whichever quantities are of interest. Typically a stress-strain plot and strain-rate versus strain plots are made to present the material response and attainment of constant strain-rate in the specimen.

Appendix B: DIC Strain Smearing

The region on the FOV over which strains are smeared in the DIC calculations, under static and dynamic loading conditions, is presented in this appendix. The speckle sizes and analysis software (ARAMIS) parameters – facet size, step size, and computation size determine the resolution of strain measurements or region over which strains are smeared. In addition, another parameter of interest is the type of interpolation. The default option is linear and has been used for all measurements since a comparison with spline interpolation showed negligible error, as mentioned earlier (section 5.1). Figure 5A.1(a) shows the facet field overlaid on a Ti_3SiC_2 specimen tested under high strain-rates (10^2-10^3 s^{-1}). The speckle sizes lie in the range 120-270 μm (0.12-0.27 mm) and the facet sizes are chosen such that there is a recognizable greyscale distribution in each facet (shown by green boxes). It must be noted that a small region on two edges are left out to avoid any edge effects in the measurements. DIC algorithm tracks the movement of this greyscale distribution relative to its center point at different frames and determines the displacement vector, based on which strains are calculated and the strain is smeared over this region. For the results presented in this dissertation, the strain smeared region is on the order of ~390 μm (0.3 mm). A computation size can be defined as the number of center points used to calculate strain at a considered facet point. Said otherwise, ARAMIS reports a strain value for a considered center point once correlation is obtained from the neighboring center points and the number of points is set by the computation size. Figure 5A.1 (b) shows the computation area, which contains 3 x 3 facets and represents the region over which the strain tensor is calculated. The center to center distance between the facets is given by the step size that is a user input. A smaller step size leads to extraction of maximum information in terms of local field evolution. A thumb rule is to input a step size that is lesser than the facet size to obtain highest degree of local field information.

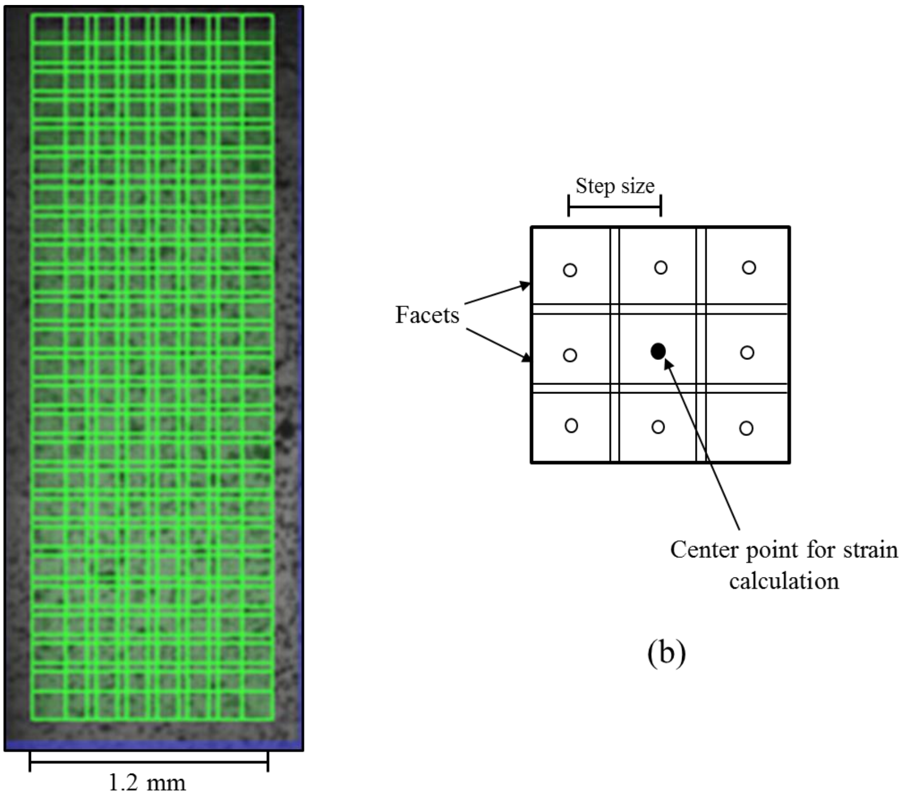

(a) (b)

Figure B.1 DIC software inputs showing a) facet field overlaid on the sample surface, and b) schematic of the grid highlighting facet, step and computation sizes.

Appendix C: ABAQUS model procedures

A detailed description of the methodical steps followed, unit conversions and mesh convergence for the computational model developed in ABAQUS is presented here. The flow diagram (Figure C.1) below shows the step-by-step procedure for the Riks analysis that is presented an extension to the 2D Dodwell model in chapter 6.

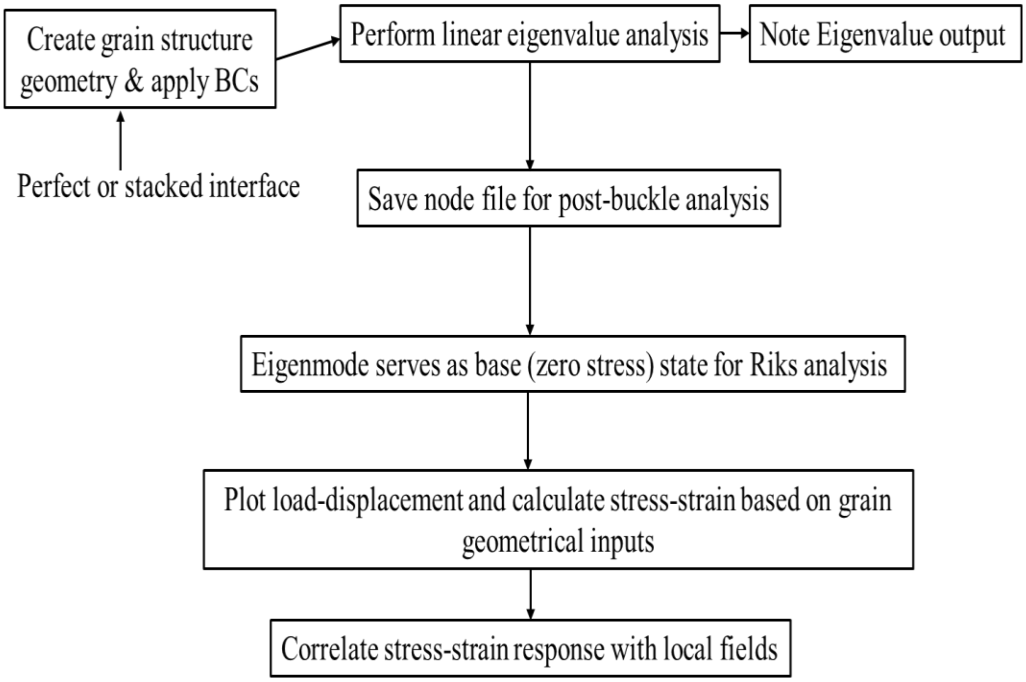

Figure C.1 Flow Diagram depicting the steps followed for uniaxial loading analysis

To check the validity of the output, the result output from eigenvalue and Riks analysis step for a perfect beam structure is compared to the static compression step for much lower displacements, and the results indicate good agreement, as shown below in Fig. C.2

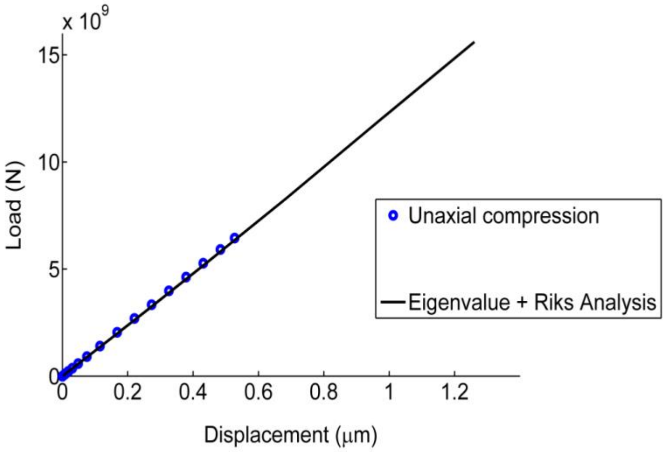

Figure C.2 Load versus displacement from uniaxial compression and Eigenvalue / Riks Analysis in the small displacement regime.

Since ABAQUS has no inherent units, consistent units are typically used. That is to say, Force is in Newtons (N), length in millimeters (mm), and stress in MegaPascal (MPa). For the results presented in this dissertation, the length or dimensional quantities are represented in μm. Therefore, a conversion of units is necessary, as follows:

$$1\,\mu m^2 \times 10^{-9} = 1\,mm^2$$

Therefore, the stress outputs shown in chapter 6 should be multiplied by a factor of 10-9 to give the corresponding value in MPa. An example is shown below in Fig. C.3 to provide a ballpark estimate using an image taken from one of the contours presented in chapter 6. It can be observed that the stresses lie in range of -39 MPa to 60 MPa.

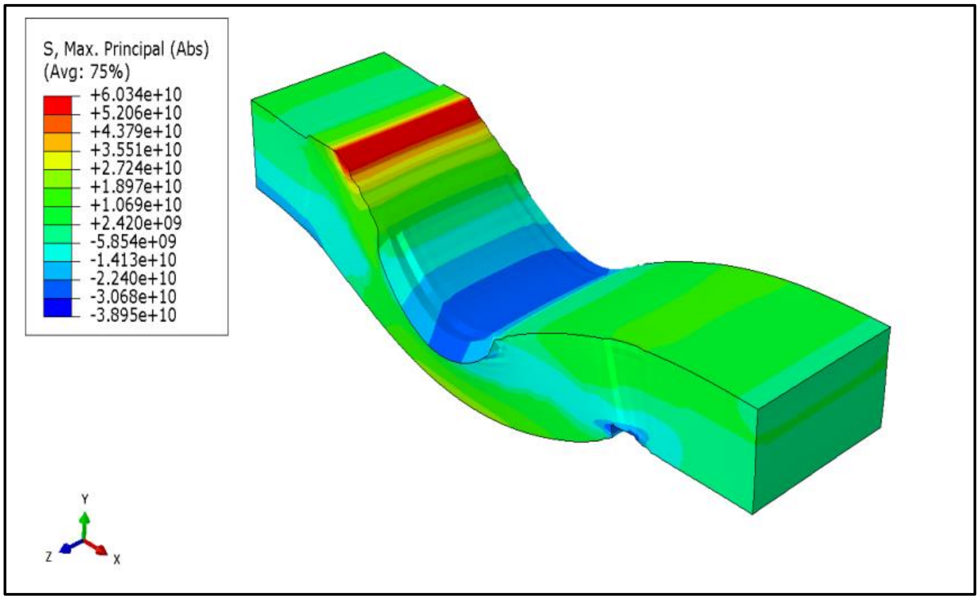

Figure C.3 Maximum principal stress contours to represent the range of values of stress

Mesh convergence studies using the linear eigenvalue buckling functionality was conducted to determine the mesh density that would optimize accuracy and run time (computational cost) for a given geometry. An estimate for the L:W =4 and L:t=33 is provided below (Case I from Table 6.2). It must be noted that C3D8R (8 noded 3D brick elements) were used for all the simulation runs. For this geometry, the mesh density with 17400 elements were chosen since increasing the number of elements by 5 times only led to a change on the order of 10^{-3} in the output, with significantly higher computational times (> 1 CPU hour).

Table C.1 Element type and mesh information for FE analysis

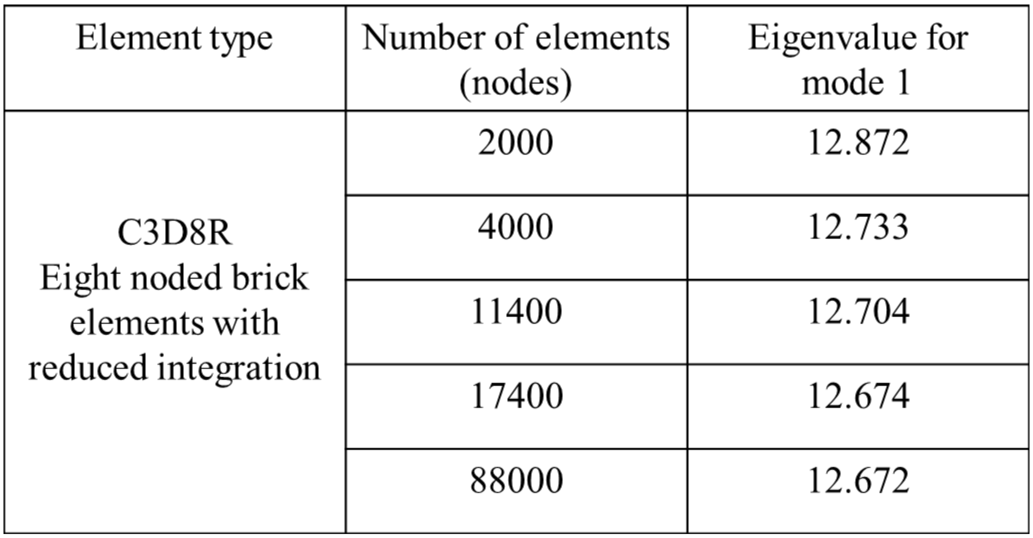

Element type	Number of elements (nodes)	Eigenvalue for mode 1
C3D8R Eight noded brick elements with reduced integration	2000	12.872
	4000	12.733
	11400	12.704
	17400	12.674
	88000	12.672

Bibliography

[1] M.W. Barsoum, Progress in Solid State Chemistry, 28 (2000) 201-281.
[2] M.W. Barsoum, M. Radovic, Annual review of materials research, 41 (2011) 195-227.
[3] M. Radovic, M.W. Barsoum, American Ceramics Society Bulletin, 92 (2013) 20-27.
[4] M.W. Barsoum, T. El-Raghy, Journal of the American Ceramic Society, 79 (1996) 1953-1956.
[5] W. Jeitschko, H. Nowotny, Monatshefte für Chemie und verwandte Teile anderer Wissenschaften, 98 (1967) 329-337.
[6] H. Nowotny, P. Rogl, J.C. Schuster, Journal of Solid State Chemistry, 44 (1982) 126-133.
[7] T. El-Raghy, M.W. Barsoum, Journal of the American Ceramic Society, 82 (1999) 2849-2854.
[8] D.W. Brown, S.R. Agnew, M.A.M. Bourke, T.M. Holden, S.C. Vogel, C.N. Tomé, Materials Science and Engineering: A, 399 (2005) 1-12.
[9] S. Zaefferer, Materials Science and Engineering: A, 344 (2003) 20-30.
[10] M.W. Barsoum, MAX phases: properties of machinable ternary carbides and nitrides, John Wiley & Sons, 2013.
[11] C.J. Shih, M.A. Meyers, V.F. Nesterenko, S.J. Chen, Acta Materialia, 48 (2000) 2399-2420.
[12] M.W. Barsoum, L. Farber, T. El-Raghy, Metallurgical and Materials Transactions A, 30 (1999) 1727-1738.
[13] B. Budiansky, N.A. Fleck, Journal of the Mechanics and Physics of Solids, 41 (1993) 183-211.
[14] P. Davidson, A.M. Waas, Mathematics and Mechanics of Solids, (2014) 1081286514535422.
[15] Y.C. Zhou, X.H. Wang, Material Research Innovations, 5 (2001) 87-93.
[16] M.W. Barsoum, T. El-Raghy, M. Ali, Metallurgical and Materials Transactions A, 31 (2000) 1857-1865.
[17] T. El-Raghy, M.W. Barsoum, A. Zavaliangos, S.R. Kalidindi, Journal of the American Ceramic Society, 82 (1999) 2855-2860.
[18] M.W. Barsoum, T. Zhen, S.R. Kalidindi, M. Radovic, A. Murugaiah, Nature Materials, 2 (2003) 107-111.
[19] N.V. Tzenov, M.W. Barsoum, Journal of the American Ceramic Society, 83 (2000) 825-832.
[20] X.H. Wang, Y.C. Zhou, Acta Materialia, 50 (2002) 3143-3151.
[21] X.H. Wang, Y.C. Zhou, Corrosion Science, 45 (2003) 891-907.
[22] M. Radovic, M.W. Barsoum, T. El-Raghy, J. Seidensticker, S. Wiederhorn, Acta materialia, 48 (2000) 453-459.
[23] G.M. Song, Y.T. Pei, W.G. Sloof, S.B. Li, J.T.M. De Hosson, S. Van der Zwaag, Scripta Materialia, 58 (2008) 13-16.
[24] M.W. Barsoum, N. Tzenov, A. Procopio, T. El-Raghy, M. Ali, Journal of The Electrochemical Society, 148 (2001) C551-C562.
[25] M.W. Barsoum, L.H. Ho-Duc, M. Radovic, T. El-Raghy, Journal of the electrochemical society, 150 (2003) B166-B175.
[26] M. Sundberg, G. Malmqvist, A. Magnusson, T. El-Raghy, Ceramics International, 30 (2004) 1899-1904.

[27] R. Bhattacharya, R. Benitez, M. Radovic, N.C. Goulbourne, Materials Science and Engineering: A, 598 (2014) 319-326.
[28] A. Murugaiah, A. Souchet, T. El-Raghy, M. Radovic, M. Sundberg, M.W. Barsoum, Journal of the American Ceramic Society, 87 (2004) 550-556.
[29] J.-F. Li, T. Matsuki, R. Watanabe, Journal of materials science, 38 (2003) 2661-2666.
[30] N.F. Gao, J.T. Li, D. Zhang, Y. Miyamoto, Journal of the European Ceramic Society, 22 (2002) 2365-2370.
[31] C. Hu, Y. Sakka, S. Grasso, T. Suzuki, H. Tanaka, Journal of the American Ceramic Society, 94 (2011) 742-748.
[32] J. Henon, M.A. Piechowiak, O. Durand-Panteix, G. Etchegoyen, O. Masson, C. Dublanche-Tixier, P. Marchet, B. Lucas, F. Rossignol, Journal of the European Ceramic Society, 35 (2015) 1179-1189.
[33] T. Lapauw, K. Vanmeensel, K. Lambrinou, J. Vleugels, Scripta Materialia, 111 (2016) 98-101.
[34] M.W. Barsoum, D. Brodkin, T. El-Raghy, Scripta Materialia, 36 (1997) 535–541.
[35] M.W. Barsoum, T. El-Raghy, M. Ali, Metallurgical and Materials Transactions A, 31 (2000) 1857–1865.
[36] F.L. Meng, Y.C. Zhou, J.Y. Wang, Scripta materialia, 53 (2005) 1369–1372.
[37] M. Radovic, M.W. Barsoum, T. El-Raghy, S.M. Wiederhorn, W.E. Luecke, Acta materialia, 50 (2002) 1297–1306.
[38] C. Hu, L. He, M. Liu, X. Wang, J. Wang, M. Li, Y. Bao, Y. Zhou, Journal of the American Ceramic Society, 91 (2008) 4029–4035.
[39] N.G. Jones, C. Humphrey, L.D. Connor, O. Wilhelmsson, L. Hultman, H.J. Stone, F. Giuliani, W.J. Clegg, Acta Materialia, 69 (2014) 149–161.
[40] R. Benitez, W.H. Kan, H. Gao, M. O'Neal, G. Proust, M. Radovic, Acta Materialia, 105 (2016) 294-305.
[41] T. El-Raghy, M.W. Barsoum, A. Zavaliangos, S.R. Kalidindi, Journal of the American Ceramic Society, 82 (1999) 2855–2860.
[42] W. Tian, Z. Sun, Y. Du, H. Hashimoto, Materials Letters, 63 (2009) 670–672.
[43] D.T. Wan, F.L. Meng, Y.C. Zhou, Y.W. Bao, J.X. Chen, Journal of the European Ceramic Society, 28 (2008) 663–669.
[44] M.F. Ashby, J.D. Embury, Scripta metallurgica, 19 (1985) 557–562.
[45] T. Zhen, M.W. Barsoum, S.R. Kalidindi, Acta materialia, 53 (2005) 4163–4171.
[46] Y.W. Bao, X.H. Wang, H.B. Zhang, Y.C. Zhou, Journal of the European Ceramic Society, 25 (2005) 3367–3374.
[47] H.B. Zhang, Y.C. Zhou, Y.W. Bao, M.S. Li, Journal of materials research, 21 (2006) 2401–2407.
[48] W.-T. Lo, C.-A. Jeng, J.-L. Huang, H.-H. Lu, D.-F. Lii, Journal of Alloys and Compounds, 455 (2008) 413-419.
[49] P.N. Parrikar, R. Benitez, H. Gao, M. Radovic, A. Shukla, Materials Science and Engineering: A, 658 (2016) 176-184.
[50] A. Johnson, Styles of folding: mechanics and mechanisms of folding of natural elastic materials, Elsevier, 2012.
[51] N.J. Price, J.W. Cosgrove, Analysis of geological structures, Cambridge University Press, 1990.
[52] E. Orowan, Nature, 149 (1942) 643–644.

[53] J.B. Hess, C.S. Barrett, TRANSACTIONS OF THE AMERICAN INSTITUTE OF MINING AND METALLURGICAL ENGINEERS, 185 (1949) 599–606.
[54] F.C. Frank, A.N. Stroh, Proceedings of the Physical Society. Section B, 65 (1952) 811.
[55] M.W. Barsoum, T. Zhen, A. Zhou, S. Basu, S.R. Kalidindi, Physical Review B, 71 (2005) 134101.
[56] A.G. Zhou, S. Basu, G. Friedman, P. Finkel, O. Yeheskel, M.W. Barsoum, others, Physical Review B, 82 (2010) 094105.
[57] A. Guitton, A. Joulain, L. Thilly, C. Tromas, Philosophical Magazine, 92 (2012) 4536–4546.
[58] N.J. Lane, S. Simak, A. Mikhaylushkin, I. Abrikosov, L. Hultman, M.W. Barsoum, Physical Review B. Condensed Matter and Materials Physics, 84 (2011) 184101.
[59] A. Guitton, S. Van Petegem, C. Tromas, A. Joulain, H. Van Swygenhoven, L. Thilly, Applied Physics Letters, 104 (2014) 241910.
[60] C.J. Gilbert, D.R. Bloyer, M.W. Barsoum, T. El-Raghy, A.P. Tomsia, R.O. Ritchie, Scripta Materialia, 42 (2000) 761–767.
[61] J.B. Hess, C.S. Barrett, TRANSACTIONS OF THE AMERICAN INSTITUTE OF MINING AND METALLURGICAL ENGINEERS, 185 (1949) 599-606.
[62] F.C. Frank, A.N. Stroh, Proceedings of the Physical Society. Section B, 65 (1952) 811.
[63] Z.F. Zhang, Z.M. Sun, Materials Science and Engineering: A, 408 (2005) 64–71.
[64] F. Barcelo, S. Doriot, T. Cozzika, M. Le Flem, J.L. Béchade, M. Radovic, M.W. Barsoum, Journal of Alloys and Compounds, 488 (2009) 181–189.
[65] A. Guitton, S. Van Petegem, C. Tromas, A. Joulain, H. Van Swygenhoven, L. Thilly, Applied Physics Letters, 104 (2014) 241910.
[66] M. Shamma, N.C. El'ad, B. Anasori, B. Clausen, D.W. Brown, S.C. Vogel, V. Presser, S. Amini, O. Yeheskel, M.W. Barsoum, Acta Materialia, 98 (2015) 51-63.
[67] R. Bhattacharya, R. Benitez, M. Radovic, N.C. Goulbourne, Materials Science and Engineering: A, 598 (2014) 319–326.
[68] H. Kolsky, Proceedings of the Physical Society. Section B, 62 (1949) 676.
[69] K.T. Ramesh, S. Narasimhan, International journal of solids and structures, 33 (1996) 3723-3738.
[70] E.D.H. Davies, S.C. Hunter, Journal of the Mechanics and Physics of Solids, 11 (1963) 155-179.
[71] G.T. Gray, H. Kuhn, D. Medlin, ASM International, Materials Park, (2000) 462.
[72] S. Sarva, S. Nemat-Nasser, Materials Science and Engineering: A, 317 (2001) 140-144.
[73] B. Song, W. Chen, Y. Ge, T. Weerasooriya, Journal of Biomechanics, 40 (2007) 2999-3005.
[74] U.S. Lindholm, Journal of the Mechanics and Physics of Solids, 12 (1964) 317-335.
[75] Z.G. Wang, L.W. Meyer, Experimental mechanics, 50 (2010) 1061-1074.
[76] G. Ravichandran, G. Subhash, Journal of the American Ceramic Society, 77 (1994) 263-267.
[77] J. Lankford, W.W. Predebon, J.M. Staehler, G. Subhash, B.J. Pletka, C.E. Anderson, Mechanics of Materials, 29 (1998) 205-218.

[78] W.W. Chen, B. Song, Split Hopkinson (Kolsky) bar: design, testing and applications, Springer Science & Business Media, 2010.

[79] M.A. Sutton, J.J. Orteu, H. Schreier, Image correlation for shape, motion and deformation measurements: basic concepts, theory and applications, Springer Science & Business Media, 2009.

[80] S. Yaofeng, J.H.L. Pang, Optics and lasers in engineering, 45 (2007) 967-974.

[81] F. Hild, S. Roux, Strain, 42 (2006) 69-80.

[82] T.A. Berfield, J.K. Patel, R.G. Shimmin, P.V. Braun, J. Lambros, N.R. Sottos, Experimental Mechanics, 47 (2007) 51-62.

[83] W.A. Scrivens, Y. Luo, M.A. Sutton, S.A. Collette, M.L. Myrick, P. Miney, P.E. Colavita, A.P. Reynolds, X. Li, Experimental Mechanics, 47 (2007) 63-77.

[84] C. Efstathiou, H. Sehitoglu, Scripta Materialia, 59 (2008) 1263-1266.

[85] C. Efstathiou, H. Sehitoglu, J. Lambros, International Journal of Plasticity, 26 (2010) 93-106.

[86] A. Godara, D. Raabe, Composites Science and technology, 67 (2007) 2417-2427.

[87] M.A. Sutton, Applied Mechanics Reviews, 65 (2013) 050802.

[88] M. Pankow, B. Justusson, A.M. Waas, Applied optics, 49 (2010) 3418-3427.

[89] J.D. Helm, M.A. Sutton, S.R. McNeill, Optical Engineering, 42 (2003) 1293-1305.

[90] T. Zhu, M.A. Sutton, N. Li, J.J. Orteu, N. Cornille, X. Li, A.P. Reynolds, Experimental Mechanics, 51 (2011) 97-109.

[91] M. Radovic, M.W. Barsoum, A. Ganguly, T. Zhen, P. Finkel, S.R. Kalidindi, E. Lara-Curzio, Acta materialia, 54 (2006) 2757-2767.

[92] R. Bhattacharya, N.C. Goulbourne, Deformation mechanisms in Mn+ 1AXn phase ternary ceramics at High Strain Rates, Dynamic Behavior of Materials, Volume 1, Springer, 2013, pp. 583-597.

[93] M. Pankow, C. Attard, A.M. Waas, The Journal of Strain Analysis for Engineering Design, 44 (2009) 689-698.

[94] M. Radovic, M.W. Barsoum, T. El-Raghy, S.M. Wiederhorn, W.E. Luecke, Acta materialia, 50 (2002) 1297-1306.

[95] N.J. Lane, M. Naguib, J. Lu, L. Hultman, M.W. Barsoum, Journal of the European Ceramic Society, 32 (2012) 3485-3491.

[96] W.K. Pang, I.-M. Low, B.H. O'Connor, A.J. Studer, V.K. Peterson, Z.-M. Sun, J.P. Palmquist, IOP Publishing, 2010, pp. 012025.

[97] B. Poon, L. Ponson, J. Zhao, G. Ravichandran, Journal of the Mechanics and Physics of Solids, 59 (2011) 2238-2257.

[98] T. Zhen, M.W. Barsoum, S.R. Kalidindi, Acta materialia, 53 (2005) 4163-4171.

[99] J.M. Staehler, W.W. Predebon, B.J. Pletka, J. Lankford, Journal of the American Ceramic Society, 76 (1993) 536-538.

[100] W. Chen, G. Subhash, G. Ravichandran, Dymat Journal, 1 (1994) 193-210.

[101] W. Chen, G. Ravichandran, Journal of the American Ceramic Society, 79 (1996) 579-584.

[102] J.Y. Huang, L. Lu, D. Fan, T. Sun, K. Fezzaa, S.L. Xu, M.H. Zhu, S.N. Luo, Scripta Materialia, 111 (2016) 114-118.

[103] M. Fazzini, S. Mistou, O. Dalverny, L. Robert, Optics and Lasers in Engineering, 48 (2010) 335-339.

[104] H.W. Schreier, J.R. Braasch, M.A. Sutton, Optical engineering, 39 (2000) 2915-2921.

[105] V. Valle, S. Hedan, P. Cosenza, A.L. Fauchille, M. Berdjane, Experimental Mechanics, 55 (2015) 379-391.

[106] H.W. Schreier, M.A. Sutton, Experimental Mechanics, 42 (2002) 303-310.

[107]

[108] A. Guitton, A. Joulain, L. Thilly, C. Tromas, Philosophical Magazine, 92 (2012) 4536-4546.

[109] G.-P. Bei, A. Guitton, A. Joulain, V. Brunet, S. Dubois, L. Thilly, C. Tromas, Philosophical Magazine, 93 (2013) 1784-1801.

[110] N.G. Jones, C. Humphrey, L.D. Connor, O. Wilhelmsson, L. Hultman, H.J. Stone, F. Giuliani, W.J. Clegg, Acta Materialia, 69 (2014) 149-161.

[111] M.A. Wadee, G.W. Hunt, M.A. Peletier, Journal of the Mechanics and Physics of Solids, 52 (2004) 1071-1091.

[112] M.A. Wadee, R. Edmunds, Journal of the Mechanics and Physics of Solids, 53 (2005) 2017-2035.

[113] J.A. Boon, C.J. Budd, G.W. Hunt, The Royal Society, 2007, pp. 1447-1466.

[114] T.J. Dodwell, G.W. Hunt, M.A. Peletier, C.J. Budd, Philosophical Transactions of the Royal Society of London A: Mathematical, Physical and Engineering Sciences, 370 (2012) 1740-1758.

[115] A.U. Manual, Dassault Systémes Simulia Corp., Providence, RI.